2022

Characterizing the Internal Porous Structure of Equine Proximal Sesamoid Bones Subjected to Race Training Using Fast Fourier Transforms

Joseph Erik Davis
University of Kentucky, j.erik.davis@outlook.com
Author ORCID Identifier:
https://orcid.org/0000-0001-9292-4603
Digital Object Identifier: https://doi.org/10.13023/etd.2022.69

STUDENT AGREEMENT:

I represent that my thesis or dissertation and abstract are my original work. Proper attribution has been given to all outside sources. I understand that I am solely responsible for obtaining any needed copyright permissions. I have obtained needed written permission statement(s) from the owner(s) of each third-party copyrighted matter to be included in my work, allowing electronic distribution (if such use is not permitted by the fair use doctrine) which will be submitted to UKnowledge as Additional File.

I hereby grant to The University of Kentucky and its agents the irrevocable, non-exclusive, and royalty-free license to archive and make accessible my work in whole or in part in all forms of media, now or hereafter known. I agree that the document mentioned above may be made available immediately for worldwide access unless an embargo applies.

I retain all other ownership rights to the copyright of my work. I also retain the right to use in future works (such as articles or books) all or part of my work. I understand that I am free to register the copyright to my work.

REVIEW, APPROVAL AND ACCEPTANCE

The document mentioned above has been reviewed and accepted by the student's advisor, on behalf of the advisory committee, and by the Director of Graduate Studies (DGS), on behalf of the program; we verify that this is the final, approved version of the student's thesis including all changes required by the advisory committee. The undersigned agree to abide by the statements above.

Joseph Erik Davis, Student

Dr. Guigen Zhang, Major Professor

Dr. Sridhar Sunderam, Director of Graduate Studies

CHARACTIZING THE INTERNAL POROUS STRUCTURE OF EQUINE PROXIMAL SESAMOID BONES SUBJECTED TO RACE TRAINING USING FAST FOURIER TRANSFORMS

THESIS

A thesis submitted in partial fulfillment of the
requirements for the degree of Master of Science in the
College of Engineering
at the University of Kentucky

By

Joseph Erik Davis

Lexington, Kentucky

Director: Dr. Guigen Zhang, Professor of Biomedical Engineering

Lexington, Kentucky

2022

https://orcid.org/0000-0001-9292-4603

ABSTRACT OF THESIS

CHARACTIZING THE INTERNAL POROUS STRUCTURE OF EQUINE PROXIMAL SESAMOID BONES SUBJECTED TO RACE TRAINING USING FAST FOURIER TRANSFORMS

The equine racing industry is one of the main proponents in Kentucky's economic infrastructure. In this industry there has come a need to investigate the nature of the proximal sesamoid bone (PSB). Breakdowns involving the PSBs are the leading cause in racehorse deaths in the industry, with still little known about what causes this bone to fracture. This study seeks to shed insight by investigating the internal structure of the PSB. Using microCT scanning, the internal porous structure was captured. From there, noticeable differences in the pores were noticed and quantified using fast Fourier transform (FFT) analysis.

The dominant peak frequencies in each FFT spectrum hold information about the pore size and pore repeating pattern for each of selected window for the FFT analysis. The dominant peak distribution shape was characterized by a confidence ellipse for each FFT spectrum. The size of the ellipse in the frequency domain holds information that can be converted to the spatial domain to characterize the size and spacing of the porous network within the PSB.

The findings of this study show interesting implications for the idea that the PSB is regionally changing the internal nature of the bone which lead to changes in structural integrity. It was observed that there were regional differences in the fracture types that could correspond with their specific fracture. A linear mixed model statistical analysis was used on the data, and it was shown that some biological factors are only shown to be significant in certain areas and not in others, while some factors are also only shown to affect the angle of the bone and not the size of the bone. Looking at the specific differences and biological factor effects, we can pinpoint which regions are experiencing changing due to the specific factors.

KEYWORDS: Image Processing, Proximal Sesamoid Bones, Fast Fourier Transforms, Microarchitecture

Joseph Erik Davis

04/26/2022

CHARACTIZING THE INTERNAL POROUS STRUCTURE OF EQUINE PROXIMAL SESAMOID BONES SUBJECTED TO RACE TRAINING USING FAST FOURIER TRANSFORMS

By
Joseph Erik Davis

Dr. Guigen Zhang
Director of Thesis

Dr. Sridhar Sunderam
Director of Graduate Studies

04/26/2022
Date

DEDICATION

To my amazing family and friends. The amount of support I have received throughout my graduate journey has been immeasurable. There was never a time where I felt like I was alone on this journey, and, for that, I am forever thankful.

ACKNOWLEDGMENTS

This thesis could not have been completed alone and I have a long list of people who I would like to acknowledge for their input and guidance

First, I would like to thank my advisor and mentor, Dr. Zhang. His patience and constant help allowed me to persevere throughout my degree and make sense of a very challenging topic. He has pushed me not only to be a better student, but also a better writer, researcher, and investigator. The overall impact he has had in shaping my outlook on careers moving forward is immense.

I would next like to thank the other members of my thesis committee Dr. MacLeod, Dr. Janes, and Dr. Bazrgari. Dr. MacLeod and Dr. Janes have been incredible collaborators from the Gluck Equine Research Center and Equine Programs. They helped me understand the complexity of the equine system and allowed me to have access to all of the bones samples needed to complete this study. Their support and insight have made this study easier to understand and complete. Dr. Bazrgari, has been a part of the department since I was in my undergraduate studies, and has offered support and reassurance for me to pursue higher education for the past few years.

Next, I would like to thank my peers that were in a collaborative study on the same horses, Kathryn, and Angela. Their help in being liaisons between our joint colleges helped the transfer of knowledge and collaboration in this project run as smoothly as possible.

And finally, I would like to thank my lab mate and colleague, Lauren, for constant support and friendship throughout this degree.

TABLE OF CONTENTS

LIST OF TABLES

LIST OF FIGURES

CHAPTER 1. INTRODUCTION

1.1. Background

The equine industry has recently come to the forefront of research and model development as a recent, unexplained surge in racehorse deaths is happening across the country. Catastrophic injuries related to the fracture of proximal sesamoid bones (PSB) are constantly happening in racehorses and yet there is little known about this specific injury. These bones are located on the palmar or planter of the fetlock joints of each limb of a horse. The PSBs are an integral part of the suspensory apparatus, a collection of bones and ligaments that are located in the fetlock joint to provide stability to the joint and prevent hyperextension. For a long time, the vascular supply and arrangement within the PSB was not well elucidated as the organizational structure appeared different than other types of bones (i.e., long bones). With developing technologies, these vascular networks were finally revealed through imaging using radiopaque injection processes, in which the main arteries and veins of the suspensory apparatus are seen to penetrate sesamoid bones on the abaxial side and then arborize throughout the bone (Trumble et al., 1995 & Dunkerly et al., 1997). This revelation along with imaging techniques that can provide information on the internal structure of the bone provide ample information for new research studies investigating microstructure of PSBs in response to high-speed exercise and catastrophic breakdown injuries.

1.2. The Proximal Sesamoid Bone (PSB)

1.2.1. Nature of Breakdown

Breakdown of a proximal sesamoid bone can often lead to fatal injury of a horse with a number of different fracture modalities documented. These fractures can be categorized by the type, location and orientation of fracture lines or surfaces. For this purpose, the PSB is often divided into three spatial regions with the top third being the apical, the middle third being the midbody, and the bottom third being the basilar. Moreover, terms like axial and abaxial are used to refer to the proximity to the mid-sagittal plane. Abaxial is on the lateral aspect of the PSB, furthest away from the third metacarpal bone (MCIII), and axial is the location closest to the MCIII. The fracture types are typically classified as: 1) simple, if there is only one clear fracture line or surface; 2) comminuted, if there are multiple fracture lines or surfaces resulting in more than two pieces of bone segments; 3) avulsion, if a piece of bone is broken off due to tension of the adjoining soft tissue structure (Diab, 2017). Fractures that do not separate the bone into multiple pieces have a lower fatality rate, but they could still end the horse's racing career (Schnabel, 2018).

1.2.2. Attaching Ligaments

The location of PSBs and their role to stabilize a horse's legs during motion and prevent hyperextension require multiple attachments through soft tissues including the suspensory ligament, the straight sesamoiden ligament, the oblique sesamoiden ligament, the palmar inter-sesamoiden ligament, the palmar annular ligament, the collateral sesamoiden ligament, the cruciate ligaments, and the short ligaments to various muscles. These various forces can be seen in Figure 1.1 and Figure 1.2. Each of these ligament

structures applies force to the PSB during a normal gait cycle. The complicated nature of these attachments means that there are multiple yet constantly changing forces acting on the PSB during a gait cycle. This could help explain why PSB fractures are occuring in complex fracture modes. The PSB bone is relatively small in comparison with the size of its host horse but the forces acting on the PSB may not be small due to horse's weight coupled with acceleration factors duing runing, hence these multiple ligaments forces could be enough to push the bone past its ultimate yield strength to fracture.

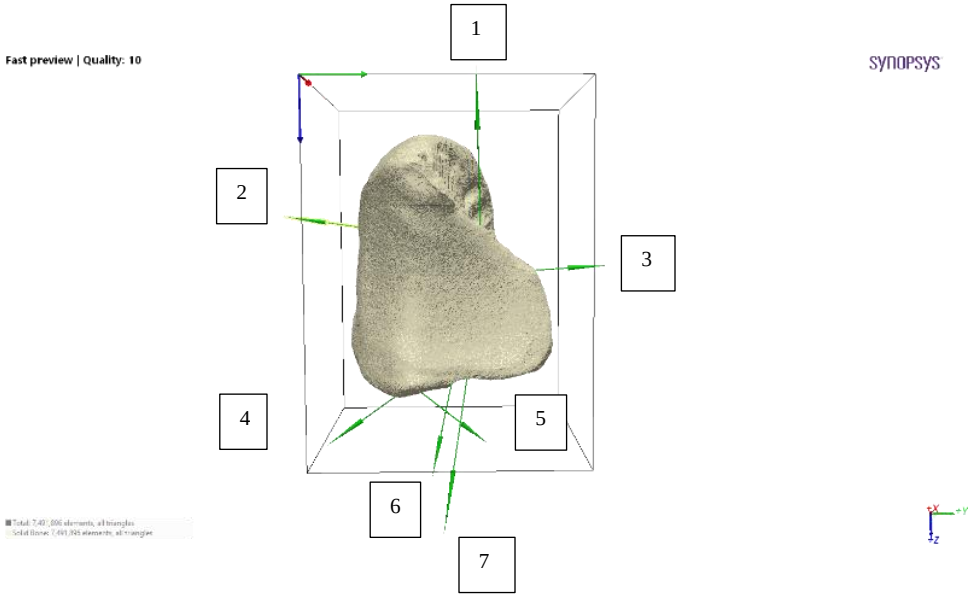

Figure 1.1 An anterior view of a 3D free body diagram of the equine PSB from the forces from ligament attachments. 1.) Suspensory ligament 2.) intersesamoidean ligament 3.) collateral ligamnet 4.) cruciate ligament 5.) short ligament 6.) straight ligament 7.) oblique ligament.

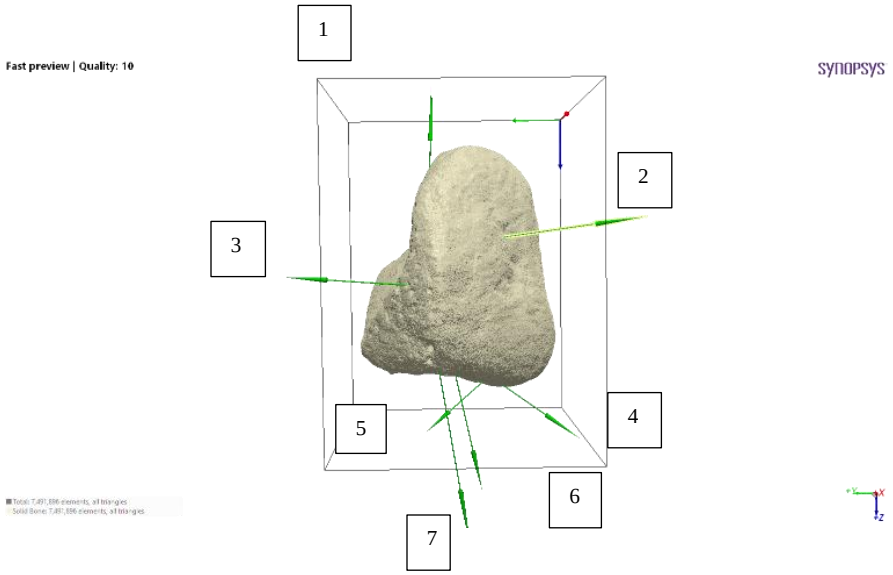

Figure 1.2 A posterior view of a 3D free body diagram of the equine PSB from the forces from ligament attachments. 1.) Suspensory ligament 2.) intersesamoidean ligament 3.) collateral ligamnet 4.) cruciate ligament 5.) short ligament 6.) straight ligament 7.) oblique ligament.

1.2.3. Internal Forces on the PSB

PSBs are responsible for preventing hyperextension of the fetlock joint as well as acting as a stabilizer for the suspensory apparatus. This is accomplished through pulling by various ligaments attached to the PSB, creating multiple mechanical forces in different directions. In other word, the PSB is subject to a complex loading condition with multiple force vectors. Each one of these vectors plays a role in the internal remodeling of the bone in a normal physiological-activity condition. During an extreme racing condition, however, these forces could lead to catastrophic breakdown of the PSB.

To be able to predict fractures from these external forces, detailed analysis is needed to elucidate how these force vectors affect bone growth and what states of internal stresses will be in terms of regions of compressive or tensile stresses and stress trajectories made of lines capturing the orientations of the resulting tensile and compressive stresses within the bone. As with any material, these external forces will

create localized areas of higher stress depending on the strength and orientation of the vectors. These localized areas of heightened stress can be a cause for failure in the material when the induced stress exceeds the strength of the material. In the case of a living material, i.e., the PSB, its strength may be changing constantly due to injury or other pathological reasons. This means that a set of force vectors, which may not cause any bone fracture in a healthy bone, could cause it to fracture catastrophically when the bone is under a pathologically affected condition.

An example of such an analysis is shown in figure 1.3, where internal stress trajectories and principal stresses are determined by performing a finite element analysis (FEA) of a 2D sagittal slice of a PSB located at the apex of the bone. The model was constructed using the same values for tensile forces of ligaments and angle of application as Thompson et. al (Thompson et, al., 1994). This model included the forced from the suspensory ligament, the straight sesamoidean ligament, and the oblique sesamoidean ligament. The FEA analysis was performed on a bone from a racehorse that sustained a PSB fracture and a horse that has not entered race training. The differences in the internal structure, show how the internal microstructure will remodel when subjected to racing stimuli. From this model we can see that the highest tensile stresses are shown on the non-articulating surface in areas where vasculature us known to enter the bone and the highest compressive stresses are shown in the basilar region where the vasculature has been shown to arborize, increasing the chance for vascular damage at these locations. This revelation of the vascular tree shows the possibility of vascular damage and how it could play a crucial role between the racing conditions the horse experiences and the mechanical integrity of the bone as race training continues. This modeling study provided

great insight into the nature of the microstructure of the PSB and how it could be put at risk through the effects of high-speed race training.

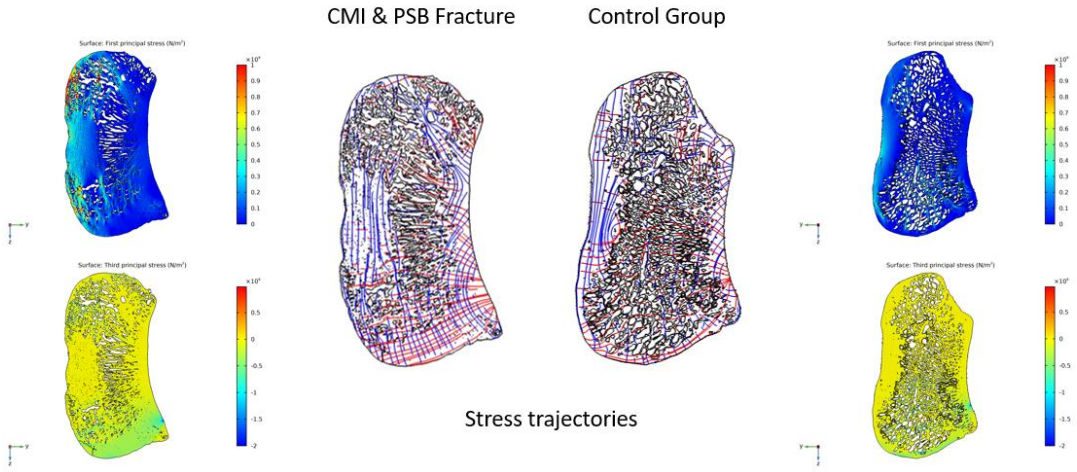

Figure 1.3 A simplified model of an FE analysis on a sagittal slice of a PSB to investigate stress trajectories and principal stresses. The figures in the top corners represent a map of the first principal stresses of the slices and the figures in the bottom corners represent a map of the third principal stresses. The red and blue lines on the figures in the middle represent the stress trajectories of the pricipal stresses.

1.2.4. Internal Structure of the PSB

1.2.4.1. Trabecular Pores

The anatomy of the PSB is unique in the regard that is does not contain some of the features that long bones have. The PSB does not contain a periosteum or cortical region. It does, however, possess an inner region of a trabecular network of cancellous bone mass. The architecture of the trabecular bone is often the result of bone remodeling in response to the external forces that the bone is subject to in a normal physiological

environment. The orientations of the trabecular truss structures usually follow the stress trajectories induced in the bone. The internal nature of the PSB and the reorganized porous structure from external loading can be seen in Figure 1.4. The articulating surface is shown on the right side of the individual bone slice and the palmar aspect is on the left side of the individual bone slice. The long axis of the ellipse of the pores in the middle of the slice of the bone from the fractured group are seen to be elongated and the number of pores is seen to be smaller when compared to the slice of bone from the control group seen in Figure 1.3. The pores from the control slice shown in Figure 1.3 are more circular in nature and do not have an elliptical shape. This shows how the pores remodel in response to the mechanical loading the bone endures from the race exposure. This remodeling changes how the bone handles external stimuli and the principle of Wolff's Law.

Internal imaging of these PSBs allowed for these trabecular networks to be visualized. With the ability to see how the bones react to their environment, the idea to analyze and compare these porous patterns between different racing groups gave way to forming the goal for this study. If these internal structures can be better understood, there is a hope to further understand the nature of catastrophic PSB fractures.

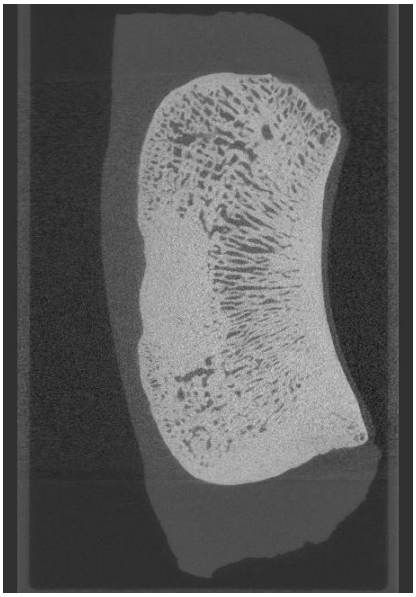

Figure 1.4 A sagittal DICOM image of a contralateral matched equine PSB from the PSB that has sustained a CMI & a PSB fracture.

1.2.4.2. Vasculature

All living bones need a source of vital nutrients and oxygen as well as a means for removal of wastes and debris to remain healthy. Not surprisingly, this source and means come from transport through the circulatory system. The PSB has main blood vessels that enter the proximolateral aspect on the non-articulating side of the bone and proliferate as they penetrate deeper into the bone. As the blood vessels disperse throughout the bone, they occupy some of the space between the trabeculae, making them vulnerable to mechanical damage.

It can be anticipated that a heightened internal stress, or an altered stress condition, could cause regional damage to the bone structure. As a result, it could injure or sever the nearby blood vessel leading to further pathological consequences in the bone such as localized areas of necrosis. This in turn could lead to a reduction of structural

integrity of the bone, thereby weakening the bone strength. For this reason, knowing how the vasculature runs inside the PSB could shed insight into how the chance of vascular vessel injury could be minimized or prevented totally. Specific spatial locations of the vascular pathways and how they arborize throughout the bone can be seen in Figure 1.5 below. This mapping helps up understand the flow of vital nutrients throughout the bone and how it maintains its structural integrity. Knowing specific locations of blood vessels can also help monitor the health of the bone. If a fracture is sustained where a vessel was just mapped, then there is increased likelihood that the soundness of the bone could be compromised.

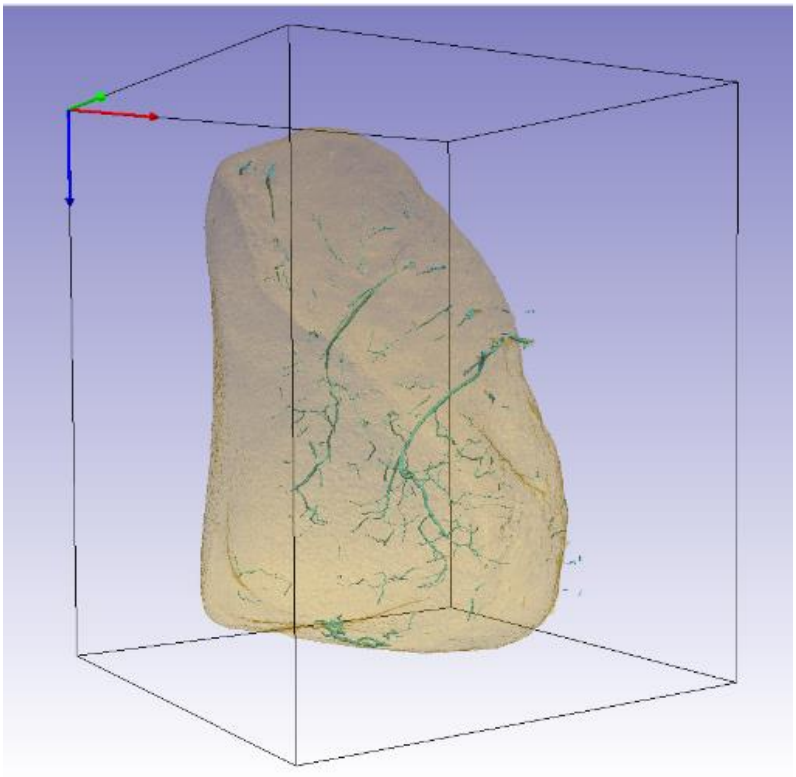

Figure 1.5 A 3D rendering of a PSB bone that was injected with BriteVU contrast agent in order to map the internal vascular tree.

This idea of localized defects coupled with the ability to see the internal structures of the PSB, gave way to the formation of this research idea. One research effort that was made was the analysis and mapping of the internal vascular tree of the PSB. Investigating the baseline vascular nature of these bones could prove beneficial information to understand the nature of PSB breakdowns. Goals of this project were to establish a method for using radiopaque injections within the bone to then be used in conjunction with imaging modalities to depict a visual of the internalized vascular tree. The forelimbs of horses euthanized for non-musculoskeletal reasons collected at the University of Kentucky Veterinary Diagnostic Lab (UKVDL) were flushed with multiple types of media through the median palmar artery to clear the blood vessels of the forelimb of any residual blood and blood clots. The remaining open vasculature was clamped except for the median palmar vein. The radiopaque contrast agent, BriteVu, was then injected into the median palmar artery for the contrast agent to perfuse throughout the limb and into the PSB. The PSBs were then dissected from the forelimb after the agent had set. The bones were then scanned using a μCT machine and the scans were then uploaded into Synopsis to render a 3D model. This model allowed for specific vascular entryways into the bone and specific blood vessel perfusion within the bone to be created and viewed in a capacity very rarely seen. A full rotational view of the bone can be seen with the blood vessels inside and also the surrounding extraosseous vessels in the soft tissue of the sample was obtained as seen in Figure 1.6. This figure shows the flow of blood in and around the bone.

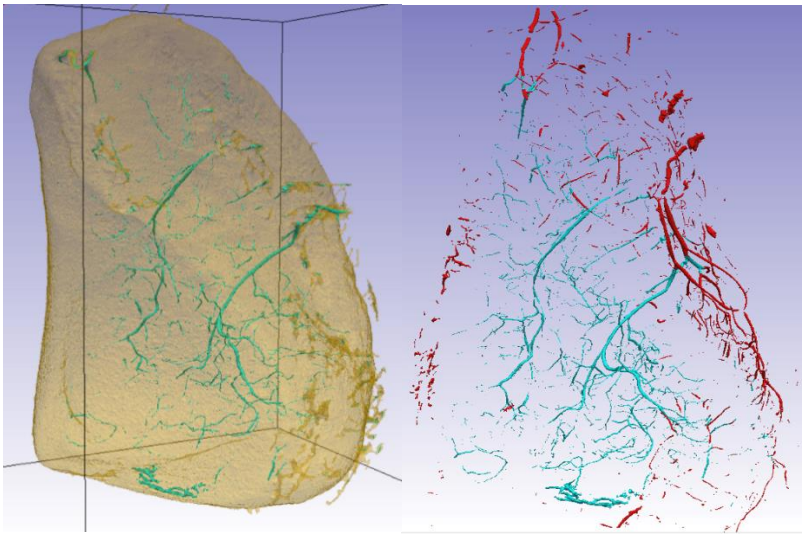

Figure 1.6 A PSB with injected BriteVu highlighting the internal vascular structures in blue (left). The external vessels (red) shows the flow of blood around the bone in the fetlock joint (right).

Overall, the study yielded beneficial information and images regarding the nature of the vascular tree of the PSB. Challenges were experienced in performing the perfusion, however. It was particularly challenging to perfuse into the smaller vessels because of the limited ability to pressurize the injection system, and with the limited perfusion, it was not possible to distinguish between non-perfused vessels and normal pore cavity space within the bone. The mapping did provide enough evidence to show that the main blood vessels enter on the proximolateral aspect, which branches from the medial and lateral digital arteries. The ability to be able to see within the bone and see specific regional distributions in relation to the arborizing blood vessels, helped form the idea to look internally at the internal porous network of the bone as well. If these blood vessels were compromised in any way, there could be a resultant indicator in the health of the bone in the specific region, which could present in the form of a structure abnormality. If we could develop a way to quantify the structure of the bone as a function of location, we

could then look to further connecting the differences as a function of vascularization as well (Price et al., 2021).

By analyzing the localized pore structure in different fracture areas, a more comprehensive outlook on the remodeling of the bone can be obtained. Rather than wholistic diagnostics, the localized analysis might be able to pinpoint how each area of the bone remodels and highlight the differences in pore structure. From there, a side-by-side comparison can show which areas might be at risk for fracture.

1.2.5. Research Gap and Rationale of Study

The fact that these PSBs are hard to access and repair in the body of the horse contribute to the fact that these breakdowns are often fatal. Another factor is that the complete nature of this bone is not as robust of that of a long bone, which complicates the fracture healing process. These circumstances not only increase the fatality for facture, but also shroud some of the information surrounding injury pathogenesis. A clinical CT machine would be able to capture in vivo processes, but it lacks the necessary resolution for us to discern the microscale trabecular bone structure and the circulatory vasculature. To meet these needs, a microCT machine is required. Using a microCT machine, however, means that the bones would have to be extracted and only postmortem studies can be done. It is worth pointing out that there may be differences in studies of live bones versus postmortem bones. For example, Cresswell et al. 2019 performed a study on the morphological properties of bone postmortem and found that an increase in the ratio of bone volume to total volume (BV/TV) was larger for horses that sustained a fracture and that the presence of an osteophyte, or bone spur, was also an indicator of increased likelihood of fracture (Cresswell et al., 2019). This contradicts the finding performed

with a larger 2D-radiographs of postmortem bones showing that the presence of an osteophyte was an indicator of decreased likelihood to fracture (Anthenill et al., 2006). This discrepancy suggests the tradeoffs between imaging that can be done in vivo versus post-mortem. With conflicting conclusions drawn from postmortem studies, this suggests that the need for *in vivo* is even more pressing. This would allow for the observation of the bone during remodeling and natural physiological processes to provide the most accurate picture of normal functionality.

Another study tried using this approach by comparing the features found in the microCT scans to the features found in radiographs. This particular study looked at the number of vascular entries into the bone from the suspensory apparatus but could find no strong positive correlations between the number of vascular entries and catastrophic fractures or racing performance (Lloyd et al., 2020). This might be because the number of main vascular entryways is not the best indicator to predict catastrophic fractures.

With this, there is even more evidence to look towards the internal remodeling process on the health of this bone, if the external vascular entryways are not providing enough data. With the thinking that this fracture is a cumulative buildup of fatigue due to continuous exposure to race training over time instead of an anomalous supraphysiological stress that causes fracture, the internal structure of the bone will capture this change over time. The porous nature of the bone will change over time and show the rigors and stresses of racing and training. At some point there will be a threshold for appropriate remodeling, and if that threshold is surpassed, then the bone will be at higher risk for failure. By analyzing the pore structure across different spatial locations throughout the bone and across different experimental groups, the goal is to

define that threshold of remodeling and better understand the response of the PSB and what could push it past that remodeling threshold.

1.3. Importance to the racing industry

Bone's main function is to provide structural support and locomotion to the body, whether human or animal. This function is currently seen to fail repeatedly with the prevalence of catastrophic breakdowns in the horse racing industry. In Kentucky, the equine industry generates over $6 billion and over 60,000 jobs. The equine industry is also notable in California and on a national level in Australia. This economic impact provides ample means for test subjects, research funding, and the ability to assembly a cross-disciplinary team to analyze this situation.

The advancement of bone screening procedures to monitor a horse's health has the potential to have a substantial impact on industry regulations. Certain standards may be put into place for the number of hours a week that a horse is allowed to train and the types of training it is allowed to undergo. Fortunately, this will have the horse's best interest in mind. A decrease in the number of horse fatalities will increase the number of races held each year, the amount of commercial revenue from the races, and the overall economic impact the industry. As the number of deaths decrease, so will the negative stigma that comes from the death of these animals. If these tests and standards show a positive impact on the industry and equine health, it could pave the way for other research studies in similar fields for human athletes.

This can translate into to looking into common bone-related injuries for humans in the sports industry as well. The sports industry generates even more economic impact in the United States and in the world overall. The sports industry has grown to generate

revenue not only from ticket selling to the sporting events themselves but also from the selling of merchandise for sports teams, concessions, and advertising sponsors (Gough, 2019). With an unforeseen injury to a crucial player, a team or franchise can experience a loss of revenue. Not only does the proposal of research into microdamage of bone certainly improve the health of the athletes directly, but it can also positively affect everyone involved. This can increase the number of stakeholders that would potentially be looking for this research and be well received within and outside the scientific community.

Medial tibial stress syndrome (MTSS), commonly referred to as shin splints, has been described as bone microdamage and can lead to other complications if not treated (Galbraith & Lavallee, 2009). This syndrome exhibits the same microdamage theorized to happen in the sesamoid bone of the horses. If advancement were made to improve the health of the horse's bone and reduce the risk of fracture in the racing community, these practices could then be translated into the human population. Preventative diagnostic measures could be put into place to regulate athletes' training regiments. If the identification of the presence of certain biomarkers for different stimuli is linked, then this could be translated into human healthcare as well. Whatever the case, there are still multiple physiologic areas of bone that are missing pieces to fully understand the osteogenic nature of this material.

1.4. Goal of Study

The goal of this study is to investigate the internal pore structure of the PSB and document any differences seen that can be attributed to high-speed race training, not only as a function of race training, but also as a function of spatial location within the bone.

There is expected to be a difference between the structures from the control group and the three (3) different populations that have been exposed to the race training, but there is hope that a physical marker in the pore structure can be identified within the PSB fracture group. This will highlight which areas of the bone could be prone to fracturing and allow for equine specialists to work on preventative action to stop these markers from developing in the first place. For a better understanding of the nature of this project, a thorough research and literature review was conducted on the biology, physiology, and pathology of bones and how they remodel and sustain structural integrity. From there the scope was narrowed to focus primarily on the specific nature of PSBs and what previous experiments have been conducted in order to fully shape the ideals of this study.

CHAPTER 2. LITERATURE REVIEW

2.1. Introduction

Bones are a unique connective tissue found in various forms in our body. They serve many functions. Primarily, they form our body's physical structures, protect various organs, and provide a means for locomotion. Secondarily, their roles include serving as a reservoir for bone marrow, stem cells, minerals, and other biochemical species and as a controller for endocrine homeostasis as well as acid-base balance. Bones hold a wealth of information to be discovered. With constant advances in our understanding of the role of bones in our body and the related physiological processes, this chapter provides a literature review of all the relevant biological aspects of bones.

2.2. Elements of Bone Integrity

2.2.1. Cellular Roles and Function

Bone possesses a unique ability to remodel itself or change its structure and shape through regenerative processes in adaption to the physical environment it is in (Hadjidakas and Androulakis, 2007). Figure 2.1 shows a depiction of the remodeling process with the specific types of cells and their function in the process. Bone tissue contains main three types of cells that contribute to this remodeling process and the overall health of the tissue: osteoblasts, osteoclasts, and osteocytes (Mohamed, 2008).

2.2.1.1. Osteoblasts

Osteoblasts are cells that specialize in osteogenesis or the creation of new bone tissue. They are controlled by different chemical factors and exhibit distinct functions in

their immature and mature states. Studies show that immature osteoblasts have a part in the regulation of osteoclast formation, by their expression of RANKL, whereas mature osteoblasts do not. Osteoblast differentiation is governed by a transcription factor known as runt-related transcription factor 2 (RUNX2). Knockout mice for RUNX2 show a complete lack of mineralization of the bone and a very porous skeleton. This further demonstrates the functionality of mature and immature osteoblasts. Since immature osteoblasts are still created but cannot mature due to lack of RUNX2, osteoclast formation still occurs as well as bone absorption, therefore, leading to this heightened disease state. Parathyroid hormone (PTH) the counterpart to calcitonin, binds to receptors on the osteoblasts to inactivate them (Langdahl et al., 2016). PTH is secreted from the parathyroid gland in response to low calcium levels, making the use of calcium for bone creation inhibited and increasing the plasma levels of calcium.

2.2.1.2. Osteoclasts

Osteoclasts are large multinucleated cells that absorb of dead or unwanted bone, normally during growth and healing. The remodeling process is still a heavily researched areas as new developments such as the role of paracrine and autocrine cytokines, gene expression, immune cells, and hormones in the remodeling process are still being discovered (Raggatt and Partridge, 2010).

The differentiation of hematopoietic stem cells into osteoclasts and mesenchymal stem cells into osteoblasts and osteocytes are the main pathways that can be altered by chemical signals to change the populations of the aforementioned cells. Osteoclasts are heavily stimulated by the receptor activation of the NF- kB ligand (RANKL) and colony stimulating factor- 1 (CSF-1/M-CSF, which modulate everything from survival to

expansion and recruitment (Eriksen, 2010). Studies have shown that mice with missing genes to codes for these cytokines present the development of osteopetrosis (heavily dense and compact bone), showing that these receptors are vital in the stimulation of bone reabsorption. Osteoprotegerin (OPG) has also been found to be an antagonist for RANKL receptors, thereby reducing osteoclasts activity and promoting osteogenesis. The ratio of RANKL/OPG presentation is a key factor in regulation in osteoclasts activity in the remodeling process and is also an indicator of disease states such as osteoporosis and osteopetrosis. Hormonally, osteoclasts are regulated by calcitonin which is secreted by the parathyroid gland. When calcium levels decrease, calcitonin secretion is increased, which binds to the receptors of the osteoclasts to inhibit their function and decrease the reabsorption of bone (Raggatt and Partridge, 2010).

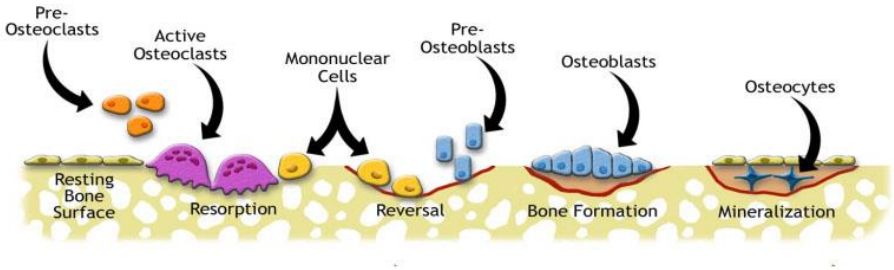

Figure 1.6 A simplified overview of the biological cascade of bone cell interactions (Maffioli & Derosa, 2017).

2.2.1.3. Osteocytes

Osteocytes are a special subclass of differentiated osteoblasts that contribute to the internal structure of the bone tissue and have thought to be a key component in coordinating the remodeling process. The remodeling process is more than just the

natural day-to-day processes of bone tissue. The phenomena of absorption and formation have been shown to be able to be manipulated not only by internal processes but also external forces. Julius Wolff developed a theory that bone will remodel itself to become stronger or weaker under the application or absence of loading. While thought to be a straight-forward principle, research now shows that this law varies in each individual based on gender, age, body mass index, and disease state (Teichtahl et al., 2015).

For bone to remodel in response to a given load, the load must be perceived, the cells must be activated, and then the growth occurs. The first step, perception, happens through a process called mechanotransduction that is still not completely understood. It is known that these applied loads are recognized by some sort of stretch receptor which then activates either a single cell or a group of surrounding cells, but the complete signaling cascade has not been detailed at this point. It has been theorized by some that the osteocytes play a role in sensing these stimuli (Bonewald, 2011). Osteocyte research has been gaining traction in more than one facet of the bone remodeling process. In an extracted avian osteocyte, it was shown the osteocyte would express RANKL on its dendritic processes, thereby supporting the notion that osteocytes could recruit osteoclasts to certain regions of the bone (Tanaka et al., 1995). Furthermore, it was noted that apoptotic osteocytes released smaller apoptotic bodies that contained RANKL that recruit osteoclasts to localized sites (Bonewald, et al., 2011). This research of osteocytes mediated differentiation of osteoblasts and mesenchymal stem cells reinforces the idea that osteocytes could be a prominent coordinator of the different activations for bone remodeling.

2.2.2. Structural Composition and Significance

Aside from these bone cells, bone is comprised of type I and type III collagen fibers infused with minerals. Type I collagen is the most prevalent and is the primary organic component of the matrix and type III collagen is found in the reticular fibers of specific connective tissue areas. The hierarchy of the composition of bone and how the collagen fibers orient can be seen in figure 2.2. The composition, formation, and structure of such collagen infused minerals can vary notably not only in different bones in the body, but also in different regions in the bone. Bone structures can be grouped into two types: cortical and trabecular bone (Clarke, 2008). Cortical bone is dense and normally forms the outer surface of the bone, protecting the internal cavities. It gives bones its smooth surface and contributes to the main function of supporting loads and protecting organs. Trabecular bone is the porous bone typically found within the internal cavities of the bone. Red bone marrow fills the space of the trabecular pores.

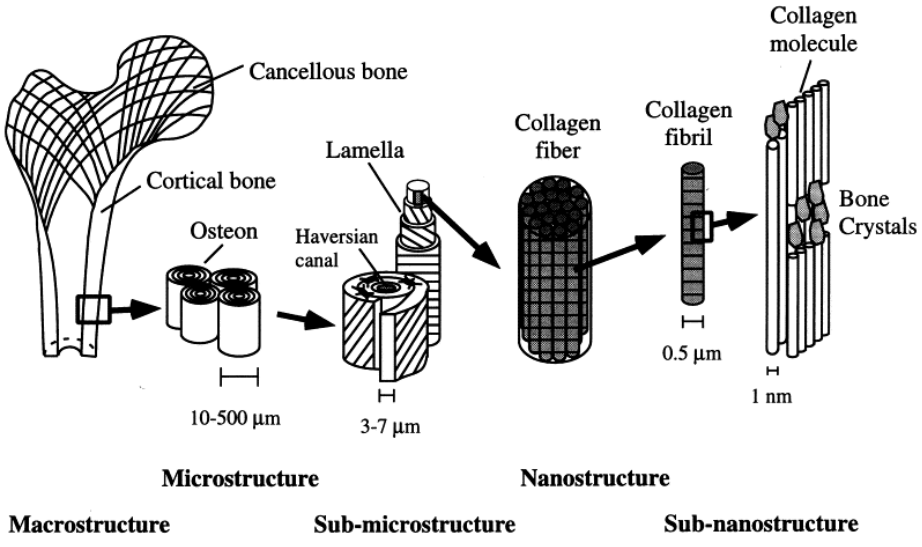

Figure 1.7 Hierarchal structure of bone (Rho et al., 1998).

Cortical bone has a denser and stronger structure than its trabecular counterpart. It normally forms the outer layer of bone providing structural support. For example, the diaphysis of long bones is primarily made of cortical bone, which forms the outer shell of the yellow marrow space where fat is stored within the bone (Augat and Schorlemmer, 2006). The fundamental structural unit of the cortical bone consisting of concentric bone layers called lamellae is the osteon, which forms the Haversian system on a higher structural level. Haversian canals are at the center of the osteon and are surrounded by concentric layers of lamellae, or compact bone tissue. The canals allow for blood vessels and nerve fibers to disperse throughout the cortical region. The neighboring osteons are connected through smaller channels called canaliculi. The Volkmann's systems run perpendicular to the Haversian system and connect the blood vessels and nerve fibers vessels outside of the bone.

Trabecular bone, named after the trabeculated nature of the bone tissue that comprises it, consists of the same materials as cortical bone, but functions in a different capacity. The pores within the trabecular allow for the dampening of stresses on joints and higher flexibility than cortical bone. Since, the pores are also filled with blood vessels, this make them the site for high metabolic activity and is a main site for the bone to receive vital nutrients. Trabecular bone is arranged in a mesh-like pattern in which each strand of the mesh forms along a stress loading line. Trabecular bone is normally found in the epiphysis and metaphysis of long bones and the inner cavities of most bones. Filling the meshwork of the trabecular is red marrow, the hemopoietic site for all blood cells. The Volkmann's system is also present within the trabeculae of bones, allowing for further blood vessel (Kreider and Goldstein, 2009).

2.2.3. Bone Vasculature

While the inner vasculature channels are important for material exchange of oxygen, glucose, and waste, the principal nutrient artery and vein are equally important for providing a channel for the bone to connect with the systemic circulatory of the bone. Vasculature channels can most evidently be studied in the long bones of organisms, and while the specific nature of the organization varies among mammalian species, a general structure can still be acquired.

The primary artery, and likewise the vein, enters in through a foramen close to the metaphysis end of the bone, from there it branches off into arterioles and eventually capillaries as it penetrates deeper into the medulla, the central cavity of the bone shaft. The medulla cavities capillaries then connect with the end-terminal capillary system at the epiphyseal plate. The ends of the bone contain an epiphyseal arteriole channel and an epiphyseal venous channel, one at each end. These capillary systems at the ends of the bone are prolific within the bone and do not venture to the outside of the bone as much. The capillaries along the diaphysis of the bone however are very developed throughout the periosteal and are highly connected to the circulatory system. These capillary systems on the surface of the bone arise because there is a lack of firmly connected muscles and other connective tissues, unlike at the end of the bones (Fung, 1993).

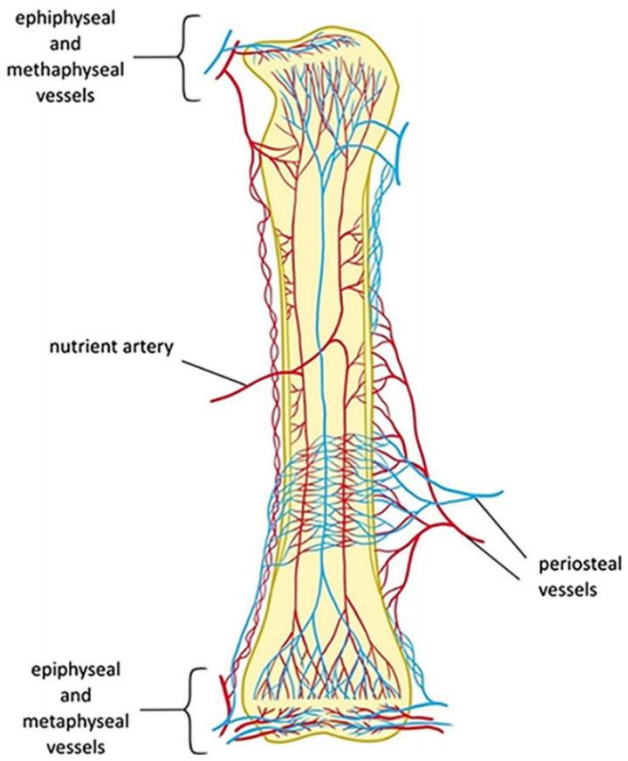

Figure 1.8 Vascular representation of vessels within a long bone (Filipowska et al., 2017).

Understanding the nature of these networks is vital for understanding certain pathological diseases and how they could arise from a compromised vascular system. This system not only provides nutrients and oxygen to the bone tissue itself but also the bone cells, specifically the osteoblasts, within.

Reduced blood flow, causing ischemia, has been shown to decrease osteoblast activity and, in turn, have an adverse effect of stimulating bone resorption (Marenzana & Arnett, 2013). This poses a problem because if this is not treated then a bone has the potential to become weak or osteoporotic in a certain region (Marenzana & Arnett, 2013). If this region is one that is commonly subjected to stresses and strains then it may not be able to withstand its normal loading, thereby resulting in a fracture. As seen in many

elderly patients, fractures of the hip or pelvic area can be fatal. This reduced blood flow continues to work against fracture repair as medicine and nutrient flow will still be limited to that area. Furthermore, the osteoblasts will still be in an inhibited state, decreasing the chance of bone remodeling to help repair the fracture. Understanding how to improve vasculature networks and angiogenesis could prove to hold insight into helping treat bone disease (Marenzana & Arnett, 2013). This parallels some of the preliminary work provided in the introduction chapter. The vascular tree mapped within the PSB can hold insight into which areas of the bone are more vascularized than others, meaning that we can pinpoint which areas are subjected to higher levels of bone remodeling. Also, if we can establish a baseline model, we can compare any future vascular trees of PSBs to the standard to isolate areas that could have damaged vascular pathways and may be more prone for a fracture to occur in that area.

2.3. Bone Physiological Processes:

With the composition and functionality of bone have discussed, we now turn to the physiological processes that transpire within the bone. It is necessary to understand the ability of each of these processes because at least one is always affected in pathophysiological states, making it easier to understand the nature of the disease states and biomarkers later discussed in the paper.

2.3.1. Bone Remodeling

One of the fundamental physiological processes in bone is the bone remodeling process. Stated earlier, this process deals with the activation of the osteoblasts and osteoclasts within the bone. Activation of osteoblasts corresponds with bone formation

and activation of osteoclasts correlates with bone absorption. It is through this ratio of formation to absorption that bone remodeling happens. If formation is greater than absorption, then there will be net bone growth. If formation is less than absorption, then there will be net bone loss. If formation equals absorption, then the bone is in a state of dynamic equilibrium with no net bone growth or loss (Clarke, 2008).

The need for understanding this remodeling process is highly important because it is a precursor for bone health. Thus, certain biomarkers such as C-terminal telopeptide (CTX) and N-terminal peptide (NTX), telopeptides of Type 1 collagen, can be used to measure osteoclast activity because they are byproducts of bone as it is broken down and reabsorbed (Walsh, 2015). For bone formation, the procollagen 1 intact N-terminal propeptide (P1NP) or procollagen 1 carboxy-terminal propeptide (P1CP) biomarker, a byproduct of collagen formation, have been used to monitor bone formation rates (Shetty et al., 2016).

2.3.2. Vascular Physiology and Pathology

Currently, research has shown that there are certain cell signaling pathways and growth factors that have a positive influence on angiogenesis in bone. One growth factor that has been frequently studied is the vascular endothelial growth factor (VEGF). VEGF is a hallmark component for the formation and maintenance of blood vessels, making it essential for most physiological processes to sustain a normal homeostatic state and for cells and tissues to receive vital nutrients. The VEGF family consists of about seven (7) different members currently known, all of which contribute to the function of either vasculogenesis or angiogenesis. VEGF-A has a variety of functions including regulation of the permeability of vasculature, macrophage cell migration, and tumor angiogenesis,

all of which have been shown to affect the health of a bone either directly or indirectly. (Shibuya, 2011).

While it is known that the VEGF-VEGFR (VEGF-Receptor) system plays a part in the pathology of tumor angiogenesis, it is by no means understood in terms of which family members activate which signaling pathways. VEGF-A, VEGF-C, and VEGF-D have all been identified as ligand signaling components of pathological angiogenesis, but metastatic tumor cells that have migrated to the lymph nodes express high levels of VEGF-C and VEGF-D. With this information, clinicians have sought to utilize anti VEGF-VEGFR drugs in the hopes of stabilizing effect treatments to tumor and cancer growth (Kim et al 1993). In murine models, treatments of a VEGF-A neutralizing antibody suppressed tumor growth and halt tumor angiogenesis. These specific antibodies targeted the VEGF-A that were secreted by the tumor not by the native VEGF-A created by the murine bone marrow. When this model was transferred over to a human model, however, the same results were not shown, except for in renal cancer.

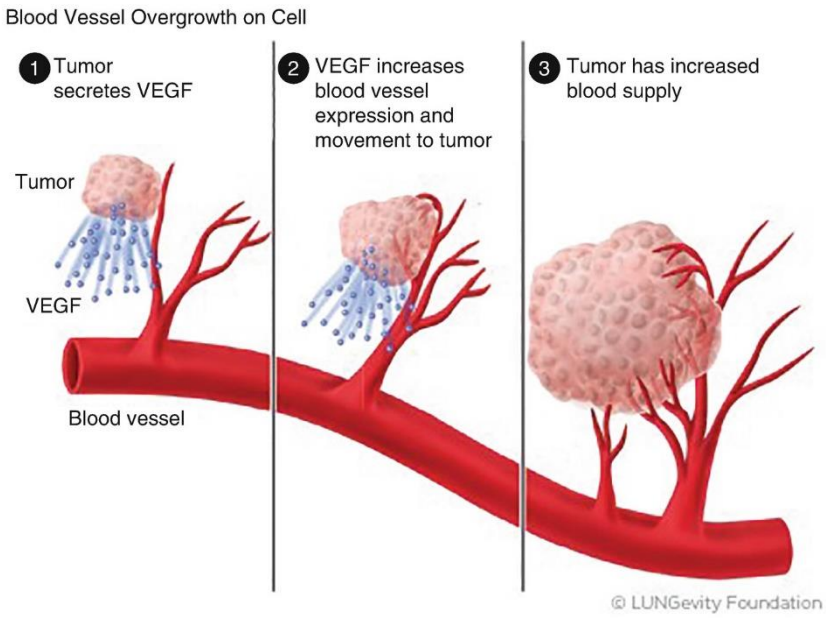

Figure 1.9 A tumor secreting VEGF to endothelial cells to increase its incoming blood supply (Oliver & Waxman, 2019).

While there are some side effects to this anti VEGF-VEGFR therapy such as hypertension, proteinuria, arrhythmia, and others, this shows to be a promising field of research for the possible treatment of cancer and tumor cells, both of which can influence the overall health of a bone. With more information and fine tuning of the therapy, there holds a chance that human models can then achieve the same outcomes as the murine models (Shibuya, 2011). It is still unknown why this effect is seen in clinical human models as opposed to the murine models. A collaboration between this and other pharmacological target attributes, such as high cell division, could prove to work better in human models as it neutralizes the VEGF-A which contributes to the high vascular development, but limits it to regions only in high cell division areas, areas normally associated with tumors. This would serve to try to further narrow the drug delivery to focus on adverse pathological angiogenesis. This can translate into new studies on bone health by looking at the effects of angiogenesis on the nutrient supply to the bone.

In an experiment looking at the vasculature of mice in exercised groups and sedentary groups, a noticeable difference was observed in the groups. Exercised mice exhibited a noticeable increase in the number of blood vessels and VEGF in the exercised bone, along with an increase in the receptor VEGFR1. To further isolate the effects of VEGF, a VEGF blocking antibody was administered to an exercised group of mice, decreasing the production of VEGF and the activity of the receptor VEGFR1. It was shown that this antibody completely stopped the vasculature adaption in the stimulated regions of the bone, producing a vasculature network that now resembled one that was closer to the sedentary group. This highlights the importance of this cellular pathway for understanding the nature of VEGF as one alternation can have such a monumental impact on bone healing and the activity of osteoblasts (Yao et al., 2004).

Since VEGF is such a key component in vasculature health and bone health, research has been done into the homeostatic mechanisms put in place by the body to try to maintain this necessary level of this biological factor. When there is an injury or a loss of blow flood to an area of bone, tissue and cells lose nutrients and bones start to lose integrity. When this happens, the area becomes hypoxic and an increase in the transcription of hypoxia-induced factors (HIFs) occurs. HIF-1a specifically has been shown to have a direct relationship to the increase of VEGF. This is most commonly seen in endochondral bone as the presence of HIF-1a stimulates the permeation of blood vessels into the adjacent cartilage. In other places, such as fracture lines, this phenomenon can also be observed, suggesting that hypoxia is a major environmental factor to trigger the growth of vasculature and bone. While this is an important pathway, it is not the only one. When deleting the gene for producing HIF-1a, there was only a

slight decrease in the production of VEGF, implying that there could also be VEGF regulators that are hypoxia independent. Manipulating the expression of E3 ligase VHL (VHL) was shown to have a direct effect on the expression of VEGF as well (Riddle, 2009). VEGF has been shown to completely cut off angiogenesis when its receptor has been blocked, meaning that it is a very important factor in the body since it modulates the supply of nutrients. A factor containing this much influence in the body might be highly regulated and have multiple pathways to moderate its creation to maintain homeostasis. If these pathways can be induced or manipulated within the bone itself, then the rate of bone turnover can also be manipulated. This would hold great benefit in being able to maintain the health of targeted bone. This may not be the only way to target bone's health; our own body has been shown to have cell pathways that we can use to affect the overall health of the bone as well.

2.3.3. Immune Cells

Recent developments have been made in the influence of the immune system in the bone remodeling process. A sensible notion because naïve lymphocytes are created in the marrow of the bone. B lymphocytes even mature and develop in the marrow before moving to secondary lymphoid organs. These cells spend the majority of their developmental life in the bone. It has been shown that mice lacking either of the lymphocytes, T or B, exhibit osteoporosis. B-lymphocytes have been shown to produce a large amount of the body's OPG, which contributes to deactivating osteoclasts activity. Without this restrain the osteoclasts are overactive, absorbing bone at an increased rate. The T-lymphocytes' role in maintaining normal bone remodeling levels is unclear, but mice models that are T-lymphocytes deficient exhibit osteoporosis. It is proposed that the

interleukins and other cytokines released by the T-lymphocytes cooperatively work with the lymphocytes to stimulate OPG production.

These combined findings hold promising aspects for pathology as an increasing number of links between body systems seem to play a part in some disease states of bone. While on one hand, this may complicate the actual nature of the disease, on the other hand it holds that there may be more than one way to treat these diseases. If one pathway is blocked, another one may open as new research on cell signaling develops. This will also allow an increasing number of professionals to weigh in on the subject at hand. An endocrinologist could potentially bring insight to a problem with their in-depth knowledge of hormones that an immunologist may not have thought of with their specialty being immune cells, and vice versa. This will allow for a broader and more in-depth range of articles and scholarly journals to be produced as well, continuously linking the professionals of the scientific field.

2.3.4. Endocrine Influence

While bone does serve primarily to support our body and provides a means for locomotion, it has become increasingly clear that bone holds much responsibility to the body's physiological and homeostatic processes. This further research into this staple body biomaterial can hold insight into the functioning of the body as a whole.

A study performed by Gunter and Rosen (2012) showed bone having a prominent part in hormonal and endocrine processes. Bone secretes a unique to self-protein, osteocalcin (OC), to modulate glucose tolerance, testosterone production, and signal osteoblasts. Osteocalcin knockout mice were shown to have increased adipose tissue and

irregularity in their glucose maintenance. This was due to the denaturing of a phosphatase enzyme that normally binds to a common insulin receptor. When the insulin cannot be activated, this causes a shift towards hyperglycemia in the individual (Gunter and Rosen, 2012).

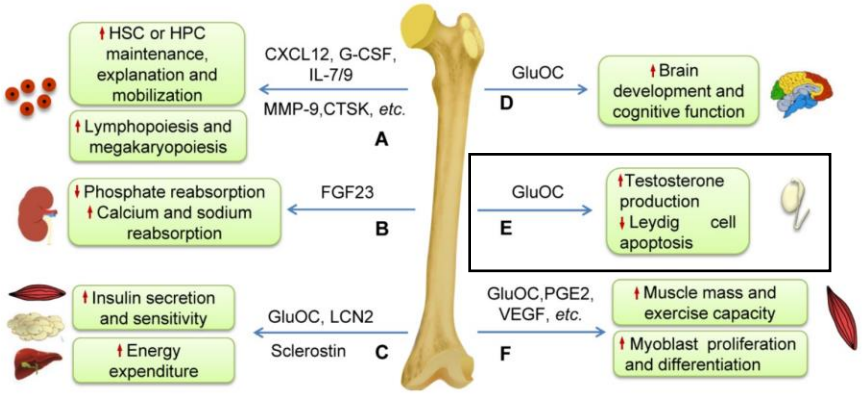

Figure 1.10. Bone's relationship with endocrine axes and physiologic states. The box highlights the Osteocalcin interaction with testosterone (Su et al., 2019).

A notable revelation mentioned in this study is that this active osteocalcin model was ignored for several years when the protein was first discovered. This is because at an initial glance, the knockout of the osteocalcin gene yielded no noticeable change in phenotype (Ducy et al., 1996). This alludes to the fact that we may have initially glossed over discoveries revolving around the function of bone because it did not affect the bone's primary function to support the body.

Osteocalcin was also shown to induce the secretion of testosterone by Leydig cells in the testes, creating an overlapping sphere between the reproductive hormone processes and the bone hormone processes. This not only poses an implication in the hypothalamic-pituitary-gonadal axis and fertility but could hold other deleterious effects to the bone itself (Ramasamy et al., 2015). Osteoporosis is a prominent cause for bone

fractures and can be exacerbated by low estradiol levels (primarily why this is seen in menopausal women) (Ji and Yu, 2015). Estradiol is primarily secreted from the ovaries in women but for men it is secreted from the Leydig and Sertoli cells in the testes. Testosterone produced from the testes can be converted into estradiol by the enzyme aromatase (Hess 2003). With the production of testosterone increased from osteocalcin, this could cause negative feedback on the hypothalamic-pituitary-gonadal axis. This could possibly have an effect on the levels of estradiol in the body if prolonged OC formation occurred. This begs the question if a decrease in osteocalcin has any effect on the onset of osteoporosis in these osteocalcin deficient individuals. While these studies primarily focus on forming the link between testosterone production, this highlights the fact that bone is still a novel component of the body that we are still learning about and there is still ample room for discoveries and research in this area.

2.4. Relating Mechanical Exposure to Pathological Defects:

With the pathways of bone remodeling sufficiently developed, it is now time to take a look at specific experiments that have sought to manipulate these signaling pathways, specifically ones stimulating osteogenic activity. With bone disease being a notable malady in today's healthcare sphere, these experiments provide valuable information and potential leads for future research investigations and directly connect bone's ability to adapt to its ability to bear loads.

2.4.1. Mechanical Properties of Bone

With its complex and heterogeneous structure, bone responds to and handles mechanical loading in a variety of ways. Bone is characterized as having both an

anisotropic and viscoelastic nature. This means that for a given loading, the mechanical properties, such as modulus and fracture strength, will be different in different applied directions and these same mechanical properties will vary as a dependent of the time and rate of loading, respectively (Geissler et al., 2015). This can be seen in long bones as they have numerous fracture patterns such as traverse fractures from tensile loading, oblique fractures due to compressive loading, spiral fractures from torsional loading, and butterfly fractures from bending. Certain pathological defects with bone mineralization make individuals more prone to experiencing a fracture, however. In the case of over-mineralization, the bone may become overly stiff and act as a brittle material, reducing the pliable nature of bone. With decreased mineralization, the bone becomes less dense and weaker, reducing the strength of bone (Tzaphlidou, 2008). Understanding the ways in which bone responds to loading will help characterize the root cause of failure for a given disease state and offer better information on preventative measures for the fracture.

A disease state that exemplifies reduced mineralization is osteoporosis, a disease characterized by excess bone loss and a significant loss in mechanical integrity. Osteoporosis has become the most common disease in the aging generation, affecting a majority of the elderly population worldwide. Bone mineral density (BMD) is a common marker used for determining the onset of osteoporosis, but current research shows that BMD may be becoming a decreasingly viable marker to use for detection. BMD does not entirely represent the variability in bone fragility, leading to a missed detection of an osteoporotic fracture in a majority of cases (Bolotin, 2007). Having reliable biomarkers to track in the bone composition or surrounding tissue could be the most effective way on monitoring fracture risk. With the current debate on which standards hold effective in

fracture prediction, a further probe into this research area is heavily warranted to push science in the right direction for healthcare monitoring and delivery.

2.4.2. Exercise and Physical Therapy and Fracture Risk

A core controversy current surrounding the mechanical properties of bone is the debate of exercise. Hughes delves into the facts surrounding bone biomechanics and exercise loading on the osteogenic processes of aging individuals (2016). This perspective is one that supports exercise as an osteogenic process, but not a standardized one. As bone ages, it loses mineral composition and sensitivity to mechanical loading, as well as a loss in endocrine functions that suppress the function of osteoclasts. Exercise can be beneficial especially for the physical therapy of the aging generation, but even more so if the individual patient characteristics are considered. Furthermore, with the help of dual-energy x-ray absorptiometry (DXA) to further comprehend the 3D structure of the bone, exercise regimens can be tailored to help increase osteogenic processes in the bone and hopefully reduce the risk of fracture (Hughes et al., 2016).

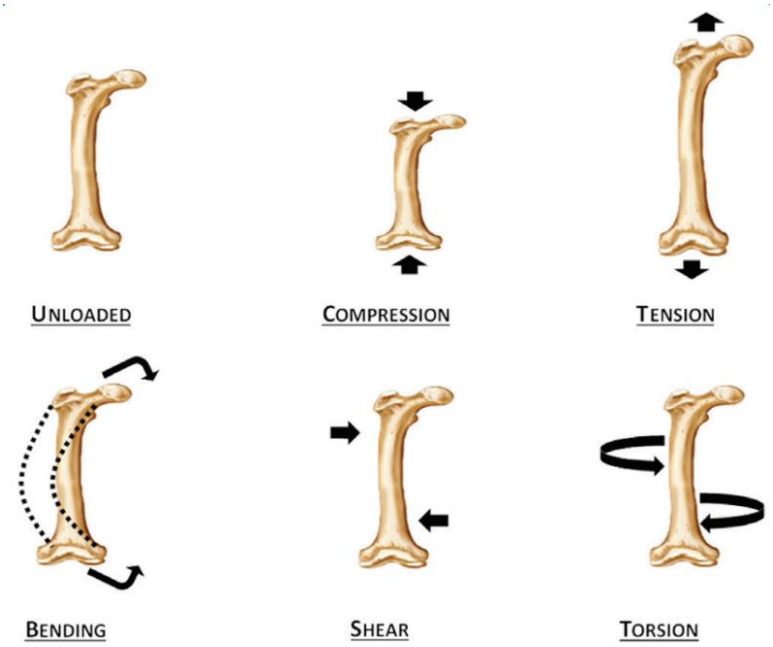

Figure 1.11 Representation of the different loading modes of bone (Hart et al., 2017).

While this perspective does offer some novel insights, such as ways to tailor the exercise to induce osteogenesis, it does acknowledge its limitations of not considering current, more precise ways of measuring bone density and structure (Hughes et al., 2016).

Originally thought to be the most effective way to induce osteogenic, high-impact loading may not be the answer for stimulation of bone growth in the elderly. As bone ages, it becomes desensitizes, therefore, to elicit the same responsiveness as seen in younger bones, a higher loading must be applied. This increases the risk of fracture and decreases the safety for the individual in these environments, creating a need for a smarter way to provoke osteogenesis in desensitized bone (Hughes, et al., 2016). While each side has a nuanced opinion on exercise, they both maintain that exercise could be a positive method if used correctly. From here, an idea that sprouts could be that there is a

need for multiple models of exercise. Each tailoring to a different bone demographic, but still playing to manipulation of the osteogenic pathway.

Promising models for induced osteogenic activity include rest-interval exercise, vibrations, and unorthodox loading. Inserting a rest period, between loading cycles showed increased bone formation at lower loads. Low-amplitude, high-frequency vibrations were shown to increase bone formation in some animal models but inconclusive results in human model. By applying unorthodox and unique loading cycles to the bone, an increase in bone formation was shown (Hughes et al., 2016).

In an equine model, the incorporation of a rest-interval proved to hold high benefits in the remodeling of bone. The remodeling process is stifled during race training periods and accelerated during the rest periods. This shows that the concept of continuous, strenuous training may causes the accumulation of microdamage quicker because the bone is not allowed to rest and recover and have ample time to remodel to the stresses that it was experiencing. While the exposure to this tine of stress is necessary, it is even more necessary to allow the bone to appropriately remodel in order to become stronger to withstand this loading. Another interesting factor was that the exposure to this race training earlier in life rather than later actually increased the longevity and success of a horse's career. Starting horses at 2 years of age could be important to exposure the bone to the stress of this high-speed racing and allow it to gradually grow and remodel over the years. Horses that started racing later in life saw an increase in their risk for fracture (Martig et. al., 2014).

Some considerations around the nature of vasculature and exercise however seem to be uninvestigated. While it was observed that these high impact loadings were

detrimental to the health of the bone, was this due to a single impact that imparted a force greater than the yield strength of the bone or was it an accumulation of impacts that caused microdamage to certain areas of vasculature. While these two causes yield the same outcome, they alter the way we must think about bone as a whole and, specifically, in individuals who experience this type of high-impact interval loading. This could lead to future healthcare and physical therapy standards for athletes as well as others. Furthermore, the results of the positive impacts of vibrations on the bone seem to be unclear. This leaves room for the comparison of the nature of these experiments as well as looking at the specific demographics that were used in the studies.

2.4.3. Cyclic Loading and Anabolic Activity

Rubin et al. hypothesized that the effects of vibrations could combat osteoporotic bone loss. In a study with seventy (70) postmenopausal women, some placebo, and some receiving 20 minutes of vibrations per day, there was a significant difference in the BMD in the spine and femur of the placebo and non-placebo group. The results show that while the vibrations may not induce anabolic activity, they do prevent catabolic activity. These results are not the same across different demographics, however (Rubin et al., 2004).

In populations where the individuals were still experiencing bone growth, children with cerebral palsy, the effect of the vibrations was shown to induce osteogenic processes in the cortical region of the affected bone (Wren et al., 2010). While the vibrations did not affect all parts of the bone, the increase in cortical surface area favors a to translation to a reduced risk of fracture. Ward, however, was able to produce anabolic effects in the trabecular region of the tibia and spine in his clinical trials of disabled ambulant children (Ward et al., 2004). This information is now corroborating this method

across disease states and different age groups for reduced catabolic activity in bone regions. While some populations tend to respond better with not just a reduction in catabolic activity, but also an increase in anabolic activity, induced vibrations are proving to be a more reliable way to produce noninvasive pharmacological effects for patients. This could prove beneficial for those who cannot or will not comply with pharmacological means for reducing bone loss and prove to be an efficacious and safe way to combat bone loss and the risk of fracture in high-risk populations.

The notion of stimulating anabolic activity in growing bone was tested by Xie et al. using eight-week-old BALB/cByJ mice, separating them into four groups of control, age matched-control, whole body vibrations (WBV) at 45Hz for 15 minutes a day, and WBV that was interrupted every second by 10 seconds of rest. Osteoclastic activity and bone formation rates on the endocortical surfaces were then measured. The results showed that after 3 weeks, the WBV mice had decreased osteoclastic activity in the bone trabecular metaphysis and epiphysis of the tibia than that of the age-matched control group. The group with rest periods failed to show cell potentiation activity, but both the WBV groups, with and without rest periods, did not show any detrimental effects on bone integrity parameters (Xie et al., 2006). This further identifies the method of subjecting bone to vibrations as one that yields positive results for decreasing the risk of fracture and maintaining the bone's integrity.

This is promising information as there is now information supporting that vibration therapy can have positive effects bone health across species as well. However, there are still some crucial gaps in knowledge not addressed in these experiments. The increased osteogenic activity was not correlated with any other biological factors such as

an increase in VEGF or vascularization. Both of these could lead to osteogenic activity by increase the activity of osteoblasts. If more connections can be made, then we will have a better understanding of how these diseases are affecting biological function.

This points towards a model for not only the elderly but also athletes and the younger population in general. If athletes want to maximize strength, they should not only focus on increasing the weight in routine workouts and exercise, but include meaningful rest periods for bone rejuvenation, and subject themselves to unique and varying load cycling. This will elicit bone mechanoreceptors and stimulate bone growth in areas normally neglected in their traditional regimens. Coupled with medical imaging, high-risk areas for bone fractures could be detected in individuals and then targeted with vibration therapy to reduce the chances of developing osteoporosis or a stress fracture.

2.4.4. Mechanically Induced Angiogenic Manipulation

In an animal model testing the osteogenic capability of bones of rats, results show that while not only baseline bone quality affects the osteogenic process, so does loading duration. This study showed that lower density rat tibias were more responsive to physical loading in terms of bone growth. The study also showed that there is an optimal range for how long to keep the tibias in loading to generate maximum bone growth. While this does corroborate some of the findings found in exercise science in human models, the experiment could be expanded upon more. The findings suggest that mechanical loading will produce greater effects in treating osteoporosis in lower quality bones than in higher quality bones. This experiment did not consider that higher quality bone could produce the same results if different, heavier loadings were applied. Their

results were at a constant load, and we have already seen in human models that evoking the osteogenic response is unique in each bone (Ko et al., 2012).

A study that incorporated mechanical stimuli but instead looked at the blood flow to the bone was done by Muir et al. (Muir et al., 2007)**.** Fatigue loading was found to increase bone blood flow but decrease interstitial fluid. Since bone formation was observed, it is reasonable to theorize that bone formation is more dependent on bone blood flow, but not directly dependent on interstitial fluid. This corresponds with the idea that osteoblast activity is increased with blood flow as well (Marenzana & Arnett, 2013)**.** **T**his further highlights the need for collaboration between engineering and biological standpoints. Even though the end result of osteogenic activity occurred, it would serve to strengthen the results if we could link it to another measurement such as blood flow.

It has already been shown that exercise can be proven to be osteogenic in some populations in individuals, but can mechanical loading be utilized further to promote anabolic as well as angiogenic activity? Mechanotransduction plays a great part in the process of bone remodeling, and while it has yet to be fully understood in bone, its general principles have been applied to experiments for remodeling.

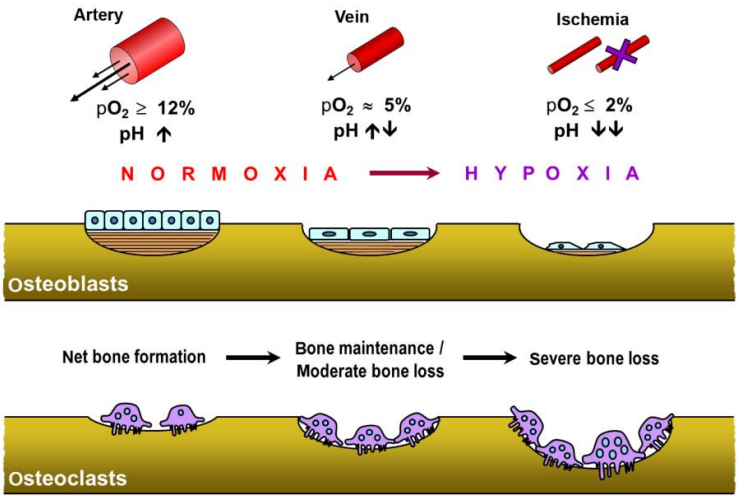

Figure 1.12. A schematic showing the relationship between hypoxia and osteoblast and osteoclast function (Marenzana & Arnett, 2013).

Angiogenesis and vascular remodeling are a critical part of any bone healing process, but a common obstacle that tissue engineered bone replacements encounter is inducing this formation process. In a study to look at the mechanical effects of vascular remodeling in tissue engineered bone, Boerckel, looked at the differences in immediate loading versus delayed loading for tissue regeneration **(**Boerckel et al., 2011). The group that received immediate loading experienced an inhibition of vasculature invasion into the new tissue and a decrease in bone formation. In the delayed group, a very different outcome was observed. Both vascular invasion and bone formation increased. It is important to note that the vascular invasion came from vascular remodeling as opposed to angiogenesis. This is still important because it highlights bone's aptitude for remodeling even if new blood vessels could not be formed. These findings suggest that bone healing can be improved or regulated through the timing of biomechanical loading. The early onset showed to create a larger stain on the bone, inducing a greater percentage of tissue differentiation into fibrous, avascular tissue and more scarring. These avascular regions

then posed to cut off nutrients to distal ends of the biomechanical loading, inducing an upregulation of bone volume proximal to the loading, making those distal ends prone to fracture. It is important to understand these vascular tendencies as the presence of blood vessels is directly related to bone health. If we cannot create healthy bone tissue then the risk of fracture is not reduced, and the loading received by the bone could still cause it to break.

The mechanical loading was shown to induce larger vessel diameters of the invading vessels and a corresponding increase in bone formation. While this study does bring to light notable knowledge on the timing of mechanical loading to bone healing, it could have been taken a step further by integrating this engineering approach with a molecular biology approach. It is known that cell signals such as VEGF and RUNX2 are present and elevated in cases where angiogenesis and osteoblast activity occur, respectively **(**Langdahl et al., 2016 & Shibuya, 2011**)**. A look at the spatial distribution of these factors in the engineered tissue and compare that to the native bone could have provided even more findings. The penetration of these factors or lack thereof could explain why there was decreased vasculature and bone formation in the early loading model and the opposite in the delayed loading model. This could offer some information as to what cell signals are specifically released during mechanotransduction in the bone. From here, from a clinical perspective, a better way to treat bone pathology using engineering aspects to induce cell signaling could potentially be researched further.

Another study by Boerckel showed another aspect of mechanotransduction (Boerckel, 2009). Rather than looking at the timing of a mechanical stimulus, this study analyzed the orientation of a mechanical stimulus to look at effects on engineered tissues

that replaced a substantial bone volume. Multiaxial and uniaxial loading plates were implanted into rat femurs. The uniaxial loads showed an increase in bone volume and stable implant tissue. The uniaxial model also showed an increase in torsional strength and stiffness. The multiaxial plate did not show sufficient stabilization of fracture propagation and bone integrity (Boerckel et al., 2009). This shows some relation to bone's anisotropic properties. Most bones are made to grow to sustain loading in a certain orientation. If the bone does not receive the loading in that certain direction and in other direction that, is it not accustomed to; there is a chance that the bone does not fortify to its normal yield strength.

While this paper holds valuable engineering information, it again stops short of relating it to a biologist standpoint. Mechanical properties of bones were determined and a significant difference in the different types of loading was found, but a deeper investigation into why this happened was not clearly stated. Anabolic results were shown by the increase in bone volume, but this could have happened from either the stimulation of osteoblasts cells or the inhibition of osteoclast cells. Similarly, it was stated that vascular invasion was necessary for maintaining the healthy engineered tissue, but this parameter was left out of the analysis. If a mechanical significance is determined, then by understanding the biological factors that contributed to this increase could help improve the model for rehabilitation after a significant bone loss or to improve regaining strength and stiffness. This shows the need for increased cross-disciplinary collaborations as more and more health concerns can be further explained if the expertise from multiple fields of study is used for analysis.

2.5. Identifying the Knowledge Gap

2.5.1. The Link Between Biomechanics and Physiology

As stated above, there have been numerous cases to show that inducing mechanical forces onto a bone can alter its physiology, which can lead to pathology or fracture. In most cases, the mechanical stimuli are directly related to the resultant pathological state of bone gain or bone loss. From the development of the physiological processes of bone earlier in this chapter, we can see that bone has a plethora of ways to remodel and sustain itself. The remodeling process not only relies on the osteoclast and osteoblasts stimulation, but it has multiple inputs from the endocrine system in the forms of estrogen, PTH, vitamin D, and IGF-1 that aid in the deposition and storage of calcium in the bones. The vascularization that helps in healing microdamage can be attributed to VEGF, HIF-1, or even foreign tumors. The point is that bone physiology is so intertwined with the rest of the workings of the body that there may not be only one answer to help mitigate bone loss or microdamage. This shows that while the first direct approach may not work, other avenues need to be researched that may be unconventional at first but may shed some light on the curtailing of bone disease.

Now that the relevance of vasculature and bone remodeling has been highlighted to show the numerous ways in which bone activity can be stimulated, it is time to take a look at the tools we have to analyze parameters to yield a representation of bone integrity. If the bone can be effectively analyzed, then this provides a better description of the remodeling and angiogenic nature of what is happening inside the bone. Loss of bone density could be a result of decreased osteoblast activity or increased osteoclast activity and necrosis could be the result of decreased angiogenesis, all of which have biomarkers

and gene expression that have been described above. The issue is, it is hard to evaluate some of these parameters noninvasively, and the once thought of golden standards for evaluating bone are showing less and less promise as the research field advances. Some metrics directly correlate with bone's mechanical properties, but now evidence shows that some variables are misrepresenting this information. There may need to be a shift in what is defined as a parameter for indicating bone health. Instead of focusing on the bone itself, there may need to be another look at the vasculature within the bone, since that is the portal for vital nutrients to enter the bone. Regardless, the gap remains between the problem and the solution.

2.5.2. Limitations in Evaluation Methods

2.5.2.1. Densitometric Measures

With the main demographic of the United States aging, research on bone health and risk assessment has become more important than ever. Fractures compromise the bone's ability to bear loading and be utilized by the body locomotion and other tasks. In older populations, fractures can lead to further complications that can even result in death. Identifying risk factors and developing methodologies to diagnosis disease onset is becoming more crucial more than ever.

A common densitometric measure used to assess the quality of bone is bone mineral density (BMD). BMD refers to the measure of bone mass per volume, but while this is a current measurement, there has been some controversy surrounding its efficacy (Bolotin, 2007). While there is a direct correlation between decreasing BMD and increasing the risk of fracture, this relationship only works one way. Increasing the BMD

of bone does not seem to decrease the risk of fracture, but decreasing the BMD increases the risk for fracture (Heaney, 2003). This an extremely important notion to observe, especially in disease states that decrease BMD. Even if bone loss is stopped over even reversed, the integrity of bone might be permanently lost (Dominguez and Agnew, 2019). Osteoporosis is the most common metabolic bone disease state, resulting in the majority of fractures of postmenopausal women and the elderly. The most common drug to treat osteoporosis is a bisphosphonate, which works to stop bone loss. Contributing to the skepticism of the efficacy of BMD, studies have shown that while bisphosphates slow and prevent bone loss, they may not contribute to the reduction of risk of fracture (Dominguez and Agnew, 2019). This highlights the importance for further research as current methodologies for combating these diseases are being shown to be ineffective.

Realizing this lack in detection possibility, a new method named Fracture Risk Assessment Tool (FRAX) has been utilized by healthcare providers to try to depict bone health and predict fractures chances more accurately (Unnanunntana et al., 2010). This protocol released by the Who Health Organization in 2008 inputs age, sex, race, height, weight, body mass index, history of fragility fracture, parental history of hip fracture, use of oral glucocorticoids, rheumatoid arthritis, smoking, and alcohol consumption into an algorithm to output a ten-year probability of a major osteoporotic fracture in the proximal humerus, wrist, hip, and vertebrae. While this yields a more accurate prediction of fracture, there is still room for improvement. Combining potential biomarkers with imaging technology could yield the best possible predictor.

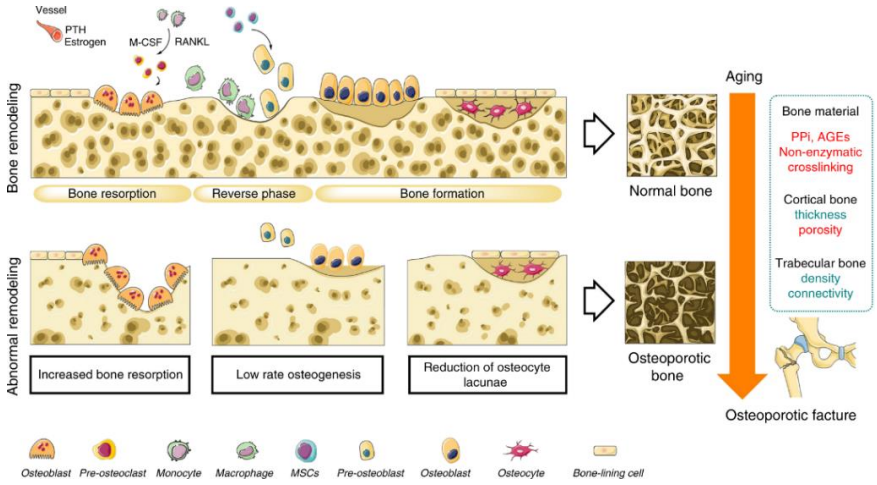

Figure 1.13 The differences in densities in the remodleing process and the composition of a healthy bone (top) and an osteoporotic bone (bottom) (Xie et al., 2019).

2.5.2.2. Finite Element Analysis (FEA)

Engineering models have developed significantly over the years, showing accurate representations of how a structure will react in a given situation. One specific model analysis type that is showing favorable diagnostics of bone pathology is finite element analysis (FEA). FEA is a digital model method that predicts the reaction for a certain body when exposed to real-world scenarios of vibration, heat, fluidics, or other physical effects. Finite element analysis can show localized areas of stress and wear and predict where it will break first. They allow for the generation of models that may not be able to be recreated experimentally and allow for unique attributes to be applied to each element rather than applying the same properties to the entire structure (Panagiotopoulou, 2009).

Bone could benefit from this because of its inhomogeneity in properties between trabecular and cortical portions. Bone, as stated earlier, is an anisotropic material that

proves hard to recreate in finite element (FE) models but is still more accurate than assuming it to be isotropic. The same goes for bone's viscoelastic properties. These are hard to truly capture within the model, but they still provide more assurance to the validity of the model than to assume linear elastic properties (Burr, 2016)**.** This is extremely helpful in the field of bone pathology as one of the main implications is bone fractures which can have serious detrimental effects.

Zysset et al (2013) performed an experiment using clinical computer tomography scans in a finite element model to test the current densitometric standards of bone mineral density (BMD), bone mineral content, and areal BMD (aBMD). These current standards can be used to predict the strength of a given bone. Zysset showed that in three different fracture sites, the distal radii, the spinal vertebrae, and the proximal femur, the FE model using the clinical scans was more reliable in predicting the nature of the bone strength than the densitometric predictors (Zysset et al., 2013). This experiment along with many others shows that technology is further advancing to create these detailed FE models to recreate many other experiments in order to charactierize the complexities of bone properties. Figure 9 shows a derived FE model of the humen femur (Eberle et al., 2013). This further emphasizes the fact that current methods are becoming increasingly outdated and the need for further research is more present than ever.

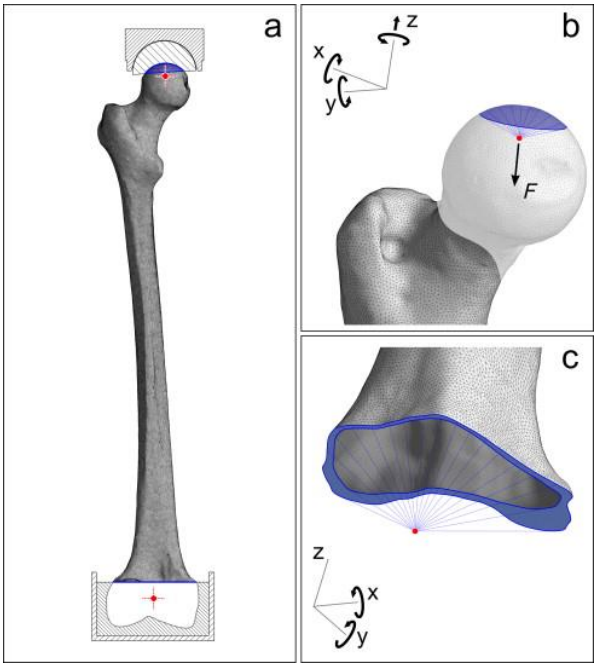

Figure 1.14 FE model of a human femur bone with the center of rotation of the femoral head and cardanic center marked (a). The boundary conditions and load applications on the femoral head (b). Boundary conditions of the distal end of the femur (c) (Eberle et al., 2013).

2.5.2.3. Implications and Unmet Needs

A common theme observed throughout the entirety of this paper is not only the fact that there is still a knowledge gap between the physiological processes of bone remodeling and external mechanical stimuli but the call to action to further the research of this field to shorten that gap. The bone remodeling process has been identified, cell signaling pathways differentiated, and growth factors named, but there has been a disconnect on how external stimuli are translated into the end phenomenon that is bone absorption or bone growth. We have observed that stimuli such as exercise, vibration, mechanical loading can all change the physiologic state of bone, but it is more of a black box flowchart. Stimuli go in and bone remodeling comes out. Theoretically speaking, from the different pathways that have been identified, there could be more than one

pathway that has the potential to be activated to get the same result. There needs to be a cross-discipline approach to analyzing this problem in two stages. The first is to not only relate mechanical stimuli to the loss of bone biomechanics but also understand what physiological processes are happening inside the bone. The next is developing imaging modalities that can image and detect these physiological processes and predict the effect on bone integrity. Developing this has the inherent possibility to transform healthcare, but the effects of improving bone health for longer can resonate in more aspects of our society.

2.6. Conclusion

Bone is a very complicated and changing material. The need to further understand it as a living material is as pressing as ever. Its heterogeneous makeup explains its viscoelastic and anisotropic properties and holds valuable information in loading failure. Because of these time-dependent and nonuniform properties, the ease of integrating other materials and devices to help the bone heal is complicated. There is not a full-proof method for total knee arthroplasties or total hip arthroplasty that reduces implantation site morbidity and stress shielding to zero. With the aging population, the ability to understand and develop the properties of bone is crucial.

Bone's remodeling properties are affected by many different signaling pathways, which could be utilized to our advantage if stimulated properly. We also know that bone cannot only remodel its matrix and collagen orientation, but also the vascular networks within it as well. By analyzing these pathways, we can then identify the best way to stimulate osteogenic and angiogenic activity whether that be through mechanical loading

or induced cell signaling or other means. Bone has been shown to respond in a variety of ways to different stimuli, showcasing the fact that we could stimulate the bone to fix or change itself in almost any situation.

To effectively utilize the information that bone holds for us, we need to develop better, more precise, imaging techniques for in vivo studies. Older metrics, such as only looking at densitometric values such as BMD, which were once used in evaluating the integrity of bone are now proving to be outdated. While higher quality imaging techniques are showing an advanced stage of metric analysis, not all can be performed directly on the bone in vivo. These imaging techniques need to be modified to be able to be used on a living specimen or coordinate them with imaging modalities that can, to cross-reference parameters with a high enough level of precision. Having better metrics for real-time analyses could be the difference between preventing catastrophic failure of bone.

The experiment detailed in the following chapters seek to establish the first step in moving towards these more precise studies. The goal of this study was to develop a new Fast Fourier Transform based methodology to analyze the rapidly changing internal structural differences in the equine PSB in order to compare the differences in horses that sustained a fatal fracture and horses that did not. The process will seek to provide quantitative measurements useful for analyzing how the bone grows and how the internal pore structure remodels in response to the mechanical loading. The information will ideally be translated into prophylactic training measures when the horse is still alive in hopes of mitigating the damage done to the horses from these fractures or preventing the fractures in their entirety. With these fractures happening in different locations within the

bone and propagating in different directions, it is reasonable to assume that there could be a regional anomaly that induces these fractures within the bone. By comparing different spatial areas within the bone, there is a possibility to find the commonality in the regions that experienced a fracture and develop characteristics to identify these conditions for detecting these fractures before they happen. This would then provide a link between the variation in the porous structure and the mechanically induced failure modalities. Through the use of Fast Fourier Transforms (FFT) and statistical models can be quantified and analyzed for significant differences in each specific spatial region that is analyzed. From here, ways to improve race training and the amount of stress sustained by the fetlock can be imposed to help increase the health of the PSB and of the racehorse as a whole.

CHAPTER 3. μCT SCANNING AND IMAGE ACQUISITION METHODOLOGY

3.1. Study Population

The population of racehorses used in this study were Thoroughbreds ages 2-6 years old including both genders and both castrated and uncastrated males. The horses are divided into 4 experimental groups for testing: 1) horses that were actively race training and sustained a CMI that did not include a PSB fracture, 2) horses that were race training and were euthanized due to a non-skeletal health issue, 3) horses that were race training and sustained a CMI that did include a PSB fracture, and 4) horses that had not entered into race training, serving as the control. All 4 PSBs were obtained from groups 1, 2, and 4. For the fracture group (group 3), only the two intact bones on the contralateral limb of the fracture were obtained.

Experimental Group	CMI only	Non-CMI	CMI & PSB	Control
Number of Horses	10	10	20	4
Number of Bones	40	40	40	16
Age Range (yrs.)	2-5	2-6	2-6	2-5
Gender Breakdown	4 Female 5 Uncast. Male 1 Cast. Male	4 Female 3 Uncast. Male 3 Cast. Male	8 Female 6 Uncast. Male 6 Cast. Male	4 Female 1 Uncast. Male 0 Cast. Male

Table 3.1 A signalment breakdown of the experimental groups showing the number of horses, the number of bones, the age range, and the gender distribution for each group.

3.2. Sample Collection Procedure

The horse specimens were obtained by the University of Kentucky Veterinary Diagnostic Laboratory (UKVDL). The UKVDL is a part of the Kentucky Horse Racing Necropsy program, which allowed the horses to be transported to the UKVDL for a full postmortem examination. All horses were euthanized on site of one of the five racetracks or two training centers in Kentucky due to injury or training or other medical reason. The PSBs were then extracted from the horses at the UKVDL.

3.3. µCT Scanning

The dissected proximal sesamoid bones were taken from their formalin storage containers and dried thoroughly using paper towels. The bones were then secured, using Styrofoam packing if needed, inside a Scanco Medical scanning tube so as to make sure

the bones did not move during the scanning process. A PSB secured in the scanning tube is shown in Figure 3.1.

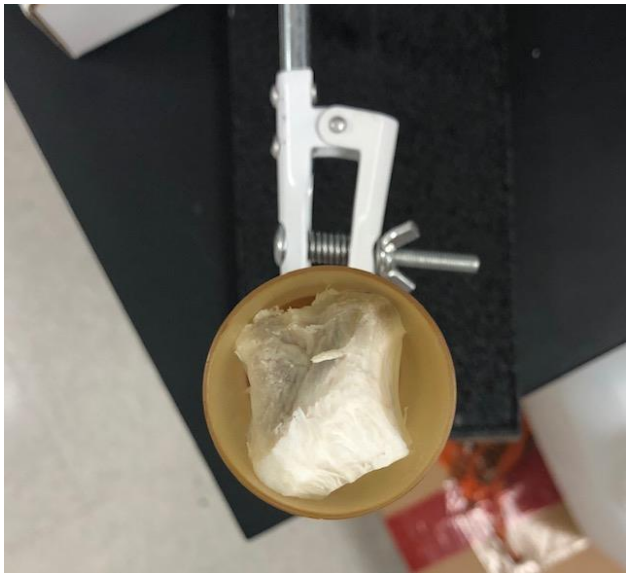

Figure 3.1 A picture showing the equine PSB secured in the microCT scanning tube.

The bones inside the tubes were then scanned using a Scanco Medical µCT 40 scanner (software version 6.1, SCANCO, Wangen-Brüttisellen, Switzerland) at energy intensity settings: 70kVp, 114 microamps, and 8W and standard resolution**.** Once the scan was complete, the entirety of the scan was processed using a preset script on the microCT machine to convert the images to DICOM images. The DICOM images were then downloaded onto a PC desktop computer from the microCT machine using the app, MicroCT FTP (software version 3.7, SCANCO, Wangen-Brüttisellen, Switzerland**).**

3.4. SimpleWare Slice Generation

The DICOM set of a single bone was then uploaded to Simpleware (Scan IP P-2019.09, Synopsys). The entire image was then rotated so that the non-articulating peak of the bone was dissected by the sagittal view of the 3D modeling program. Figure 3.2

shows a transverse view of the orientation that all bones were rotated to, ensuring a more normalized slice set.

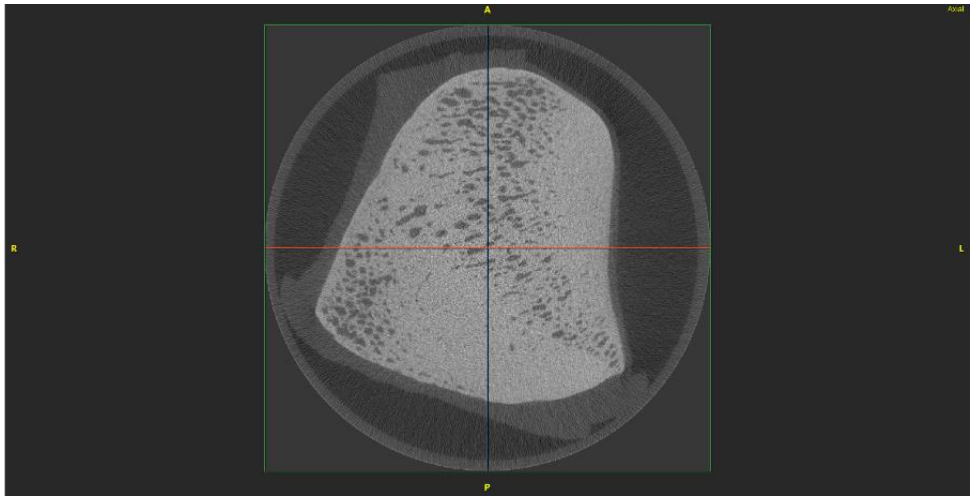

Figure 3.2 A screenshot from Simpleware showing the orientation to which all bones were aligned before the sagittal slices were obtained. The right side edge of the bone is the articulating surface and the left side edge is the non-articulating surface.

This was done for all bones to ensure that they all shared the same orientation. A sagittal bone mask was then created at the apex of the bone, which was labeled “Slice B.”. Another mask was created 100 pixels (~ 33mm) towards the midline of the leg in reference to Slice B and was labeled “Slice A.” A final mask was created 100 pixels (~33mm) away from the midline of the leg in reference to Slice B and was labeled “Slice C.”. These three (3) slices were chosen based on the objective of this study. This study wanted to look at the differences in apical, midbody, and basilar structures and these three masks contained regions that were fully formed. These three (3) masks were then exported as DICOM images from SimpleWare to the lab desktop using the SimpleWare application.

3.5. ImageJ Fast Fourier Transform (FFT) Methodology

3.5.1. Data Collection Procedure and Rationale

Once the DICOM images were created, they were imported into ImageJ v. 1.53j (National Institute of Health, Bethesda, Maryland, USA). Using ImageJ and a plugin, Easy PowerSpectrum v. 1.2.2. (Glunder, 2020), the Fast Fourier Transform (FFT) was taken at the apical, midbody, and basilar regions of the bones in the 3 DICOM images. Using the "Report Dominant Peaks" function of the plugin, the selection window for the FFT was fitted around the porous structures to isolate the porous network as the structure of interest rather than any compact bone around the edges of the bone (the analysis and rationale for this procedure is detailed in the following chapter).

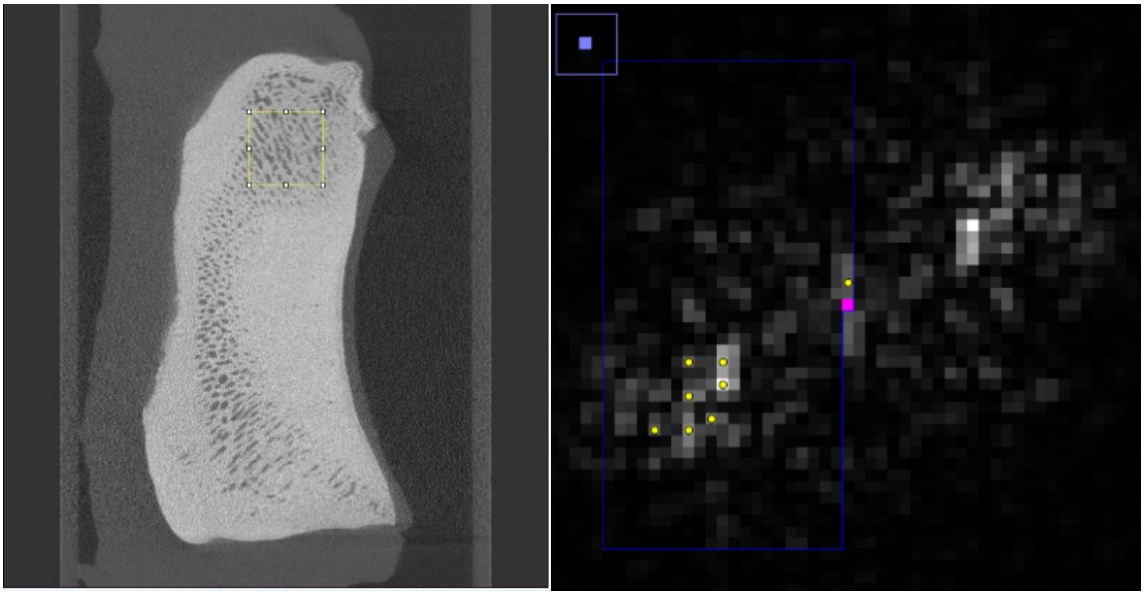

Figure 3.3 A PSB slice with the selection window for the apical region shown by the yellow box (left) and the corresponding Dominant Peak FFT spectral output (right). The varying grey square pixels in the image on the right desingate all of the frequencies detected by the FFT. The yellow dots on the image on the right designate the "peak frequnecies" as detected by the Easy Power Spectrum plugin.

There were three (3) different FFTs taken for each slice: 1 in the apical region, 1 in the midbody region, and 1 in the basilar region. A sample selection window of the apical region and its corresponding FFT output is shown in Figure 3.3. The selection windows were located in the internal region of the bone to capture the most repeatable capture of the porous structure. The articulating surface is comprised of compact cortical bone and the palmar surface of the bone presents the trabecular structure that are not in the same consistent pattern of that of the most internal region. Windows were placed along the same internal stress trajectories along the same bone to provide some commonality among the windows for each individual slice. The spectral peaks were then labeled through the report dominant peaks function, and those peaks were then isolated from the FFT and peaks with their coordinates were saved in a text file to be analyzed. There were other options as well in the plugin, but the “Report Dominant Peaks” function was determined to yield the best results for finding the peak frequencies. The selection process is detailed in the next chapter.

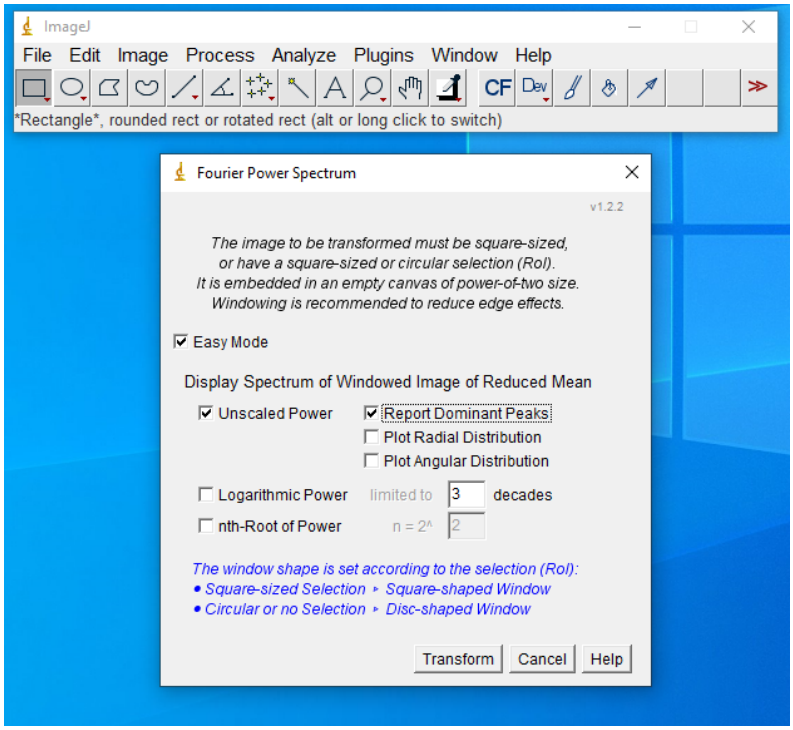

Figure 3.4 A screenshot showing the setup for taking the FFT in the EasyPower Spectrum plugin.

3.6. Confidence Ellipse Generation

After the text file with the spectral intensities was saved, it was then uploaded into Microsoft Excel where it was analyzed using the Xrealstats add-in v. 8.1.5. (Zaiontz, 2010). This add-in allows a confidence ellipse to be fitted onto a plot of points and calculate the length of the a-axis, b-axis, and the angle of rotation of the a-axis from the positive x-axis in the Cartesian coordinate system (The procedure on how to obtain these ellipses and how to convert them into spatial domain data is detailed in the following chapter). Each bone had a confidence ellipse generated in the apical, midbody, and basilar regions for all three (3) slices (slice A, slice B, and slice C), creating a total of nine (9) confidence ellipses for each bone. For each ellipse, the length of the major and

minor axis and the angle of rotation was recorded. Figure 3.4 shows a sample confidence ellipse for which the values were taken from for the apical region.

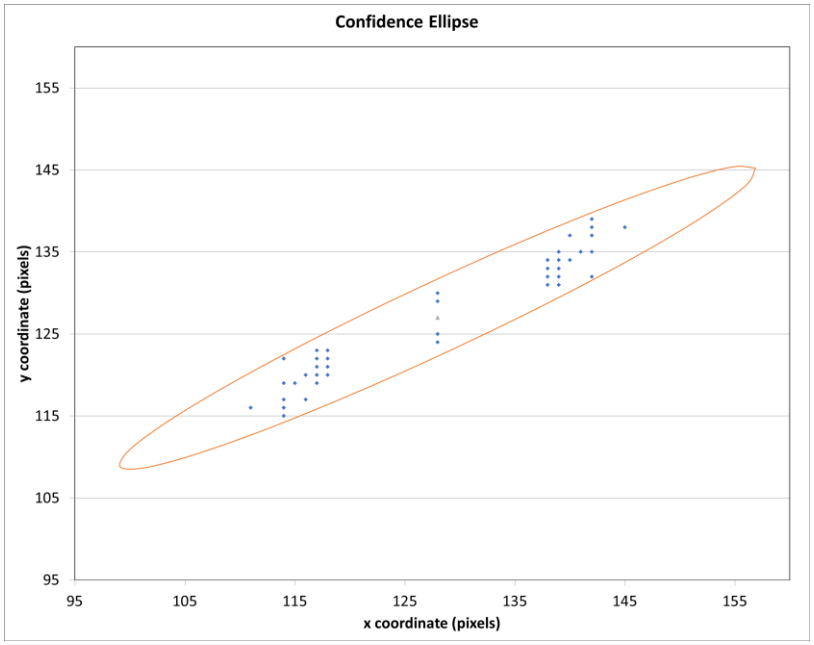

Figure 3.5 A sample confidence ellipse generated from the FFT output in the apical region.

CHAPTER 4. ANALYSIS OF PROCEDURES

4.1. Understanding the Imaging Processing FFT

Before we narrow in to analyze the obtained results, the analytical basis underlying the data generation and analysis of the FFT of the scanned images needs to be discussed in detail. It is known that Fourier Analysis is used to detect repeating patterns and relationships from images that may not be visible to the naked eye. These relationships are present in the frequency domain, which is made available to the user from the FFT technique. The need to better understand what the data in the frequency domain meant was addresses through a round of phantom testing before the data was contextually analyzed.

4.1.1. Phantom Creation

We begin by creating phantoms of basic patterns with varying pore sizing and pore spacing and apply FFT to them. Through this process, we will establish some basic rules for interpreting and analyzing results. First, a phantom of a grid of sixteen (16) equally sized squares was created to see if the FFT was more sensitive to detect the change in the size of the squares, the porosity, or the change in the distance between the centers of the squares, the periodicity. In some cases, the periodicity of the pores would remain constant while the size of the pore itself changed, or a vice versa case, the size of the pores would remain the same while the distance between them was manipulated. It is important to characterize the capacity in which the FFT is able to capture these changes to effectively analyze the data and make accurate conclusions. To characterize the FFT capability, a confidence ellipse was overlaid onto the dominant peaks of the FFT output. Since all phantoms were uniform, the confidence ellipse was a circle each time. The length of the

axis of this ellipse (equivalent to the radius of the circle), was then recorded and graphed. (In the context of the porous structure of the bone, the lattice is much less uniform and will result in an ellipse with a major and minor axis). The main analysis points of the graphs were to examine how the length of the ellipse changed in each instance to the specific dependent variable. The following testing will help determine what the length of the ellipses of the FFT help quantify in the phantom. Another parameter that will be used to help elucidate this relationship is the slope of the line of best fit. It is expected that an inversely linear relationship will present itself with graphing the length of the ellipse against a feature in the spatial domain. This is from the derived inverse relationship of the frequency and spatial domain found in literature. The graph with the greatest negative value (highest absolute value) will show the strongest inverse relationship. This value will also help differentiate whether the FFT is more prone to detect changes in the periodicity or porosity.

4.1.2. Periodicity Testing

For the periodicity testing, the original phantom was created and then the distance between neighboring pores was modified to create instances of increased or decreased periodicity. From here, the FFT was taken in each case and the confidence ellipse was generated. The lengths of the axes were then recorded and graphed as a function of the distance between the pores. Since the phantom in the spatial domain is a uniform pattern, all confidence ellipses were circles having equal major axis and minor axis length. Figure 4.1 shows a phantom where the distance from the center of each square to the next was 40 pixels. Figure 4.2 shows the same phantom, except this time with an increased spacing constant of 55 pixels from the center of one square to the next.

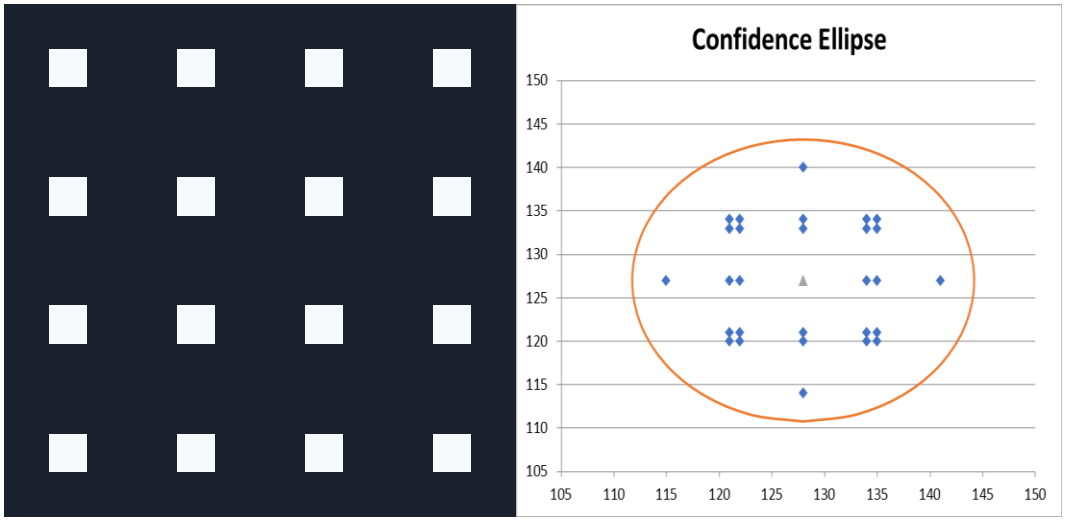

Figure 4.1 A phantom pore pattern where the size of the pores were held constant and the distance from one center to an adjacent center is 40 pixels (left) and the confidence ellipse of the domainant peaks of the FFT (right).

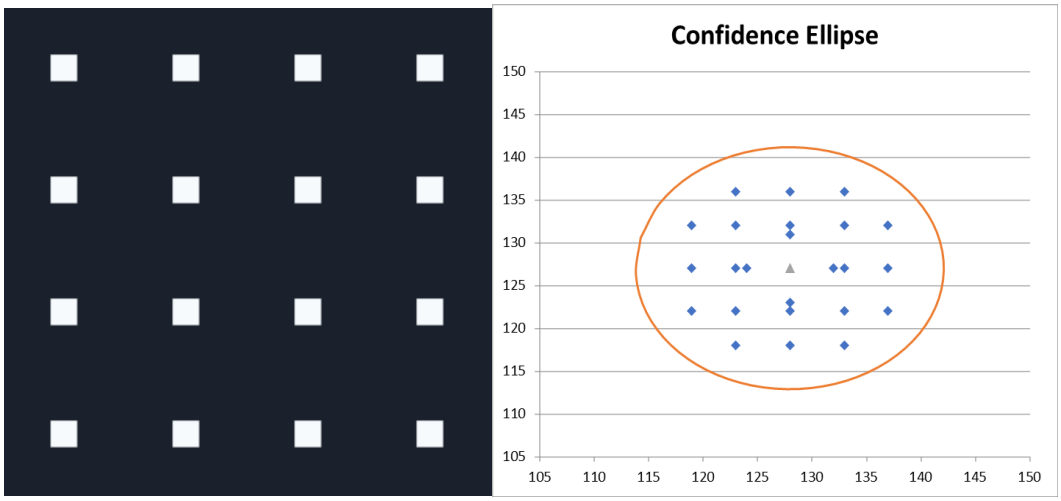

Figure 4.2 A phantom pore pattern where the size of the pores was held constant and the distance from one center to an adjacent center is 55 pixels (left) and the confidence ellipse of the domainant peaks of the FFT (right)..

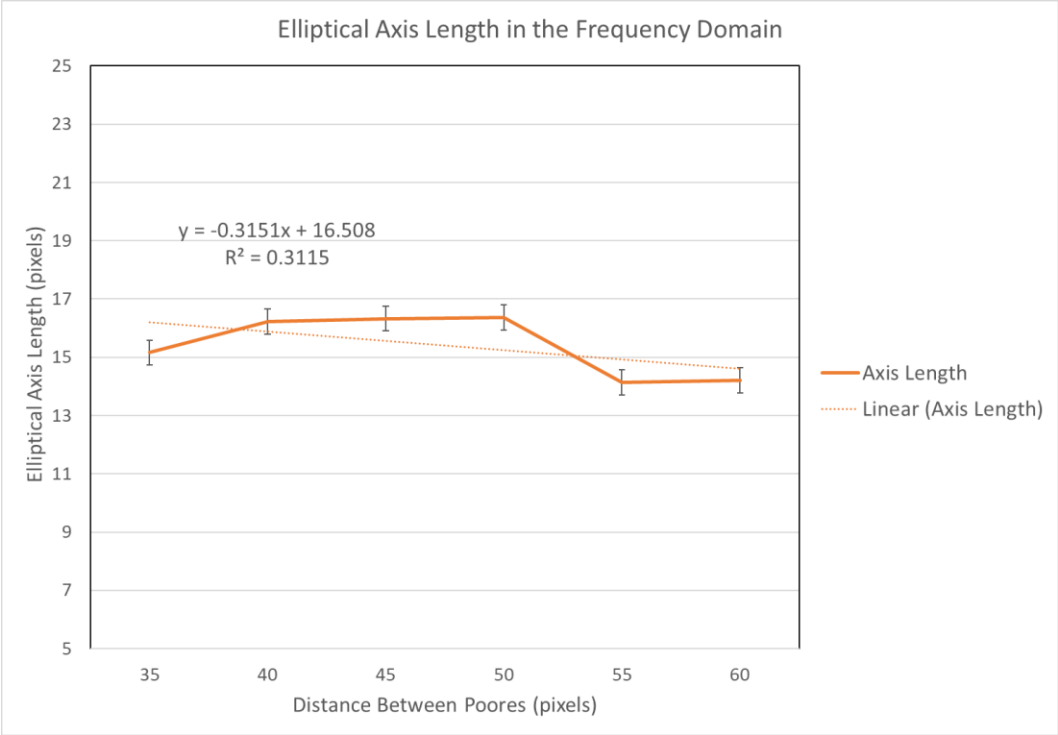

Figure 4.3 A graph showing the relationship between the length of the radius of the confidence ellipse in the frequency domain to changing the distance between neighboring pore structures in the different phatom models.

The graph shows that there is a slight overall inverse relationship between the distance between the pores and the ellipse axis, based on the slope of the line of best fit. However, the left side of the graph shows a linear relationship between the spacing the ellipse axis. A line of best fit was overlayed onto the graph, and the slope of the line and the correlation coefficient for the data is showed on the graph.

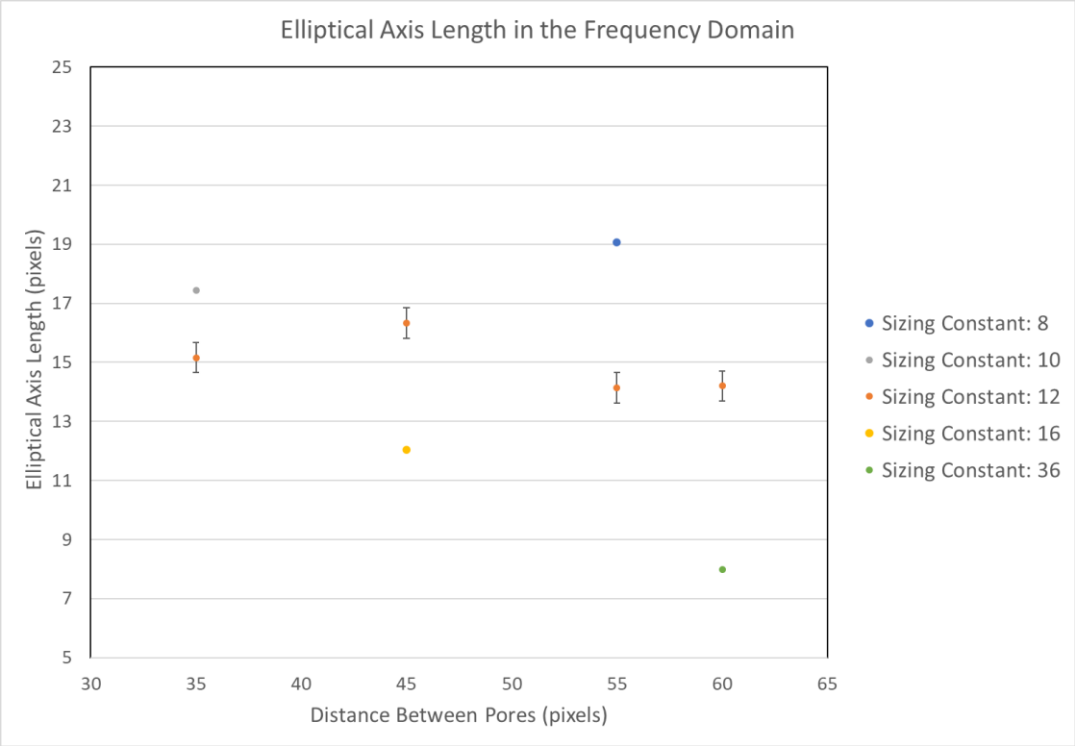

Figure 4.4 A graph showing the relationship between the length of the radius of the confidenc of the ellipse as a function of the distance bewtween the center of the pores. Different individual pore size constants are also testing and incorprated into this graph.

Further testing was done by changing the sizing constant, the length of the individual pores in the phantom, at different pore spacings. If the FFT was more sensitive in detecting the changes in the spacing, then changing the size of the pores in each test would not affect the elliptical output. As evident in the above figure, when changing the pore size, there was significant change in the ellipse. The inverse relation is shown when increasing the sizing constant, there is a decrease in the ellipse size and when decreasing the sizing constant, there is an increase in the ellipse size. This helps show that the FFT is detecting changes in the size of the pores.

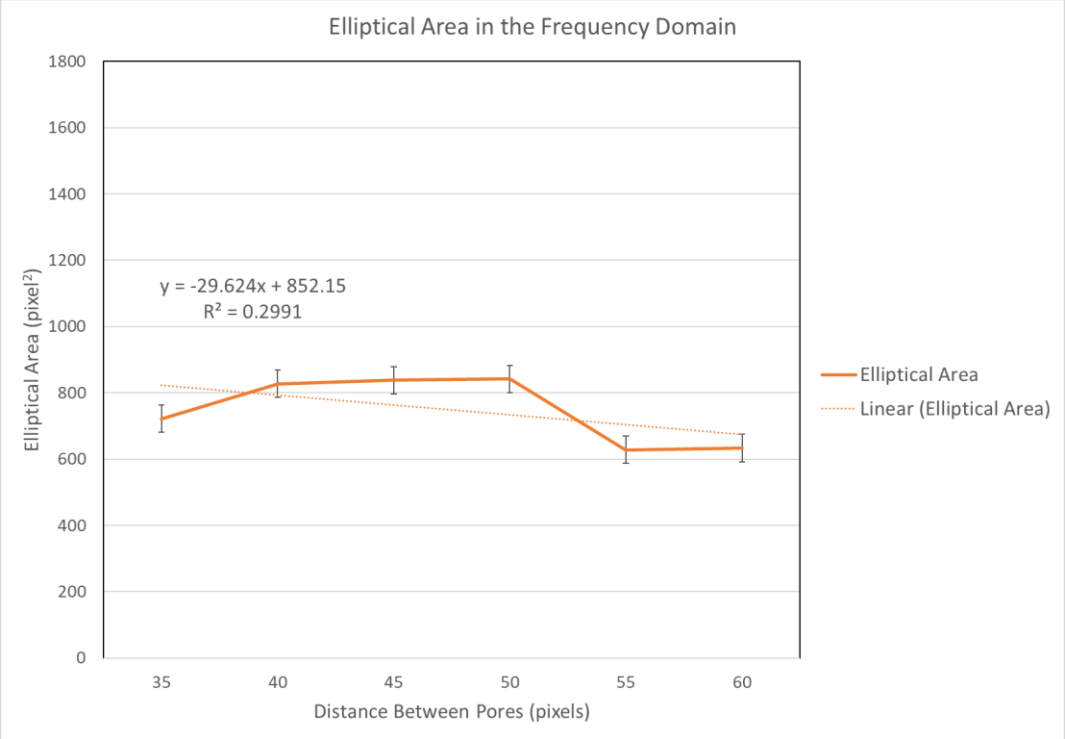

Figure 4.5 A graph showing the relationship between area of the confidence ellipse in the frequency domain to changing the distance between neighboring pore structures in the different phatom models.

This graph shows similar results to the previous graph of the elliptical axis length to the pore spacing. The same overall inverse relationship is present; but, again, the left half of the graph shows more of a linear relationship. A line of best fit was fitted to the graph, and the slope and correlation coefficient are shown on the graph. The low correlation coefficients indicate that these models might not represent the relationship of the data in the best way.

4.1.3. Porosity Testing

The porosity testing was accomplished by taking the original phantom and then changing the size of the pores within the phantom. This in theory would represent the change of porosity in a certain selection window because as the size of the pores increase,

the volume fraction of pores increases as well. The original phantom was then modified by increasing and decreasing the size of the pores still arranged in the 16-pore formation. The distance of the center of one pore to the next remained constant throughout the phantoms. The FFT was then taken of each phantom and the confidence ellipse were created. The distance of the major axis was then plotted as a function of the length of the pore. Figure 4.6 shows a phantom with smaller squares representing a bone with a smaller porosity. Figure 4.7 shows a phantom with larger squares representing a bone with a smaller porosity.

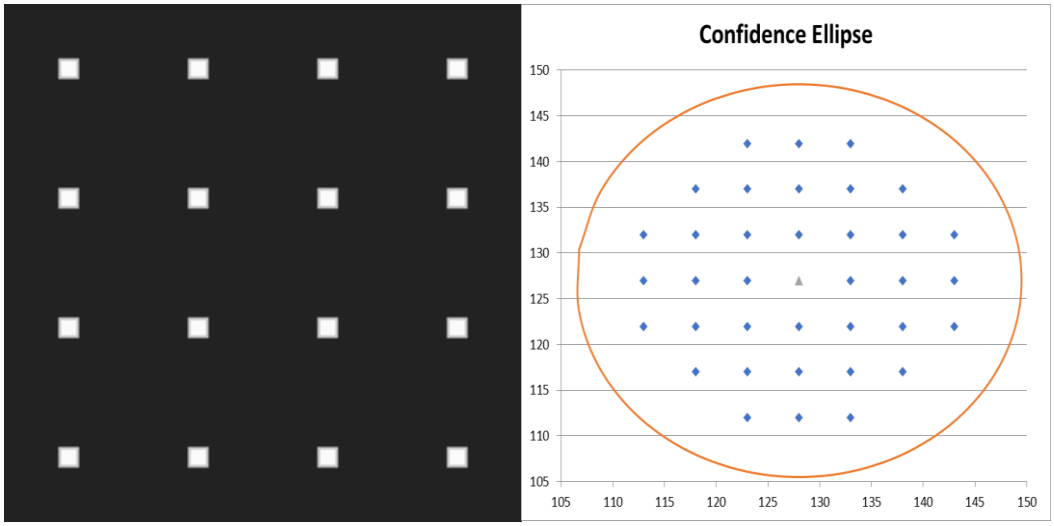

Figure 4.6 A phatom where the distance between the center of the pores was held constant and the length of each individual pore is 8 pixels long (left) and the confidence ellipse of the domainant peaks of the FFT (right)..

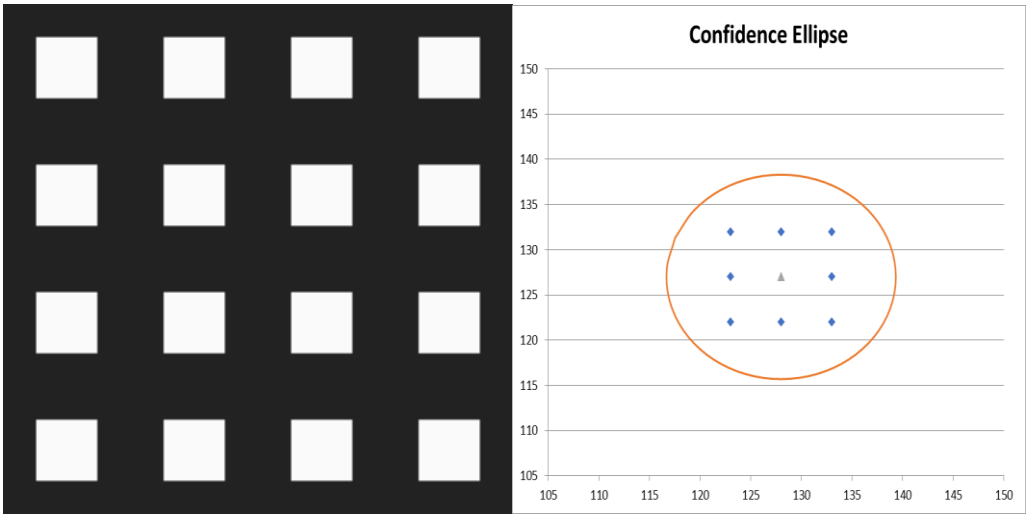

Figure 4.7 A phatom where the distance between the center of the pores was held constant and the length of each individual pore is 24 pixels long (left) and the confidence ellipse of the domainant peaks of the FFT (right)..

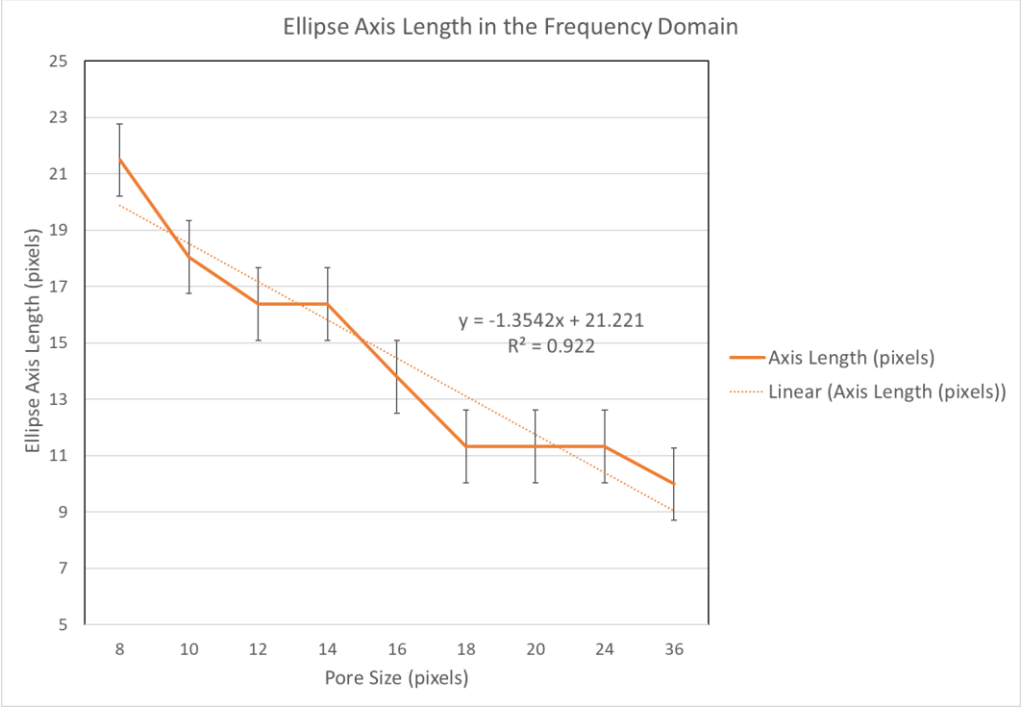

Figure 4.8 A graph showing the relationship between the length of the radius of the confidence ellipse in the frequency domain to changing the size of individual pore structures in the different phatom models.

The above graph shows the relationship between the pore size and the length of the confidence ellipse in the frequency domain. There is an apparent strong inverse correlation between these two parameters. As the size of the pore increases, the length of the axis of the ellipse decreases. This is the expected relationship from converting between the spatial domain to the frequency domain. A line of best fit was used to quantify the data. The slope of the line and the correlation coefficient are shown on the graph.

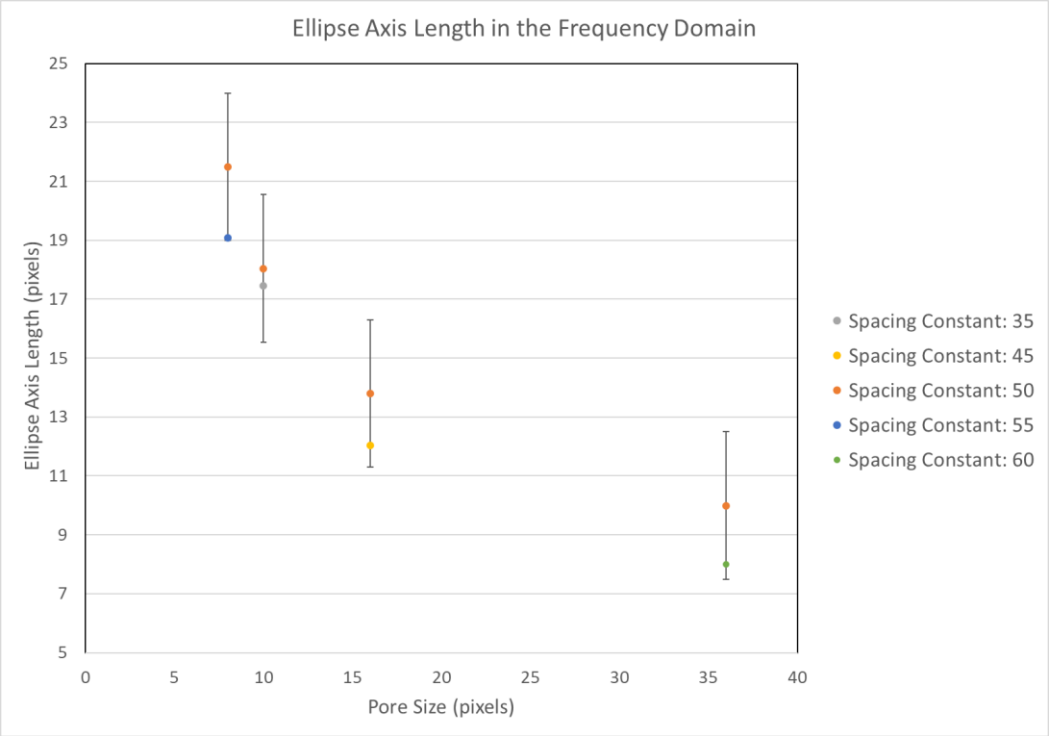

Figure 4.9 A graph showing the relationship between the length of the radius of the confidenc of the ellipse as a function of the size of the individual pores. Different individual pore spacing constants are also testing and incorprated into this graph.

Further phantoms were generated with pores of the same size, but the space between them, or the sizing constant, was altered to observe the effects in the ellipse in the FFT. From the graph, it is noticeable that the size did change, but there was no

distinguishable trend. Regardless of whether the sizing constant was increased or decreased, the size of the ellipse decreased. The overall trend of a decrease in the size of the ellipse as the size of the pores increased, was still able to be observed, however. This further reiterates that the changes observed in the size of the pores in a selection window of a given FFT dictate the size and shape of the spectral intensities of the FFT, rather than the distance between the pores in the selection window.

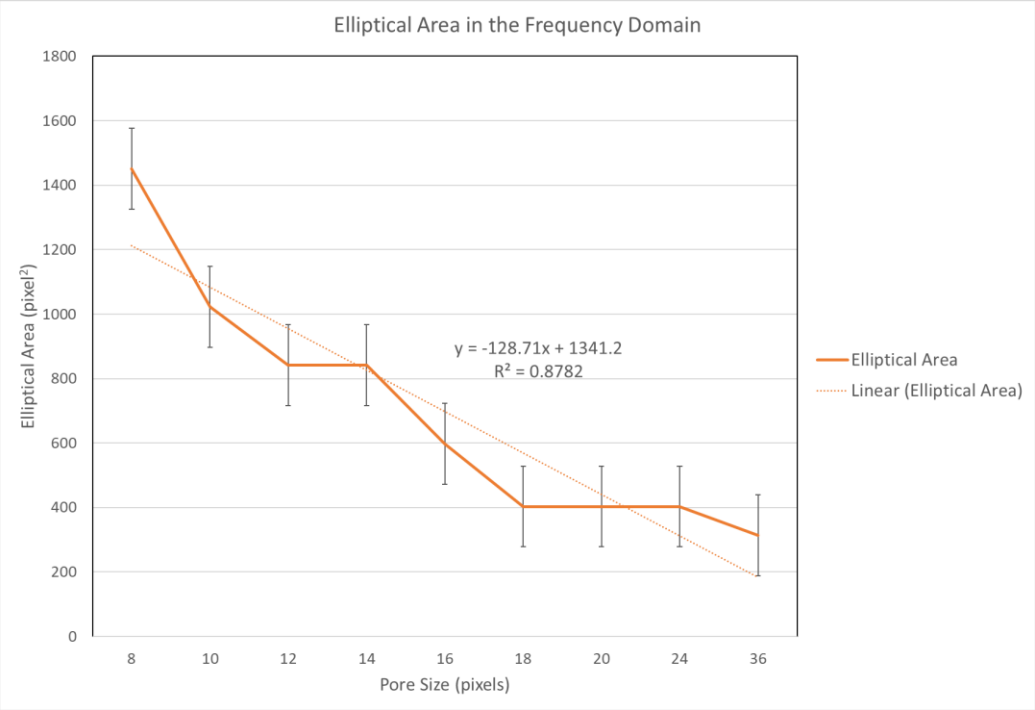

Figure 4.10 A graph showing the relationship between area of the confidence ellipse in the frequency domain to changing the size of individual pore structures in the different phatom models.

The graph above shows the relationship between the length of the pore in the phantom pattern and the corresponding area of the ellipse in the frequency domain. The same trends are apparent in this graph as in the graph relating the axis length of these same ellipses. There is an inverse relationship throughout the graph. As the length of the

pore increases, the area of the ellipse in the frequency domain decreases. The relationship is expected from known work on converting from the spatial domain to the frequency domain. Overall, the relationship between the length of the pore to the size characteristics of the ellipse in the frequency shows a stronger correlation and matches those relationships found in the literature. The slope of the line of best fit for the porosity test models are almost four times greater than the slope of the line of best fit in the periodicity testing. This along with the high R^2-values of the porosity testing indicate that the variability in the data is better explained by the porosity models. This means that the spectral intensities of the FFT better represent the repeating frequencies in the spatial domain that are represented by the length of the pores. Now that the relationship has been depicted, the procedure on how to analyze the frequency domain data will be detailed.

4.2. Frequency Domain Data

4.2.1. Data Analysis Using ImageJ

The outputs from FFT of the scanned images can be regarded as frequency domain spectral data. In using ImageJ, it is necessary to test the different display modes of the FFT to decide which mode would yield the spectral points that are relevant to our studies. The Easy PowerSpectrum plugin offered multiple reporting methods, but the ones that were decided to be of interest were the 1st log decade, the 2nd log decade, and the dominant peaks functions. The following section details the nature of each of these outputs and how a decision was made to conclude to use the dominant peaks methodology.

4.2.1.1. 1st Log Decade Power Spectrum

The 1st decade is logarithmically scaled. The 10log is taken of all the unscaled spectral intensities, and then they are mapped to 8bit integers on a scale of 0 to 255. A display of the first decade indicates that the smallest spectral intensity shown is 1/10 of the maximum spectral intensity of the transform.

It was shown that the peaks in the first decade did contain the spatial information we were looking for and the distribution of peaks was indicative of the pore shape, but it was hard to isolate those points from the rest of the FFT, and there was not a way to determine a consistent thresholding level to record the peaks.

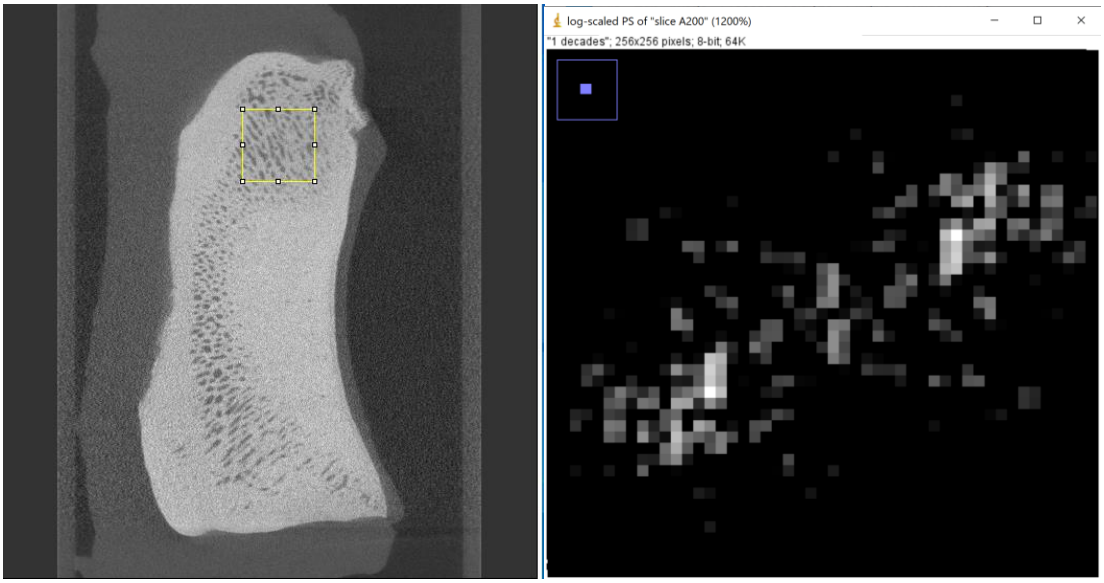

Figure 4.11 A sagittal slice of a PSB with the apical area of interest enclosed (left). The 1st log decacde FFT output (right).

4.2.1.2. 2nd Log Decade Power Spectrum

The 2nd decade is logarithmically scaled as well. A display of the second decade indicates that the smallest spectral intensity shown is 1/100 of the maximum spectral intensity of the transform. It was determined that the second decade contained too many

peaks in the frequency domain and the specific spatial information we were looking for, was harder to decipher from this output.

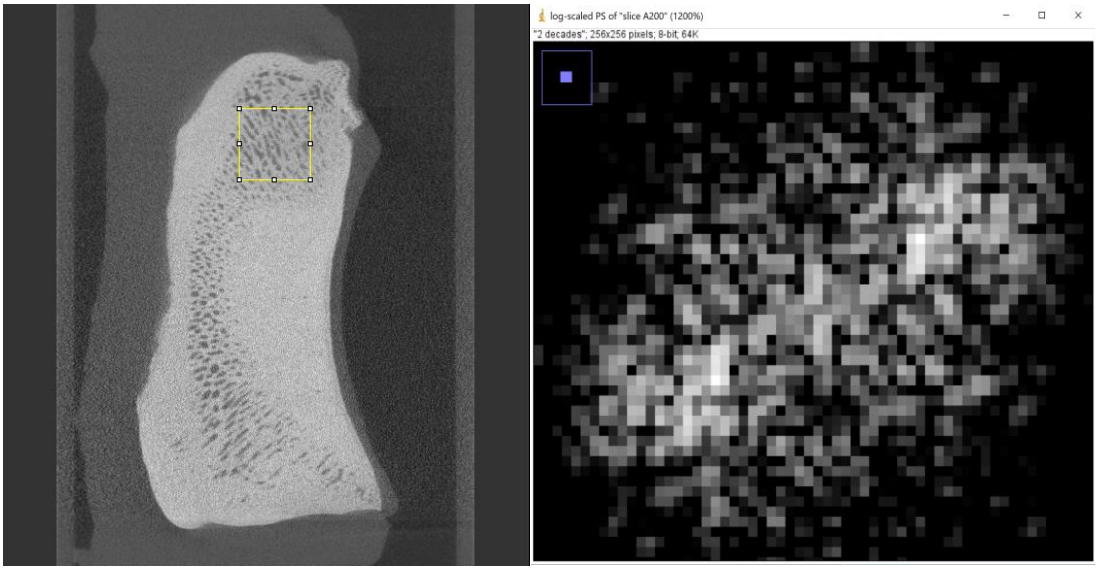

Figure 4.12 A sagittal slice of a PSB with the apical area of interest enclosed (left). The 2nd log decacde FFT output (right).

4.2.1.3. Report Dominant Peaks

The dominant peaks feature is based on the unscaled power spectrum of the transform. Up to twenty (20) spectral peaks in the upper 67% power range are detected with their absolute magnitude, relative magnitude, radial frequency, and spatial period calculated. This is extremely useful, because in a selection window of a repeating porous pattern, the dominant peaks should be the peaks associated with the pore shape of the repeating pattern.

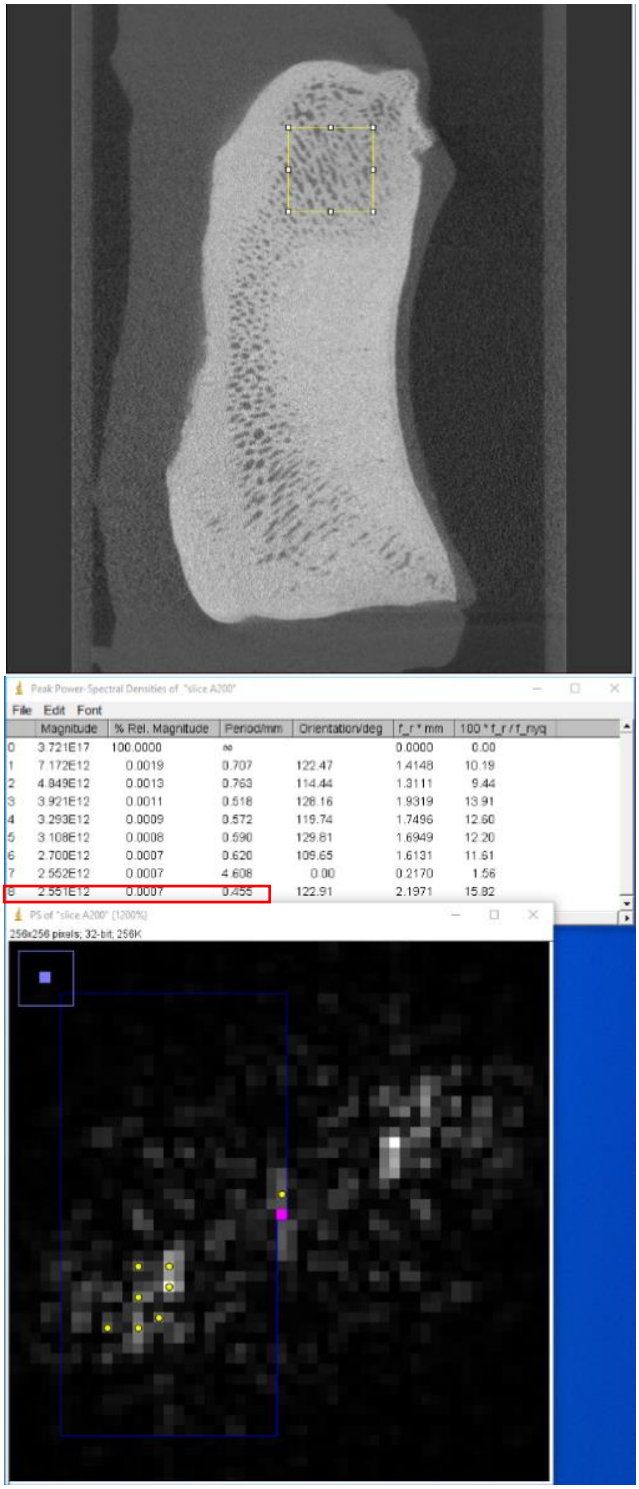

Figure 4.13 A sagittal slice and the apical region of interest (top). The dominant peaks FFT and spectral intensity output with the point of interest for calibration enclosed in red (bottom).

From here, a threshold level was set. The cutoff value would be the value of the smallest dominant peak, and all spectral peaks above this value would be recorded.

This ensures that all dominant peaks are captured along with all other high intensity peaks that might not be marked as dominant, but still have a high spectral intensity. These points on the FFTs, along with their spatial location on the FFT were then recorded and recorded as a text file.

Figure 4.14 A sagittal slice of a PSB and the apical region of interest (left). The dominant peaks FFT output, with threshold to isolate the points of highest intensity (middle). The threshold cutoff values to obtain the middle image (right).

However, the length of the center of one pore to the next (the periodicity) and the length of an individual pore are similar in size. If the FFT represents an average of the values in the selection window, there could be some confusion as to what the FFT is effectively capturing. To test the validity of this method, other theoretical testing needed to be done, which was accomplished through the phantom testing. Now that a valid

representation of the frequency data has been derived, the derivation into the spatial domain and those implications can now be detailed and presented.

4.3. Spatial Domain Relationships and Equations

The parameters of major and minor axis (a and b, respectively) are distances in the frequency domain measured in terms of pixels. The FFT output is a square box with the same number of pixels for the length and width, this pixel dimension of the whole FFT is determined based on the physical size of the selection window for the FFT in the spatial domain. Using the relationship shown in Equation 1, we can determine the length in the spatial domain from the frequency length of the confidence ellipse.

$$f_{max} = \frac{1}{2\ pixels} \tag{1}$$

If f_{max} denotes highest frequency possible, composed of alternating black and white pixels on every other pixel, this point will be represented by the furthest distance from the center on the FFT output. Taking another example of an alternating frequency of two (2) black pixels and two (2) white pixels, the repeating frequency is now a set of 4 total pixels. A relationship between the current frequency and the maximum frequency can now be derived, shown by Equation 2.

$$f = \frac{1}{4\ pixels} = \frac{f_{max}}{2} \tag{2}$$

Now, looking at the FFT output for a frequency of a pattern of four (4) pixels (alternating two (2) black and two (2) white), we can see peaks at halfway between the center and the edge.

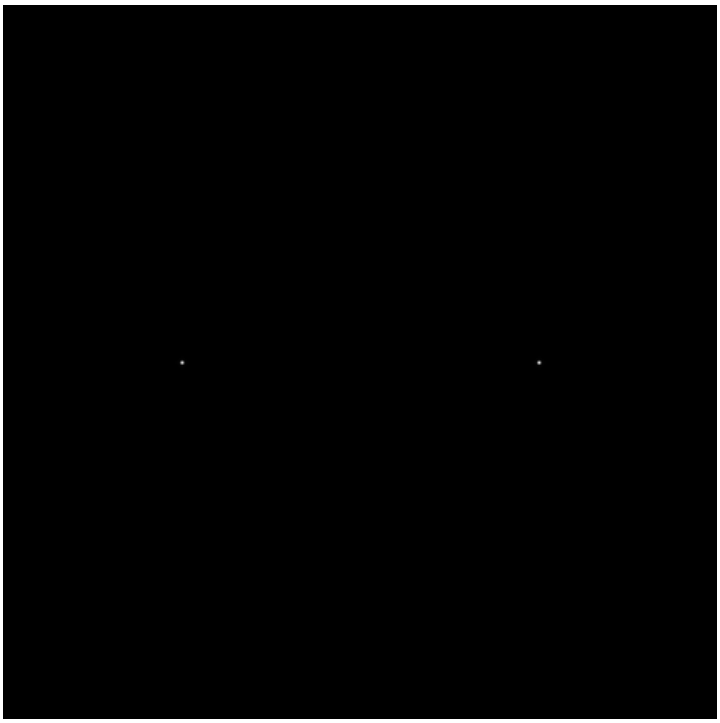

Figure 4.15 The FFT spectral intensity output of a phantom with a repeating of 4 pixels.

This sets up the inverse relationship between the frequency in the spatial domain and the distance of the peak from the center in the frequency domain. As the frequency increases in the spatial domain, the distance of the peaks from the center in the frequency domain decreases. To prove this equation for the current situation, we will take the point highlighted in Figure 3.6, and mark that point in our confidence ellipse.

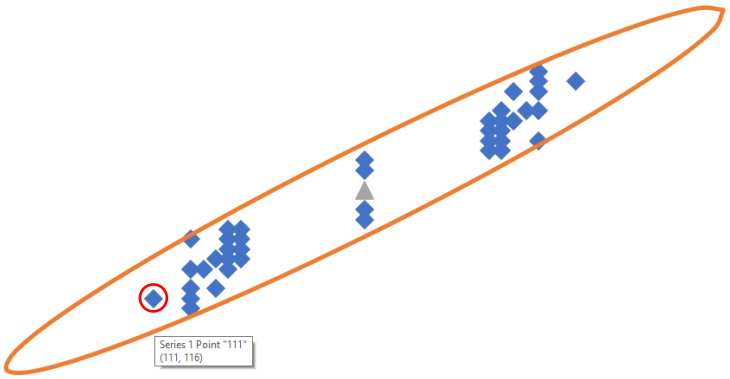

Figure 4.16 A confidence with a specific point highlighted that will be used to prove the relationship from converting to the spatial domain from the frequency domain.

The distance from this point (111, 116) to the center (128, 127) is ~20.248 pixels or $(410)^{1/2}$. Using the relationship from Equation 2, we can now use the following steps to calculate the associated spatial periodicity in terms of pixels (see Equation 3-Equation 9). Then, using the conversion factor of 36.86 millimeters to 1024 pixels obtained from the properties of the DICOM image, we can obtain the spatial periodicity in terms of millimeters in the spatial domain.

$$f = \frac{1\ cycle}{x\ pixels} \tag{3}$$

$$f == \frac{f_{max}}{\frac{x}{2}} = \frac{128}{\frac{x}{2}} = \sqrt{410} \tag{4}$$

$$x = \frac{2*128}{\sqrt{410}} = \sim 12.64294 \tag{5}$$

$$frequency = \frac{1\ cycle}{12.64294\ pixels} \tag{6}$$

$$period = \frac{12.64294\ pixels}{1\ cycle} \tag{7}$$

$$period = \frac{12.64294\ pixels}{1\ cycle} * \frac{36.86\ mm}{1024\ pixels} = \sim \frac{0.455mm}{1\ cycle} \quad (8)$$

The final calculation of the spatial periodicity is consistent with the calculated spatial periodicity from the Easy PowerSpectrum, proving that we can take a radial distance in the frequency domain and convert it to a spatial periodicity in the spatial domain. This is translatable to converting the radial distance of the major and minor axis of the confidence ellipse into spatial pore lengths in their respective direction. The angle of rotation must also be converted as well. Since this is an inverse relationship, the major axis in the frequency domain becomes the minor spatial periodicity in the spatial domain and vice versa for the minor axis. Our angle is now readjusted to correspond with the major spatial periodicity rather than the major axis of the ellipse.

4.4. Spatial Parameter Partitioning

Once everything is converted into the spatial domain, we now have multiple parameters to analyze among the different populations of racehorses. Using the major and minor axis, the area of the ellipse in the spatial domain can now be derived as well as creating a parameter for the ratio of the major axis to the minor axis. These parameters help characterize the size and shape of the pores in the spatial domain. After the data was compiled, a linear mixed model analysis, assuming compound symmetry, was used to evaluate the results using JMP statistical software. For the statistical analysis, the raw data in the frequency domain was used. More details on why this data was used is described in Chapter 6. Biologically impossible outliers were removed from the data set before a backwards elimination was performed on the model. Two different models were generated: the first model holds the elliptical area in the frequency domain as the

response variable and the second model holds the angle of rotation in the frequency domain as the response variable. Both models were run in all three (3) regions (apical, midbody, and basilar) for all three (3) slices (slice A, slice B, and slice C). The backwards elimination continued until the remaining fixed effect variables' p-value fell below the threshold of 0.05 or until there were no more variables in the model. In some cases, no variables were found to have a significant effect on the response variable. Interpretation for the meaning of the significance of the statistical models came from a series of tests using self-created phantoms to test the sensitivity of the FFT output.

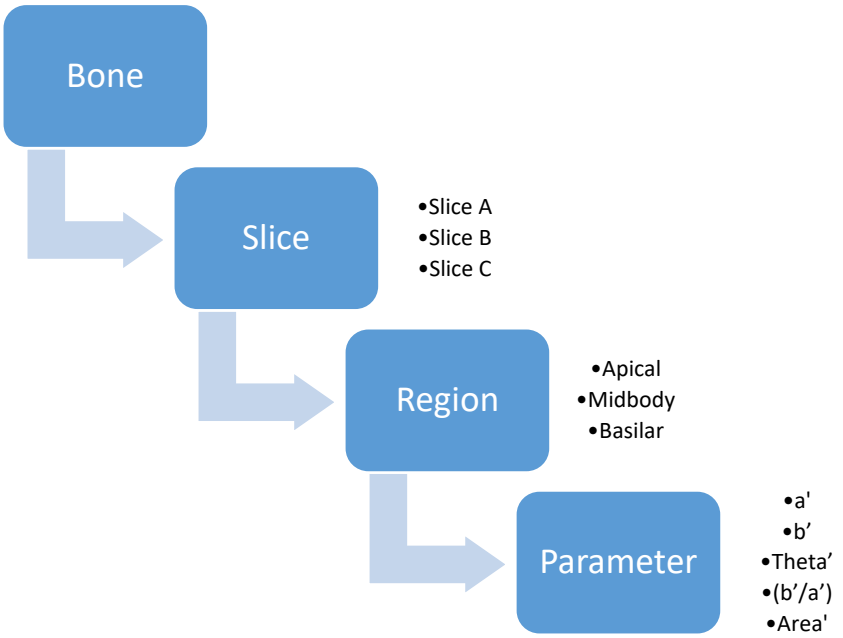

Figure 4.17 A flowchart showing how each parameter is obtained for each region and each slice of each bone. The parameters are as follows: a'- the average length of the minor axis of the pores in the spatiala domain, b' – the average length of the major axis of the pores in the spatial domain, theta' – the average angle of rotation of the pore in the spatial domain, b'/a' – the ratio of the average major axis length to the average minor axis length of the pore in the spatial domain, and area' – the average area of the pores in the spatial domain.

CHAPTER 5. RESULTS

5.1. Phantom Results and Implications for FFT Analysis

The data from the phantom testing is compiled in the following charts. Understanding this data before moving forward in other data analysis provides a clearer understanding on how the analysis of the FFT data can be practically analyzed moving forward.

	Slope of the Line of Best Fit (mm/mm)	R^2 Value
Changing Periodicity v. Ellipse Axis Length	-0.3151	0.3115
Changing Porosity v. Ellipse Axis Length	-1.3542	0.922

Table 5.1 The slope of the line of best fit and the correlation coefficient for the models that relate the change in the axis of the confidenc ellipse when changing either the size or spacing of the pore in the phantom models.

	Slope of the Line of Best Fit (mm^2/mm)	R^2 Value
Changing Periodicity v. Ellipse Area	-29.624	0.2991
Changing Porosity v. Ellipse Area	-128.71	0.8782

Table 5.2 The slope of the line of best fit and the correlation coefficient for the models that relate the change in the area of the confidenc ellipse when changing either the size or spacing of the pore in the phantom models.

From the phantom results, the magnitude of the slope of the line of best fit is greater for the cases where the periodicity was held constant, and the size of the pores were changed. The slope of the line of best fit was approximately four times larger in this case for both the ellipse axis length and the elliptical area. This shows that the FFT response is more sensitive to detect changes in the length or size of the individual pores rather than the spacing between the pores. The phantom test modes that change the size of the pore also have larger R^2 value when compared to the models that changed the spacing between the pores. This shows that the variability in the size and shape of the ellipse is better explained by the change in the size of the ellipse, making it a better predictor for analyzing the dominant peaks of the FFT.

5.2. Pore Length -Minor Axis Direction (Spatial Domain)

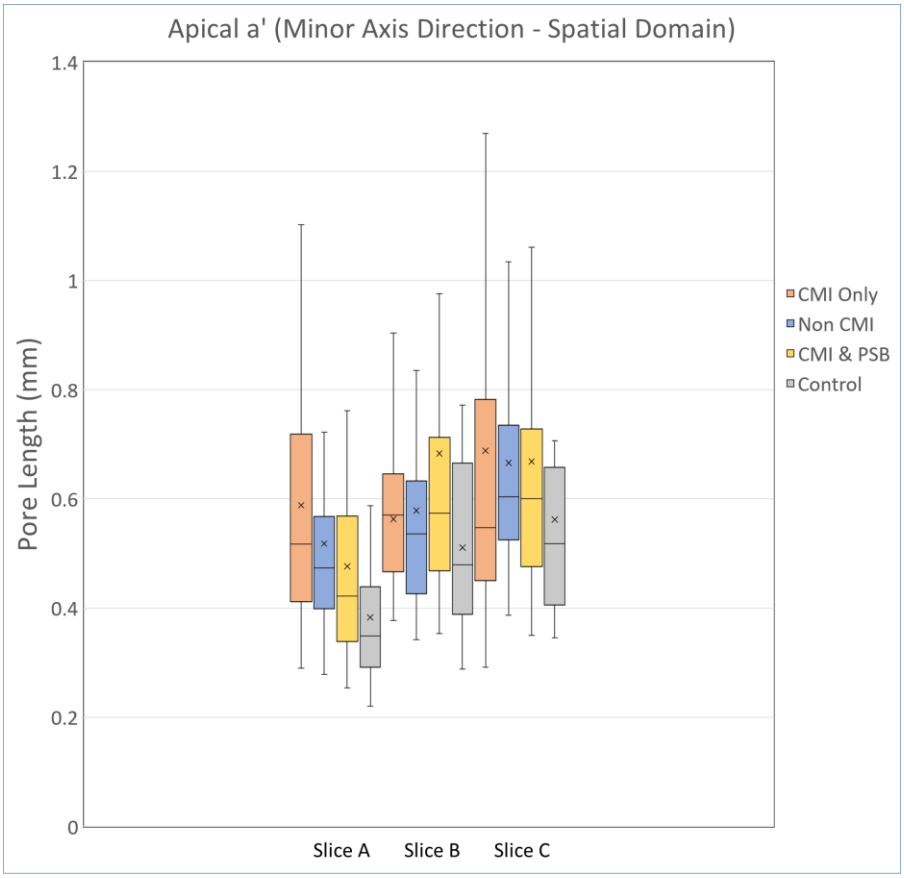

Figure 5.1 The box and whisker plots from the data showing the average length of the minor axis of the individual pores in the spatial domain in the bone in the apical region across all three slices.

The average pore length in the minor axis direction of the pore of the spatial domain yields the graph above. The smaller this number is correlates to an average smaller pore length along of the pores in the selection window in this direction. The average length of pore in the minor axis of the pore in the spatial domain was the smallest in the control group across all slices. This group has had no exposure to race training. In slice A and C, the CMI only group had the largest pore length with the CMI & PSB fracture group having the highest spacing in slice B. As you move from slice A to slice C, there is a noticeable trend that the average for all four groups increases as you move from

one slice to the next. The graph provides initial information that exposure to race training increases the pore length in all slices in the apical area. It is interesting to note that bone that are likely to fracture could be indicated by the peak in porous spacing in slice B for this area.

For the pore length in the minor axis direction in the spatial domain in the midbody area of the bone, some of the same trends were notices. The control group still yielded the smallest length across all three slices with the overall averages increasing from slice A to slice C. However, the non-CMI group presented with the largest length in the minor axis in slice B and C. In slice A, all three racing training groups were around the same average.

For the basilar region, again, the control group presented with the lowest average pore length and the average length among all the groups increased from slice A to C. The differences in the three race training groups were less pronounced throughout moving from slice A to C. The CMI only and CMI & PSB groups did have a noticeably higher average length in slice B when compared to the non-CMI group.

	A' (Minor Axis Direction – Spatial Domain) Averages (mm)								
	Apical			Midbody			Basilar		
Slice:	A	B	C	A	B	C	A	B	C
CMI only	0.5884	0.5629	0.6882	0.4723	0.5558	0.7748	0.3699	0.4533	0.5279
Non CMI	0.5179	0.5786	0.6658	0.4720	0.7135	0.8564	0.3815	0.4188	0.5099
CMI & PSB	0.4764	0.6830	0.6684	0.4746	0.4920	0.8084	0.3566	0.4437	0.5137
Control	0.38301	0.5108	0.5624	0.3475	0.3468	0.5685	0.3236	0.3745	0.4728

Table 5.3 The average values for the minor axis length of the individual pores in the spatial domain in the apical, midbody, and basilar regions across all three slices.

5.3. Pore Length – Major Axis Direction (Spatial Domain)

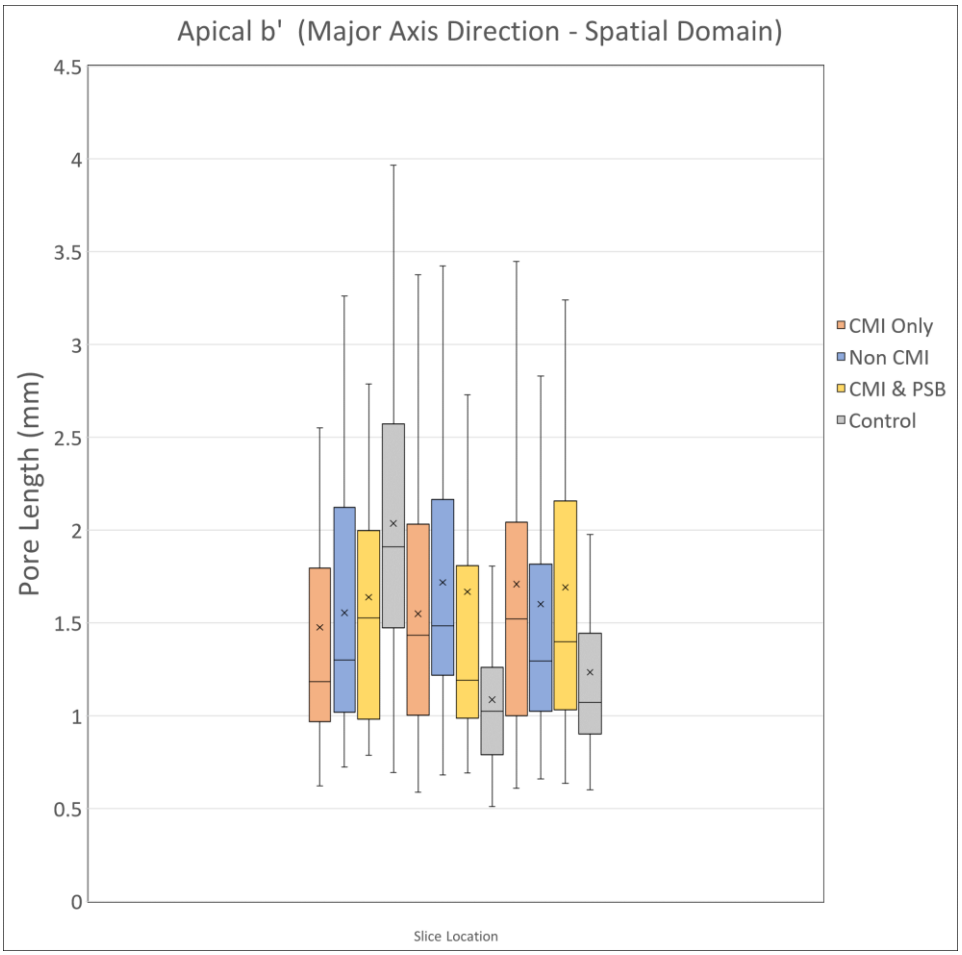

Figure 5.2 The box and whisker plots from the data showing the averaege length of the major axis of the individual pores in the spatial domain in the bone in the apical region across all three slices.

The average pore length in the major axis direction of the pore in the spatial domain for the apical region of the bone is shown above. The higher this parameter is, the larger the average size of the pores in the selection window along their major axis. Surprisingly, the control group exhibits the largest length but just for slice A, then exhibits the smallest length for slices B and C. The overall averages for the groups do not exhibit the same upwards trend from slice A to slice C as seen in the minor axis direction. The averages for the three race training groups stay close to each other as well, with the

non-CMI group having the largest length in slice B and the CMI-only group having the largest length in slice C.

The midbody section shows slightly different results. The control group has the smallest length in all three slices, including slice A. The race training groups show similar results to their apical counterparts. The averages are close in range throughout each slice and a relationship from slice A to slice C is not as apparent. Non-CMI has the largest length in slice A and slice C and CMI-only has the largest length in slice B.

The basilar region for the pore length in the major axis direction shows some interesting data. The control group now has the second highest pore length in slice A and slice B, right behind the non-CMI group which has the largest average in all three slices. The control, however, has the smallest average in slice C. The overall averages also exhibit a slight decreasing trend when moving from slice A to C. This suggest that exposure to race training could either decrease or increase depending on the slice and regional location of the bone.

	B’ (Major Axis Direction) Averages (mm)								
	Apical			Midbody			Basilar		
Slice:	A	B	C	A	B	C	A	B	C
CMI only	1.4757	1.5499	1.7094	1.7095	1.8267	1.6205	1.7562	1.5052	1.2571
Non CMI	1.5545	1.7184	1.6018	1.8546	1.7517	1.6398	1.9677	2.0221	1.3456
CMI & PSB	1.6385	1.6684	1.6912	1.7688	1.5503	1.6335	1.5915	1.5386	1.3085
Control	2.0357	1.0862	1.2343	1.6016	1.1590	0.8675	1.7910	1.5890	1.0112

Table 5.4 The average values for the major axis length of the pores in the spatial domain in the apical, midbody, and basilar regions across all three slices.

5.4. Angle of Rotation (Spatial Domain)

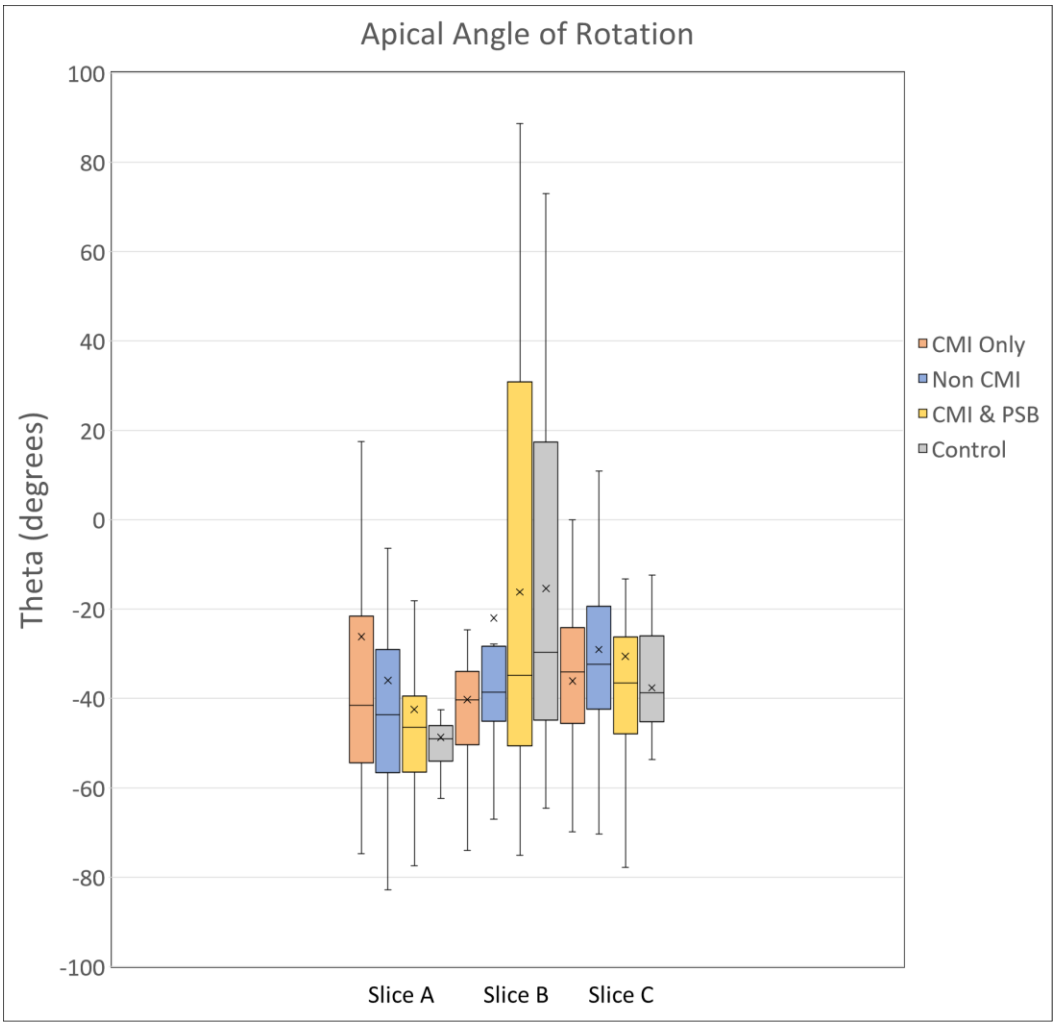

Figure 5.3 The box and whisker plots from the data showing the average anlge of roation of the individual pores in the spatial domain in the bone in the apical region across all three slices.

The average angles of rotation for the confidence ellipses in the spatial domain were stored and recorded. The angle is based on the major axis of the ellipse in the spatial domain. All angles were measured from the positive x-axis. A positive angle of rotation means that the long axis of the ellipse showed a positive rotation from the x-axis (towards the positive y-axis) and a negative angle of rotation means that the long axis of the ellipse showed a negative rotation from the x-axis (towards the negative y-axis). The data for the

apical region is shown above. The control group shows the highest magnitude of rotation in slice A and slice C and the lowest magnitude in slice B. The magnitude of the CMI & PSB fracture group is very similar in slice B, but both have high variability in slice B as well. The CMI-only group has the smallest magnitude in slice A and the non-CMI group has the smallest magnitude in slice C

For the midbody region, all averages were smaller in magnitude. The control group had the smallest angle of rotation in slice A, but had the highest magnitude for the angle of rotation in slice C. The non-CMI group had the smallest angle of rotation in slice B with the control being second smallest. The CMI-only group had the smallest magnitude for the angle of rotation in slice C.

In the basilar region the control group has the highest magnitude for the angle of rotation in slice A and slice B, but the lowest magnitude in slice C. CMI- only has the smallest average magnitude for the angle of rotation in slice A as does the non-CMI group for slice B. The CMI & PSB fracture group has the highest average magnitude for the angle of rotation in slice C. This preliminary data shows that the exposure of race training could have an effect on the orientation of the porous network within the bone, and it could have a greater effect in some areas more than others to remodel the bone in accordance with the outside forces.

	Angle of Rotation Averages (degrees)								
	Apical			Midbody			Basilar		
Slice:	A	B	C	A	B	C	A	B	C
CMI only	-26.1566	-40.2932	-36.1215	-8.3930	-10.2337	1.4454	21.3653	22.4974	19.0551
Non CMI	-35.9722	-22.0026	-29.0608	-6.1094	2.1073	8.0985	21.7225	18.6877	20.0936
CMI & PSB	-42.4824	-16.2206	-30.5926	-7.0929	-13.7677	2.4104	22.1595	19.2856	26.1581
Control	-48.7358	-15.3838	-37.6184	-2.5126	-3.8004	9.2649	24.2819	27.5406	13.9896

Table 5.5 The average values for the angle of rotation of the individual pores in the spatial domain in the apical, midbody, and basilar regions across all three slices.

5.5. Spacing Ratio

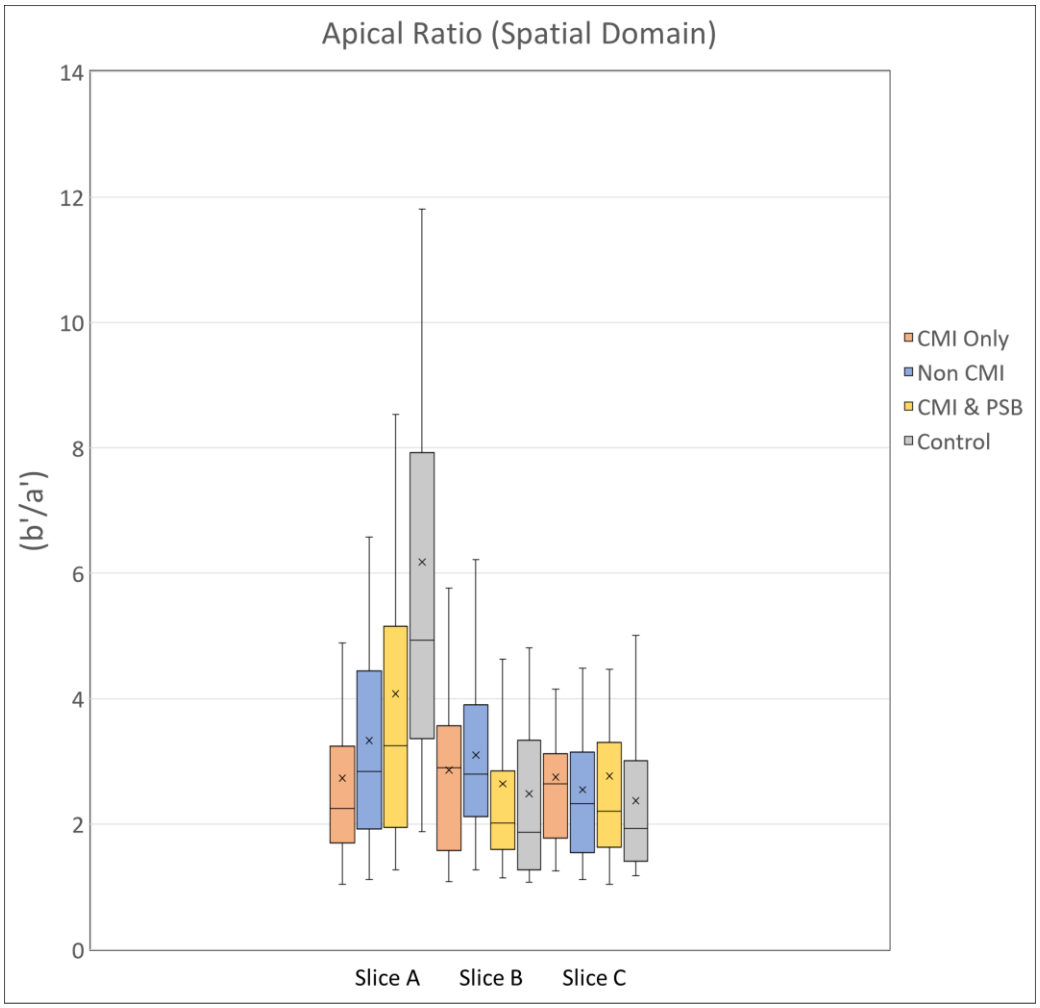

Figure 5.4 The box and whisker plots from the data showing the average ratio of the major axis to the minor axis of the indidvidual pores in the spatial domain in the bone in the apical region across all three slices.

The ratio is a representation of the length of the pore in the along the major axis divided by the length of the pore along the minor axis. The higher the ratio, the higher average elongation in the shape of the pores in the network for that specific area. The control group has the largest shape ratio in slice A, but the smallest shape ratio in slices B and C. The CMI only group has the smallest ratio in slice A, the non-CMI group has the

highest shape ratio in slice B, and the CMI & PSB fracture group has the highest shape ratio in slice C.

The control group had the highest shape ratio in slice A for the midbody region as well, with the second highest ratio in slice B, and the smallest ratio in slice C. The non-CMI group had the smallest ratio in slice A and in slice B. The CMI & PSB fracture group had the highest ratio in slice B and the CMI only group had the highest ratio in slice C. The three race training groups all had similar averages in slice A and slice C.

Similar trends are present in the basilar region like they are in the midbody region. Again, the control group had the highest average ratio in slice A for the midbody region as well, with the second highest average ratio in slice B, and the smallest average ratio in slice C. However, the CMI & PSB fracture group had the smallest average ratio in slice A, and the CMI only group had the smallest average ratio in slice B. The non-CMI group had the largest average ratio in slice B and slice C. Overall, there was a downward trend among the averages moving from slice A to slice C. This data could indicate that the shape of the porous network could be reason for injury. In most cases, the race training had modified the shape to some extent, decreasing the elongation in some regions and increasing the elongation in others, when using the control shape as reference.

	Shape Ratio Averages (mm/mm)								
	Apical			Midbody			Basilar		
Slice:	A	B	C	A	B	C	A	B	C
CMI only	2.7334	2.8616	2.7504	4.0910	3.3605	2.2203	5.1995	3.5708	2.4591
Non CMI	3.3341	3.0990	2.5490	3.9915	2.7420	1.9052	5.4751	5.6855	2.7332
CMI & PSB	4.0801	2.6403	2.7661	4.1861	3.6692	2.1341	4.8790	3.7098	2.6622
Control	6.1789	2.4848	2.3725	5.0648	3.5523	1.5576	5.8275	4.7869	2.3955

Table 5.6 The average values for the ratio of the major axis to the minor axis of the individula pores in the spatial domain in the apical, midbody, and basilar regions across all three slices.

5.6. Spatial Area

The average spatial area for the pores was estimated using the equation:

$$Spatial\ Area = \left(\frac{a'}{2}\right) * \left(\frac{b'}{2}\right) * \pi \quad (9)$$

If a' and b' can be assumed to be the distance of the minor axis and major axis, respectfully, then half of that distance would be the radius of a single pore in each direction. The average radius of the minor axis and major axis can be estimated using this method and then input into the normal equation for the area of an ellipse. This area represents the average area of the pores in the spatial domain. The larger this calculated area is, the larger the average size of the pores in the spatial domain.

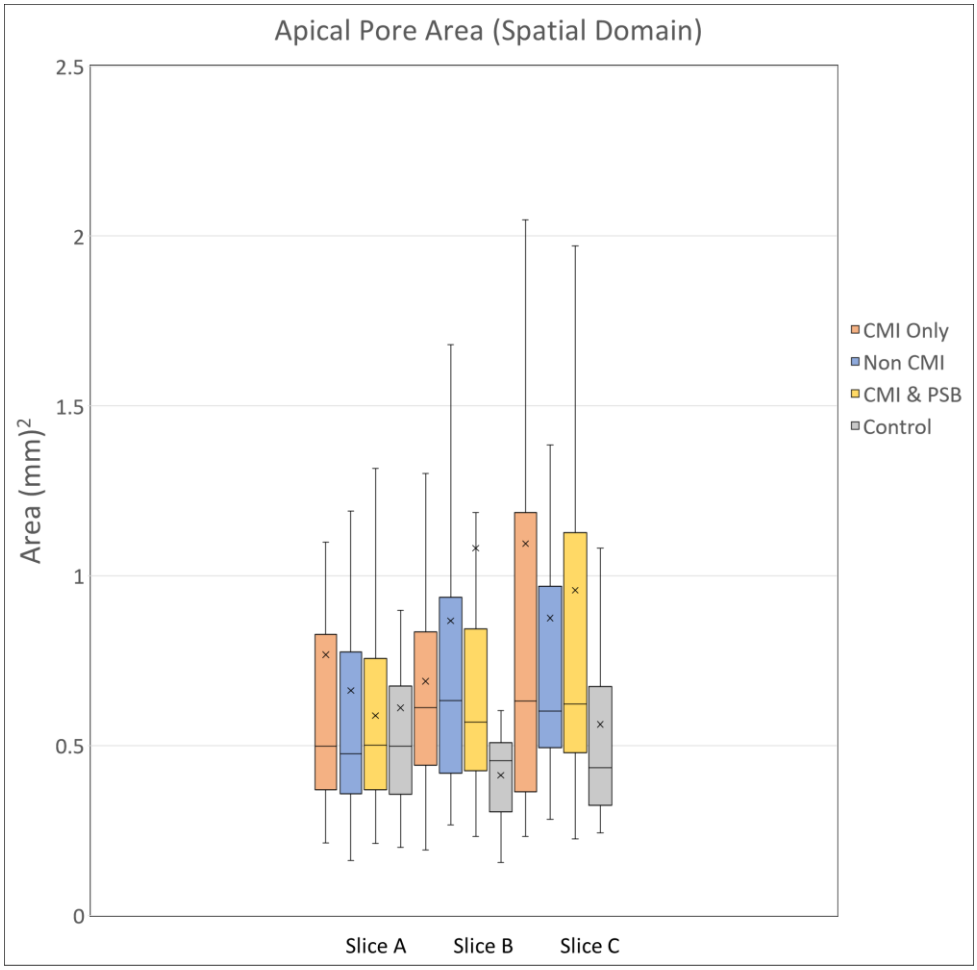

Figure 5.5 The box and whisker plots from the data showing the average area of the individual pores in the spatial domain in the bone in the apical region across all three slices.

The CMI-only group has the largest average pore size for slice A and slice C, while the CMI & PSB fracture had the largest average pore size in slice B, but the smallest average pore size in slice A. The control group had the smallest average pore size in slice B and slice C. There seems to be a slight trend of the average pore size increasing across all groups as one moves from slice A to slice C.

The midbody region holds similar results. The control group now has the smallest average pore size across all slices, and the non-CMI group has the largest average pore

size across all slices. The trend of increasing from moving from slice A to slice C is still present. The difference between the control average and the three race training averages is greater in the midbody regions and has increased in all slices.

The average size of the pores in all slices for all groups decreased in the basilar region. The non-CMI group still has the largest pore size across all slices, and the control group has the smallest average in slice B and slice C. The CMI & PSB fracture group has the smallest average pore size in slice A. This shows to some degree how the bone will remodel and change when exposed to outside forces. In some cases, the indication that the CMI & PSB fracture group has the highest or lowest area in that region could serve as an indicator of fracture, but more research needs to be done.

	Pore Area Averages (mm^2)								
	Apical			Midbody			Basilar		
Slice:	A	B	C	A	B	C	A	B	C
CMI only	0.7674	0.6894	1.0943	0.6923	1.0321	1.1148	0.5152	0.5355	0.5561
Non CMI	0.6622	0.8668	0.8753	0.9481	1.2682	1.3884	0.6317	0.6289	0.5632
CMI & PSB	0.5883	1.0814	0.9570	0.7040	0.6283	1.2175	0.4377	0.5385	0.5480
Control	0.6108	0.4128	0.5623	0.4593	0.3233	0.3978	0.4577	0.4491	0.3737

Table 5.7 The average values for the areas of the individual pores in the spatial domain in the apical, midbody, and basilar regions across all three slices.

5.7. Fracture Mode Comparison a' (Spatial Domain)

The data was then further analyzed based on comparing the specific types of fractures to the rest of the bones that did not fracture. There were five (5) different types of fractures that existed within the overall CMI & PSB fracture group. These subcategories were looked at to see if there were any regional differences in the areas where the fractured occurred compared to the rest of the groups.

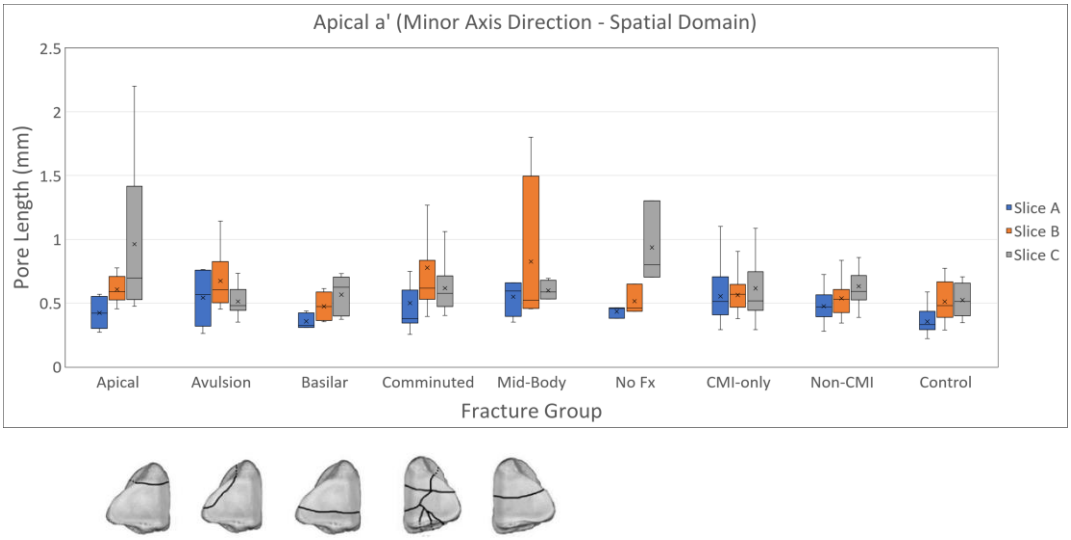

Figure 5.6 The box and whisker plots from the data showing the average length of the minor axis of the individual pores in the spatial domain in the bone in the apical region across all three slices. These plots are organized by the fracture they sustained or the study poulation that they are a part of. The bones below the fracture types depict the type of fracture that they sustained.

The graph above shows the same parameter as shown before (pore length in the minor axis direction), but this graph shows the box and whisker plots groups by the bone distinction with the three (3) different slice locations grouped together. This graph shows only pore length in the apical region of the bone. Of interest, there is an increase in the spacing in this region in slice C present in the bone that experienced apical fractures. This could serve as a physical biomarker for marking bones that are prone to this type of

fracture. However, the population of the apical fractured bones is still very small, and more research and statistical analysis needs to be done to prove the validity of this marker. This large a' value is only present in the apical region and not in the midbody or basilar region, which supports the claim that this increase in the parameter could be caused by the fracture that occurred in that region.

5.8. Fracture Mode Comparison b' (Spatial Domain)

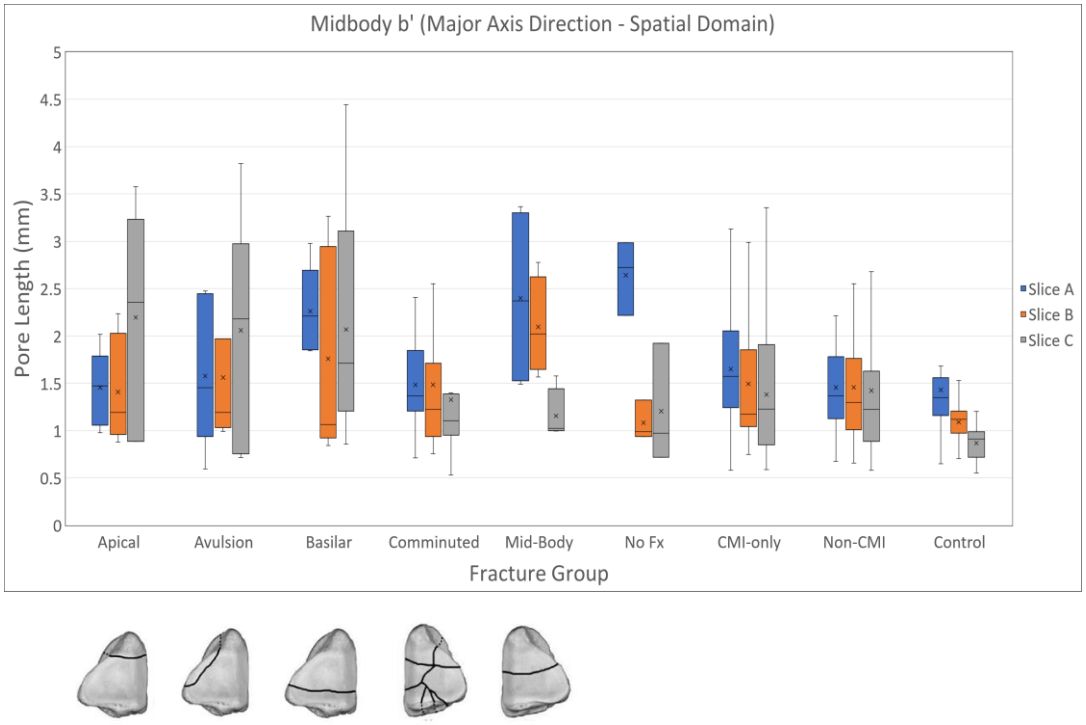

Figure 5.7 The box and whisker plots from the data showing the average length of the major axis of the individual pores in the spatial domain in the bone in the midbody region across all three slices. These plots are organized by the fracture they sustained or the study poulation that they are a part of. The bones below the fracture types depict the type of fracture that they sustained.

Something of similar nature happens in the midbody region when analyzing the pore length in the major axis direction in the spatial domain. When comparing the group that experienced a fracture in the midbody region, it is noticeable that they have the highest

average in slice B. While in slice A and slice C, it has an average that is not the highest and seems on par with the rest of the values. The sample size is still small for these fracture groups but adding more data to these groups will increase the power in any statistical While this is still surface level analysis, it holds valuable insight for proposing new hypothesis and testing current data.

5.9. Fracture Mode Comparison Angle of Rotation (Spatial Domain)

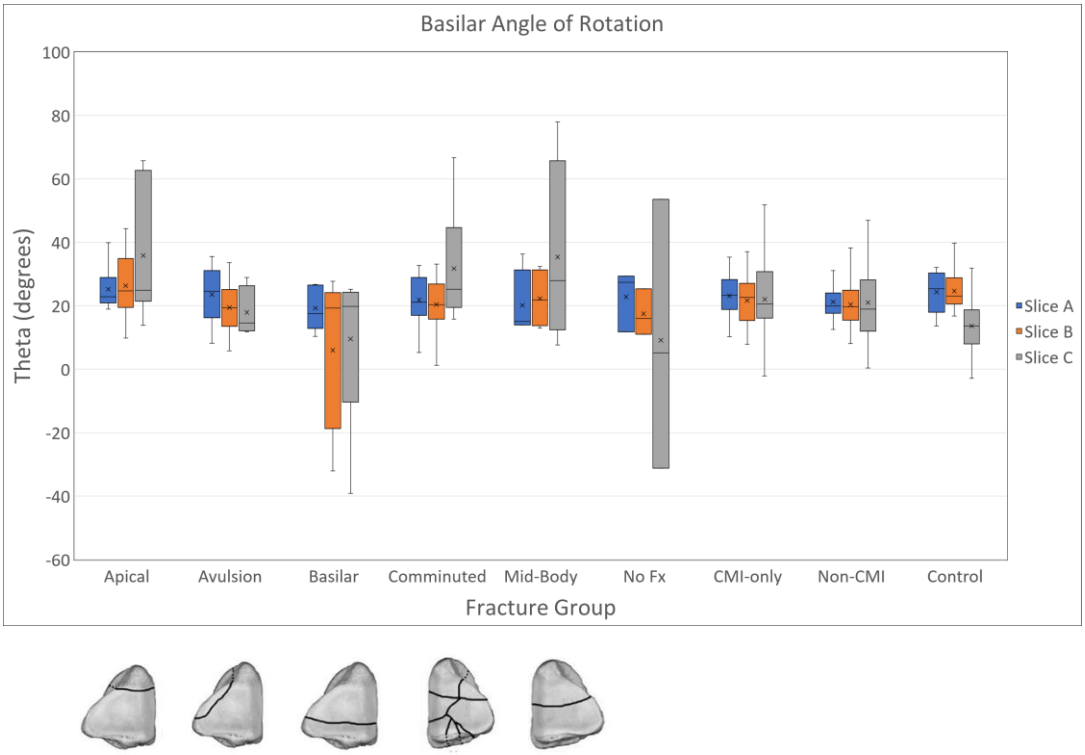

Figure 5.8 The box and whisker plots from the data showing the average angle of rotation of the individual pores in the spatial domain in the bone in the basilar region across all three slices. These plots are organized by the fracture they sustained or the study poulation that they are a part of. The bones below the fracture types depict the type of fracture that they sustained.

Looking into the data further, there can be evidence that there could be an influence due to the fracture looking at the basilar region. The bones with a fracture in the basilar area do show having small angles of rotation for slice B and slice C. The basilar group is also the only group to have values in the negative range for slice B. This distribution could be indicative for increased likelihood to fracture. Again, these differences in distribution for the basilar fracture group are only present when analyzing the porous spacing in the basilar region.

From here statistical models were developed to detect any significance within the distribution of the values. The response variables that were chosen were in the elliptical area and the angle of rotation in the frequency domain. The area would effectively characterize the a' and b' variables at the same time. Therefore, these two models would seek to capture the size and orientation of the internal structure of the bone, both of which are hoped to hold insight into the remodeling process and the reason for failure as well.

CHAPTER 6. STATISTICAL MODELS & DISCUSSION

6.1. Elliptical Area Mixed Model Analysis (Frequency Domain)

Two different mixed models were developed for statistical analysis. These mixed models were used to demonstrate the interaction between biological explanatory variables and a response variable obtained from analyzing the FFT of the porous network. The two response variables that were chosen for analysis were the log output of the elliptical area in the frequency domain and the log output of the angle of rotation in the frequency domain. The frequency domain parameters were chosen over the spatial domain because they represent the raw data before it is processed. The log output of the data was chosen to create more normally distributed variables to reduce the amount of error produced from the model and so as to not overfit the model during the analysis. The raw log transformed data will provide a clearer version of the data before converting to the spatial domain to accurately capture any differences in the data obtained directly from the FFT. The elliptical area and the angle of rotation in the frequency domain in each of the nine (9) regions were used as a response variable in a mixed model in the statistical software JMP v. 16 (SAS Incorporated, Cary, North Carolina, USA). The fixed effect variables that were used in the model to test their significance were as follows: weight, age, leg, bone, sex, experimental group, and porosity. Weight, age, and porosity were continuous variables. Leg, bone, sex, and experimental group were nominal variables; the leg was either the left front or the right front, the bone was either the medial or lateral, the sex was either castrated male, intact male, or female, and the experimental groups were either CMI only, non CMI, CMI & PSB, or control. A backwards elimination technique was used to reduce the number of variables to find a more concise model that best explains the data.

The analysis showed that the response variable of elliptical area had at least one significant variable in four (4) out of the nine (9) regions.

	P-Values								
	Slice A			Slice B			Slice C		
	Apical	Midbody	Basilar	Apical	Midbody	Basilar	Apical	Midbody	Basilar
Weight	--	--	--	--	--	--	-	--	--
Age	--	--	0.0073*	--	--	--	--	--	--
Leg	--	--	--	--	--	--	--	--	--
Bone	--	--	--	--	--	--	--	--	--
Sex	--	--	--	--	--	--	--	--	--
Experimental Group	--	--	--	--	--	--	--	0.0320*	--
Porosity	--	--	--	--	0.0220*	--	0.0131*	--	--

Table 6.1 The p-values obtained from using the backwards elimination technique on the mixed model for the statistical analysis with the average elliptical area of the indivudal pores in the frequency domain as the respose variable.

An inverse relationship was found with age in the basilar region of the bone in slice A. As the age of the horse increased, the area of the ellipse decreased in the frequency domain, which means that the size of the ellipse will increase in the spatial domain.

Fixed Effects Parameters Estimates							
Term	Estimate	Std Error	DFDen	t ratio	Prob > |t|	95%Lower	95%Upper
Intercept	2.8687727	0.0726294	41.9	39.50	<.0001*	2.7221879	3.0153574
Age	-0.004418	0.0015664	41.5	-2.82	0.0073*	-0.007581	-0.001256

Table 6.2 The fixed effect parameter estimates from the mixed model where the elliptical area in the basilar region in slice A is the response variable.

In the midbody region of slice C, there was found to be a significant interaction between the different experimental groups. The control group had the highest elliptical area, followed by the CMI only group, then the CMI & PSB group, and then the non CMI group. The CMI & PSB fracture and non CMI groups were very similar. The control would then have the smallest average pore area in the spatial domain, followed by the CMI only group, then the CMI & PSB group, and the non CMI group.

Least Squares Means Table			
Level	Least Sq Mean	Std Error	Mean
CMI & PSB	2.4337397	0.06389959	2.41545
CMI only	2.4475011	0.06809750	2.45317
Control	2.6913601	0.12662402	2.75463
Non CMI	2.3964281	0.06306881	2.40030

Table 6.3 The least square means table of the experimental group variable from the mixed model where the elliptical area in the midbody region of slice C was the response variable.

The porosity of the bone was found to be significant in two regions, the midbody in slice B and the apical region of slice C. In both cases, a positive linear relationship between the porosity and the elliptical area in the frequency domain was found. This means that as the porosity increases, the average size of the pore in the spatial domain decreases. This is also corroborated by the high number of trabecular connections within porous bone. High porosity has also been associated with the control group, horses that have no had race training. This means that prior to race training, the number of pores is larger, but the average size is smaller. When exposed to the racing stimuli, the bone works to remodel to become stronger by consolidating the pores, decreasing the trabecular connections and number of pores but increasing the average size of the individual pore.

Fixed Effects Parameters Estimates							
Term	Estimate	Std Error	DFDen	t ratio	Prob > |t|	95%Lower	95%Upper
Intercept	2.3457817	0.1106733	59.7	21.20	<.0001*	2.1243802	2.5671831
Porosity	2.0596383	0.8747732	58.1	2.35	0.0220*	0.3086353	3.8106413

Table 6.4 The fixed effect parameter estimates from the mixed model where the elliptical area in the midbody region in slice B is the response variable.

Fixed Effects Parameters Estimates							
Term	Estimate	Std Error	DFDen	t ratio	Prob > |t|	95%Lower	95%Upper
Intercept	2.2706055	0.0864954	56.0	26.25	<.0001*	2.097331	2.4438799
Porosity	1.7496467	0.6815224	53.0	2.57	0.0131*	0.3827082	3.1165852

Table 6.5 The fixed effect parameter estimates from the mixed model where the elliptical area in the apical region in slice C is the response variable.

6.2. Elliptical Angle of Rotation Mixed Model Analysis (Frequency Domain)

A second mixed model was developed using the same explanatory variables for testing the fixed effects, but the response variable measured in this model was the angle of rotation of the porous network in each region taken from the bone.

	P-Values								
	Slice A			Slice B			Slice C		
	Apical	Midbody	Basilar	Apical	Midbody	Basilar	Apical	Midbody	Basilar
Weight	--	--	--	--	--	--	--	0.0069*	0.0099*
Age	--	--	--	--	--	--	0.0374*	--	--
Leg	--	--	--	--	--	--	--	--	--
Bone	--	--	--	--	--	--	--	--	--
Sex	0.0362*	--	--	--	--	--	--	--	--
Experimental Group	--	--	--	--	--	--	--	--	0.0492*
Porosity	--	--	--	--	--	--	--	--	--

Table 6.6 The p-values obtained from using the backwards elimination technique on the mixed model for the statistical analysis with the average angle of rotaion of the individual pores in the frequency domain as the respose variable.

Weight was found to be a significant factor on the angle of rotation in the midbody and basilar regions of slice C. In both cases weight showed to have an inverse relationship with the angle of rotation in the frequency domain. This means that as the weight increases, the angle of rotation also decreases in the spatial domain. In both regions, since these angles are positive, their magnitude also decreases with the increase in weight.

Fixed Effects Parameters Estimates							
Term	Estimate	Std Error	DFDen	t ratio	Prob > |t|	95%Lower	95%Upper
Intercept	2.5427513	0.1954441	14.7	13.01	<.0001*	2.1255264	2.9599761
Weight	-0.001245	0.0003965	14.7	-3.14	0.0069*	-0.002092	-0.000398

Table 6.7 The fixed effect parameter estimates from the mixed model where the elliptical angle of rotation in the midbody region in slice C is the response variable.

Fixed Effects Parameters Estimates							
Term	Estimate	Std Error	DFDen	t ratio	Prob > |t|	95%Lower	95%Upper
Intercept	2.1789362	0.0467467	26.1	46.61	<.0001*	2.0828566	2.2750157
Weight	-0.000262	0.0000942	25.9	-2.78	0.0099*	-0.000456	-6.862e-5
Experimental Groups [CMI & PSB]	0.0220731	0.0076638	54.6	2.88	0.0057*	0.0067119	0.0374342
Experimental Groups [CMI only]	-0.000373	0.007563	24.6	-0.05	0.9611	-0.015962	0.0152163
Experimental Groups [Control]	-0.01309	0.0104543	24.4	-1.25	0.2224	-0.034649	0.0084681

Table 6.8 The fixed effect parameter estimates from the mixed model where the elliptical angle of rotation in the basilar region in slice C is the response variable.

The experimental group was found to have a significant effect in the basilar region of slice C. The control group had the smallest angle of rotation in the frequency domain, followed by the CMI only group, followed by the non CMI, with the CMI & PSB having the highest angle of rotation in the frequency domain. Since these angles are in the apical region, the control group had the smallest magnitude for the angle of rotation in the spatial domain, followed the CMI only group, followed by the non CMI group, with the

CMI & PSB group having the largest magnitude of the angle of rotation in the spatial domain.

Least Squares Means Table			
Level	Least Sq Mean	Std Error	Mean
CMI & PSB	2.0723687	0.00856967	2.07273
CMI only	2.0498279	0.00866293	2.04637
Control	2.0375147	0.01374429	2.03290
Non CMI	2.0416032	0.00864099	2.04640

Table 6.9 The least square means table of the experimental group variable from the mixed model where the elliptical angle of rotation in the basilar region of slice C was the response variable.

The sex of the horse was found to be a significant factor in the apical region of slice A. The intact male had the highest angle in the frequency domain, followed by the castrated male, followed by the female group. Since these angles are in the apical region, the intact male has the smallest magnitude of angle of rotation in the spatial domain followed by the castrated male, followed by the female group.

Least Squares Means Table			
Level	Least Sq Mean	Std Error	Mean
Castrated Male	1.6657995	0.04288190	1.66580
Female	1.6208132	0.02929391	1.62081
Intact Male	1.7186584	0.03275159	1.71866

Table 6.10 The least square means table of the sex variable from the mixed model where the elliptical angle of rotation in the apical region of slice A was the response variable.

The age of the horse was found to be a significant factor in the apical region of slice C. The age of the horse was found to have a linear relationship with the angle of rotation in the frequency domain. Since these angles are in the apical region, the age has an inverse relationship with the magnitude of the angle of rotation in the spatial domain.

Fixed Effects Parameters Estimates							
Term	Estimate	Std Error	DFDen	t ratio	Prob > |t|	95%Lower	95%Upper
Intercept	1.6149697	0.052977	41.1	30.48	<.0001*	1.50799	1.7219494
Age	0.002462	0.0011445	41.2	2.15	0.0374*	0.000151	0.004773

Table 6.11 The fixed effect parameter estimates from the mixed model where the elliptical angle of rotation in the apical region in slice C is the response variable.

In total for the elliptical area model, there were four (4) regions that saw significant interaction from the explanatory variables. There were three (3) different

variables that caused these interactions, and one variable caused an interaction in two different regions.

For the angle of rotation model, there were again four (4) regions that saw a significant interaction, but they were not the same regions as seen in the elliptical area model. There were four (4) different variables that caused these interactions, two of which were the same variables seen in the elliptical area model. In the elliptical model out of the four (4) total interactions, the distribution of interactions in the slices is: 1 in slice A, 1 in slice B, and 2 in slice C. The distribution of interactions among the regions is: one (1) in the apical region, 2 in the midbody region, and 1 in the basilar regions. In the elliptical angle of rotation model out of the five (5) total interactions, the distribution across the slices is: 1 in slice A, 0 in slice B, and 4 in slice C. The distribution among the regions is: two (2) in the apical regions, 1 in the midbody region, and 2 in the basilar region.

From this data, the elliptical area is seen to have to most interactions in slice C or in the midbody region. The elliptical angle of rotation is seen to have to have the most interaction in slice C or in the apical or basilar region. Slice C was shown to have the most interactions, this could mean that if another slice was taken even more lateral from the midline of the leg, then perhaps even more interactions could be captured.

CHAPTER 7. CONCLUSION

7.1. Conclusion

The purpose of this study was to perform an investigative analysis into the internal structure of the equine PSB in hopes of expanding the edge of knowledge on this bone and on its fracture modalities. The breakdown of this specific bone is among the most common fatal injuries in the American horse racing industry in general and specifically with Thoroughbred horses as well. In this study, to gain insight into how internal architectural structures of PSB bones affect the modes of fracture, the porous structure of several types of PSB of horses was investigated, including from horses that have not been exposed to race training, racehorses that were euthanized for non-injury related reasons, racehorses that experienced a CMI, and horses that experienced a CMI & PSB. The findings of this study show interesting implications for the idea that the PSB is regionally changing the internal nature of the bone which lead to changes in structural integrity. The control group had the smallest average pore area in the majority of the different regions analyzed (7 out of 9). This presents the fact that race training could be a factor in increasing the size of the individual pores within the bone. The fact that this is not seen in all 9 regions also suggests that the race training could affect some regions at a higher capacity than others, suggesting that the affect is spatially dependent within the bone. This is also seen with the comparisons made with the individual fracture modes within the overall CMI & PSB fracture group. It was observed that there were regional differences in the fracture types that could correspond with their specific fracture. It was seen that the apical fracture group had the largest average pore length in the minor axis direction in slice C of the apical region, the midbody fracture group had the highest

average pore length in the major axis direction of slice B of the midbody region, and the basilar fracture group had the smallest angle of rotation in slice B of the basilar regions. While these same sizes are still very small and cannot have a sufficient statistical analysis run on them due to the lack of statistical power, these are very interesting observations that the data presents, and could direct future studies to be focused solely on regional differences rather than holistic differences.

The idea that the internal working of the bone is further regionally dependent is further highlighted by the findings of the statistical model that included the effects due to biological factors. Some biological factors are only shown to be significant in certain areas and not in others, while some factors are also only shown to affect the angle of the bone and not the size of the bone. This furthers the complexity the nature of the fracture of this bone, because it was theorized that both the size and shape of the porous network, and now the models show that each is affected differently at different locations. This shows that there is a lot to look at when examining the integrity of the bone, and with the high variation among the regions, propensity to fracture could increase in certain areas. This could be why there is a variation in the types of fractures that are seen. Looking at the specific differences and biological factor effects, we can pinpoint which regions are experiencing changing due to the specific factors.

It was observed that the control had the smallest pore length along the minor axis of the individual pore in all nine (9) regions and had the smallest pore length in the major axis of the pore in six (6) out of the nine (9) regions. It was also observed that the control group had the smallest average individual pore area in seven (7) out of the nine (9) regions.

In the mixed model analysis of the elliptical area in the frequency domain (the raw data), weight was found to have an inverse relationship with the frequency domain area and a positive linear relationship with the spatial domain area in the apical region of slice A, age was found to have an inverse relationship with the frequency domain area and a positive linear relationship with the spatial domain area in the basilar region of slice A, and the porosity was found to have a positive linear relationship with the frequency domain area and an inverse relationship with the spatial domain area in the midbody region of slice B and the apical region of slice C. The different PSB bones (medial v. lateral) were found to have a significant effect in the apical region of slice B along with the sex of the horse (female v. intact male v. castrated male) in the same region. The lateral PSBs were found to have smaller average pore sizes in the spatial domain when compared to the medial PSBs. Females were found to have the smallest average pore size in the spatial domain when compared to the castrated and intact males; castrated males had the largest average pore size. The different experimental groups were found to have a significant effect in the midbody region of slice C. The control group had the smallest average pore size, followed by the CMI only group, then the CMI & PSB group, and then the non CMI group had the largest average pore size by a small margin.

In the mixed model analysis for the angle of rotation in the frequency domain for the pores, weight was found to have a significant effect in both the midbody and basilar regions of slice C. In both regions, there was an inverse relationship found with the weight and the angle of rotation in the frequency domain. Looking at the data, this corresponded to an inverse relationship with the magnitude of the angel of rotation in the spatial domain as well. As the weight increased, the magnitudes of the angles of rotation

decreased. Age was found to have a significant effect in the apical region of slice C. As the horse aged, the angle of rotation increased in the frequency domain. The angles in the apical region are in the first quadrant in the frequency domain, however. When these angles are translated to the spatial domain, the magnitude of the angles decreases with the increasing weight. Another factor having a significant effect on slice C is the different experimental population groups. The control had the lowest angle of rotation and the CMI & PSB fracture group had the highest average angle of rotation. In the spatial domain, this translates to the control group having the smallest average magnitude for the angle of rotation and the CMI & PSB fracture group having the highest average magnitude for the angle of rotation. The sex of the horse was found to significantly affect the apical region of slice A. The female had the lowest average angle of rotation in the frequency domain and the intact males had the highest average angle of rotation in the frequency domain. This corresponds to the females having the highest average magnitude for the angle of rotation in the spatial domain and the intact males having the lowest average magnitude for the angle of rotation in the spatial domain.

These findings could help establish certain physiological practices to help monitor the health of the PSB and to improve the overall health of the horses in the racing industry in hopes of decreasing mortality rates.

7.2. Study Limitations

The nature of this research study is limited in a few aspects. The horses that were analyzed were ones that were only a part of the Kentucky Horse Racing Necropsy Program, meaning that all of the horses were regionally based. With that, finding

thoroughbred horses that had not entered race training for the control population was challenging. Only five (5) horses were obtained and one (1) had to be excluded from the study from an underlying lameness issue. Finding exact age and gender matched samples also proved challenging at times. Another limitation is that this study was conducted postmortem for all of the horses. For analyzing the data, when comparing the specific fracture types the sample sizes could be larger for more power when conducting statistical studies. In terms of gathering the data, the resolution of the scans was limited to the capability of the μCT machine used and the desktop computer used for importing the scans and generating the sagittal slices.

7.3. Future Studies

Throughout the course of this research there have been multiple areas of additional research that have been noted that could prove to yield notable results if pursued. In the initial stages of researching the PSB, preliminary FEA testing was performed on singular sagittal slices of the bone to identify areas of high tensile and compressive stresses. A full scale PSB bone is still being made for full bone FEA testing. This study could further refine this protocol. If we can identify the areas that experience the most stress, the ones that will mostly likely remodel the most through mechanotransduction, then we can identify which specific sagittal slice should be analyzed via the FFT. This will also allow us to assess the strength of the bone and gather data for their fracture strength which would then be compared across the four (4) different experimental groups.

Another initial test was to map the internal vasculature of the PSB. The protocol was successful in injecting a contrast agent into the bone and then identifying the contrast agent in the μCT scans and creating a 3D model of the vascular map. It would be further beneficial to do this protocol on bones from the four different experimental groups. The presence, or lack thereof, could then be cross referenced with the strength of the bone and also the regions that have different pore sizes. It is known that blood supplies vital nutrients for bone remodeling; this could then be used to help identify regions of the bone that are not getting a proper nutrient flow. This could then be examined in the fracture group specifically. The region where the fracture occurred could then be evaluated with the vascular density to see if there is a correlation.

Furthermore, when creating the statistical mixed model, there were other morphometric variables that could have been included such as trabecular thickness, trabecular spacing, and trabecular number. It is not known whether they would have provided any statistical insight, so for the sake of simplifying the model, they were excluded. As for the response variable, any of the parameters could have been analyzed individually, but it was decided that the raw data of the frequency data would yield the most comprehensive model, since the elliptical area is a function of the spacing in both directions.

With the data analysis, there is an observed need to do further data collection on the different fracture types in the CMI & PSB fracture group. There is evidence to suggest that there could be structural makers that may serve to indicate the onset of a fracture, but at the current state, the statistical analysis is lacking power. A larger sample size across all of the groups is needed. This group along with the CMI only and non CMI

group would benefit from a group specific analysis. Preliminary data has been collected regarding the different injuries in the CMI only group and the different illnesses in the non CMI group. Further analysis from this could prove to show more information on the overall health of the PSB.

Overall, this exploratory study provided substantial knowledge in a specific area where there was little to begin. A comprehensive database for μCT scans in the sagittal plane has been collected and organized to provide a baseline image repository moving forward in studies. Regional porous structures have been identified and analyzed using FFT technology to compare patterns in the frequency domain that may not be visible in the spatial domain. The inclusion of biological factors in the mixed model analysis allowed factors rather than just the experimental groups to be examined for significant effect on the internal porous structure. There is hope that the results from this study can be further expanded upon by analyzing a greater population of PSB fracture racehorses and cross referencing the results with race training data. The study also provided initial steps for collaborative studies in mechanical testing and vascular perfusion. As the edge of knowledge expands and the PSB is better understood, this data should be used for providing preventative race training programs to monitor the health of the PSB antemortem in hopes of decreasing the fatality rate in this industry and maintaining the health of the horses that are a part of it.

APPENDICES

APPENDIX A.

Supplementary graphs for the data of the 4 experimental groups.

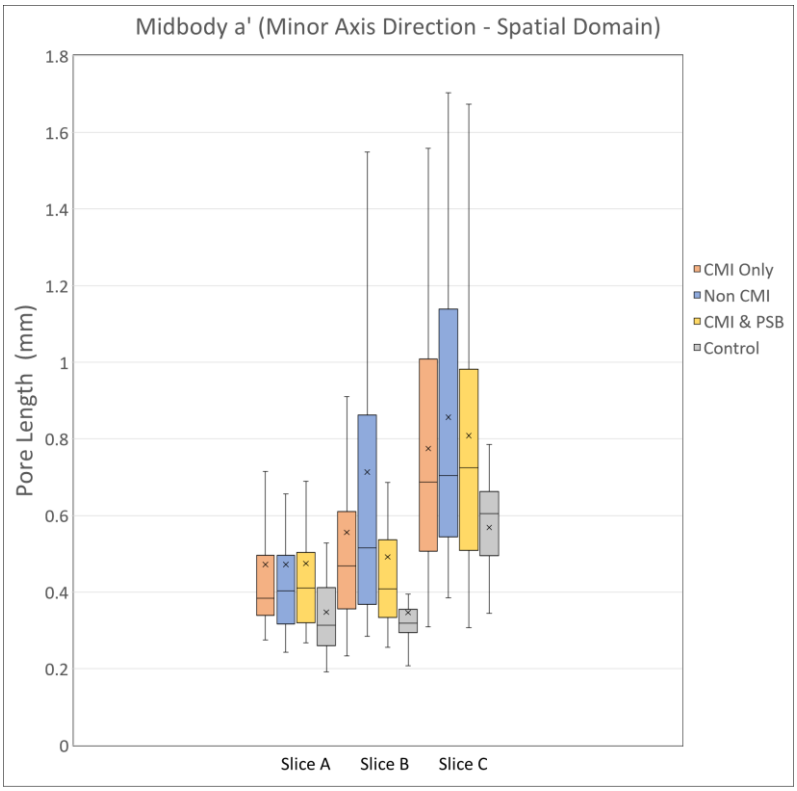

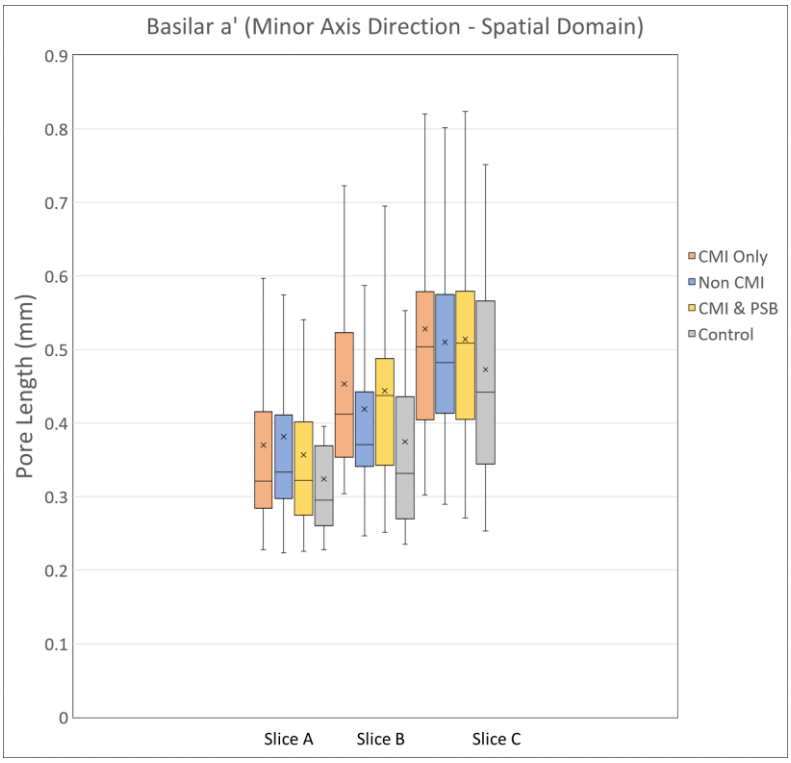
Basilar a' (Minor Axis Direction - Spatial Domain)
Pore Length (mm)
0.9
0.8
0.7
0.6
0.5
0.4
0.3
0.2
0.1
0
Slice A
Slice B
Slice C
CMI Only
Non CMI
CMI & PSB
Control

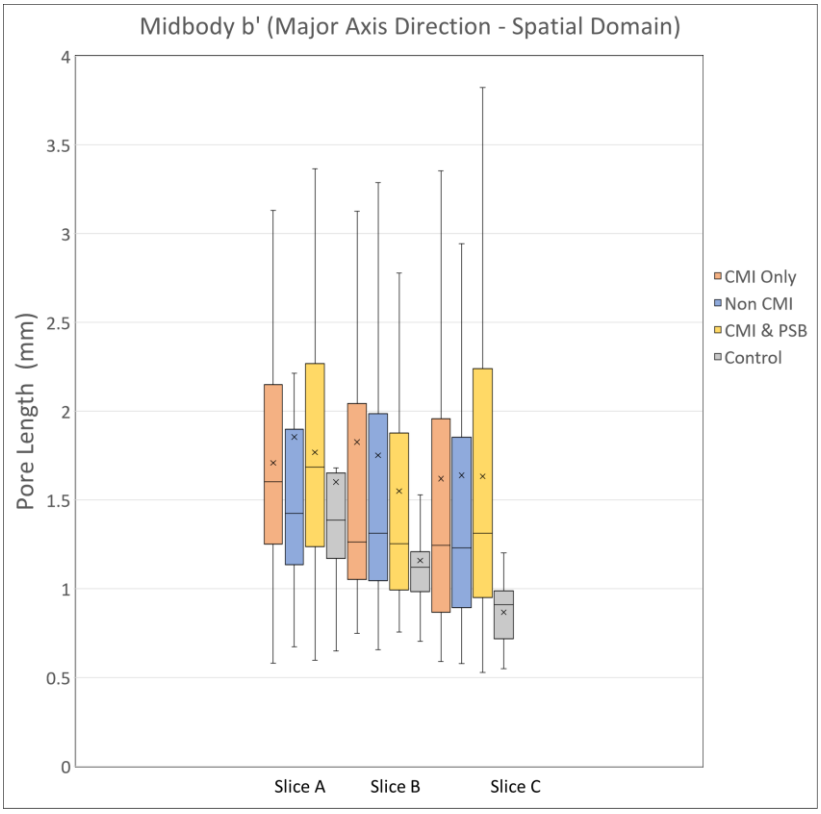
Midbody b' (Major Axis Direction - Spatial Domain)
Pore Length (mm)
4
3.5
3
2.5
2
1.5
1
0.5
0
Slice A
Slice B
Slice C
CMI Only
Non CMI
CMI & PSB
Control

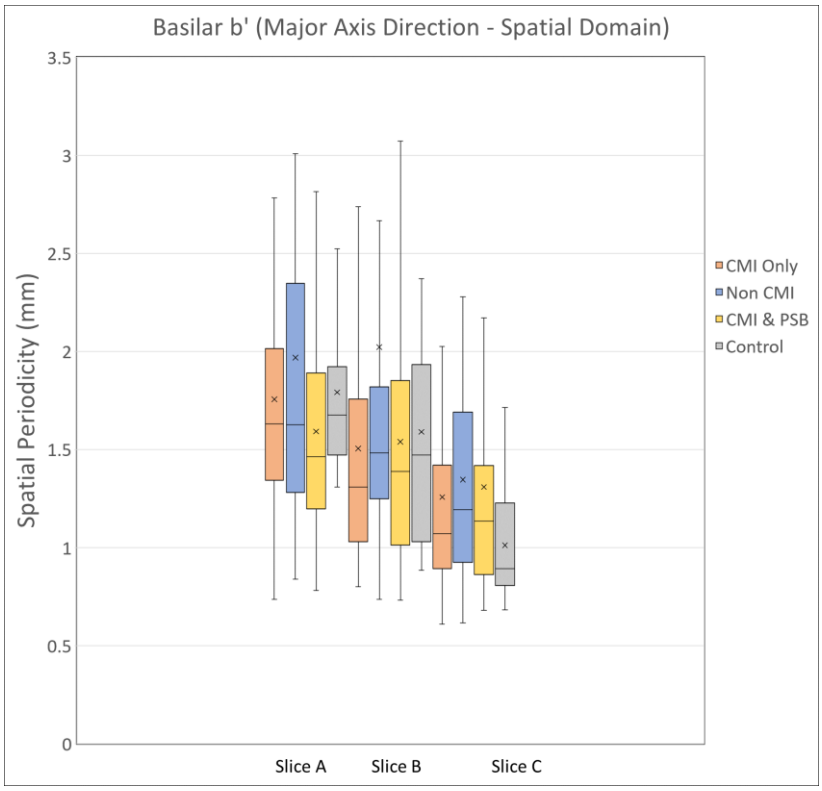
Basilar b' (Major Axis Direction - Spatial Domain)
Spatial Periodicity (mm)
3.5
3
2.5
2
1.5
1
0.5
0
Slice A
Slice B
Slice C
CMI Only
Non CMI
CMI & PSB
Control

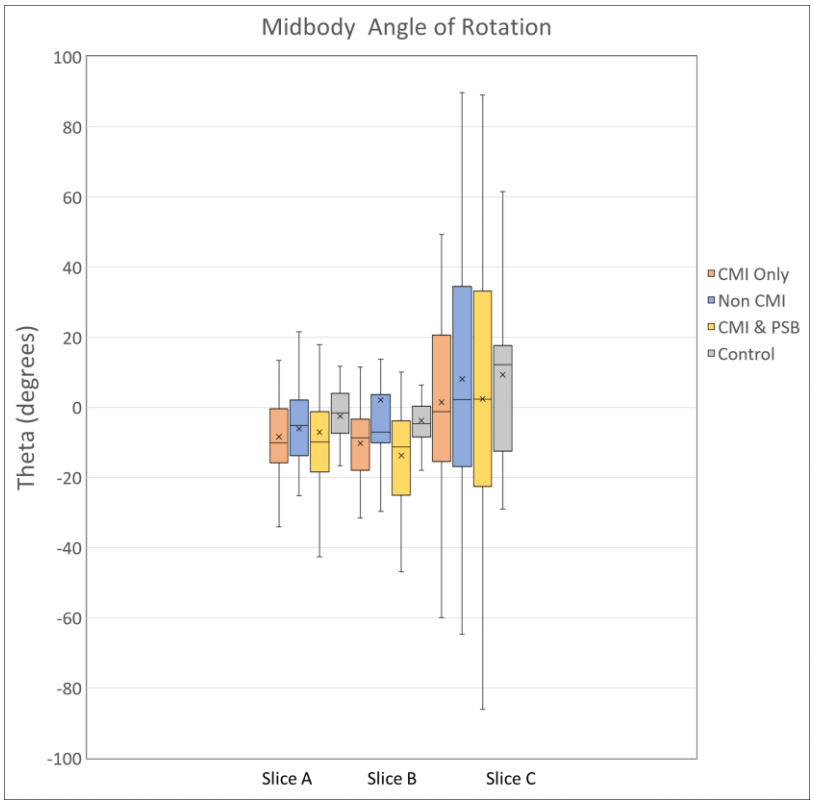
Midbody Angle of Rotation
Theta (degrees)
100
80
60
40
20
0
-20
-40
-60
-80
-100
Slice A
Slice B
Slice C
CMI Only
Non CMI
CMI & PSB
Control

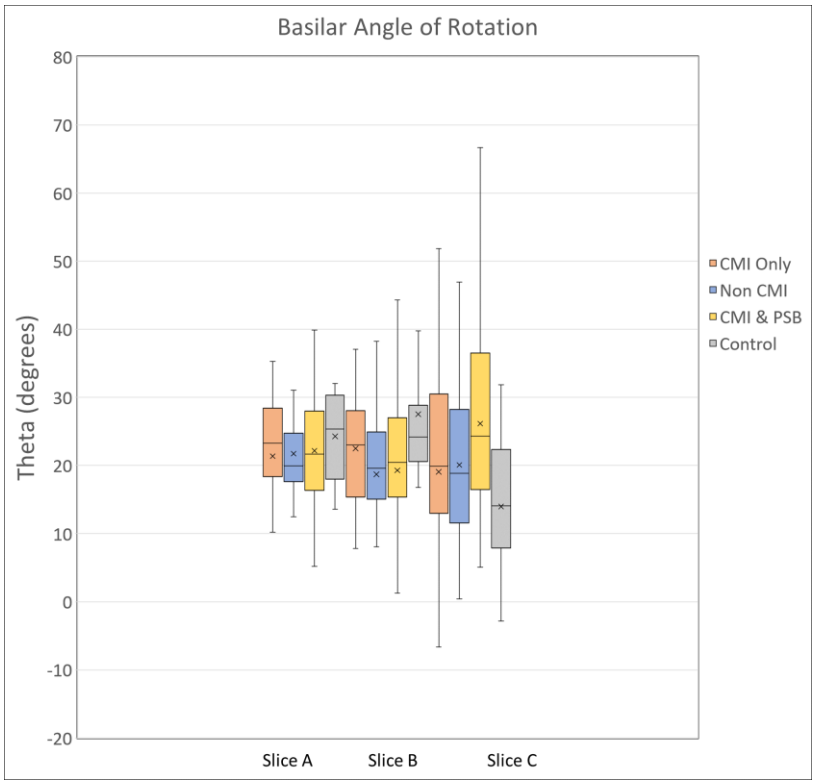
Basilar Angle of Rotation
Theta (degrees)
80
70
60
50
40
30
20
10
0
-10
-20
Slice A
Slice B
Slice C
CMI Only
Non CMI
CMI & PSB
Control

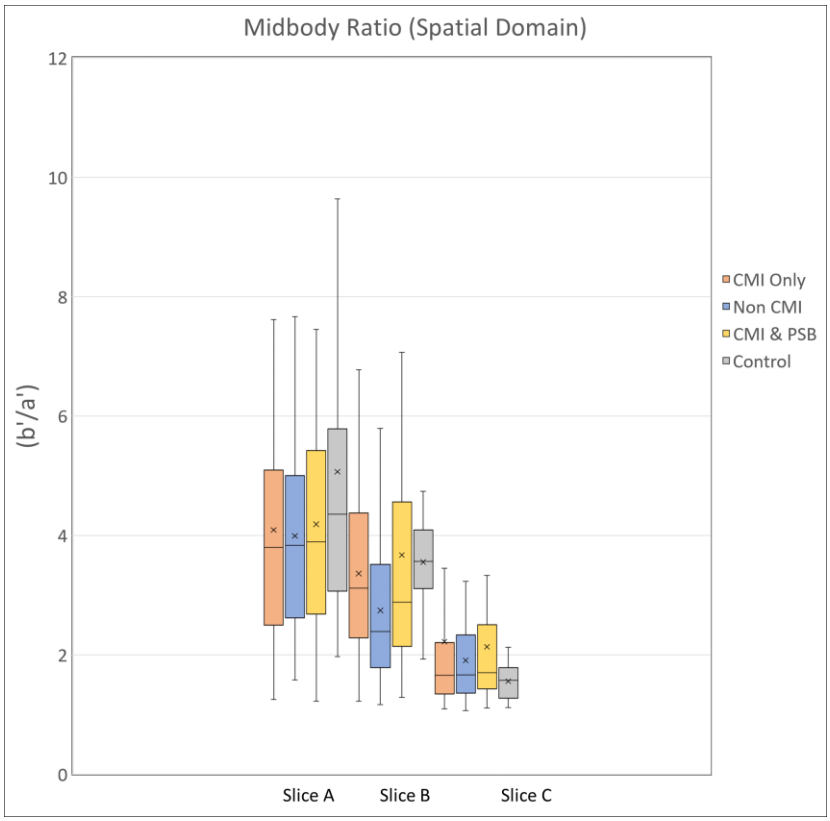
Midbody Ratio (Spatial Domain)
(b'/a')
12
10
8
6
4
2
0
Slice A
Slice B
Slice C
CMI Only
Non CMI
CMI & PSB
Control

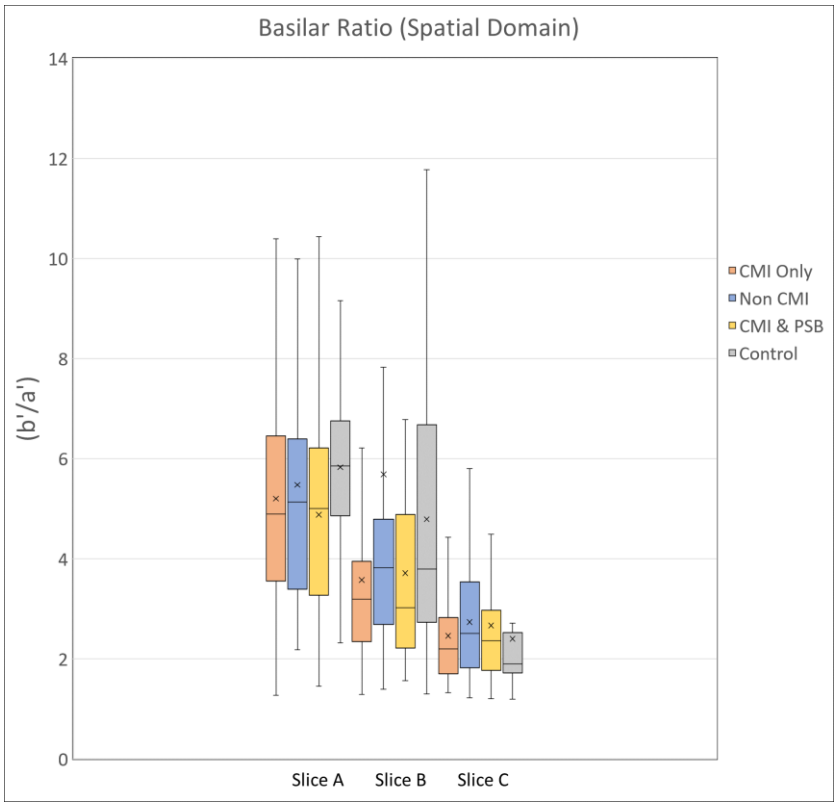
Basilar Ratio (Spatial Domain)
(b'/a')
14
12
10
8
6
4
2
0
Slice A
Slice B
Slice C
CMI Only
Non CMI
CMI & PSB
Control

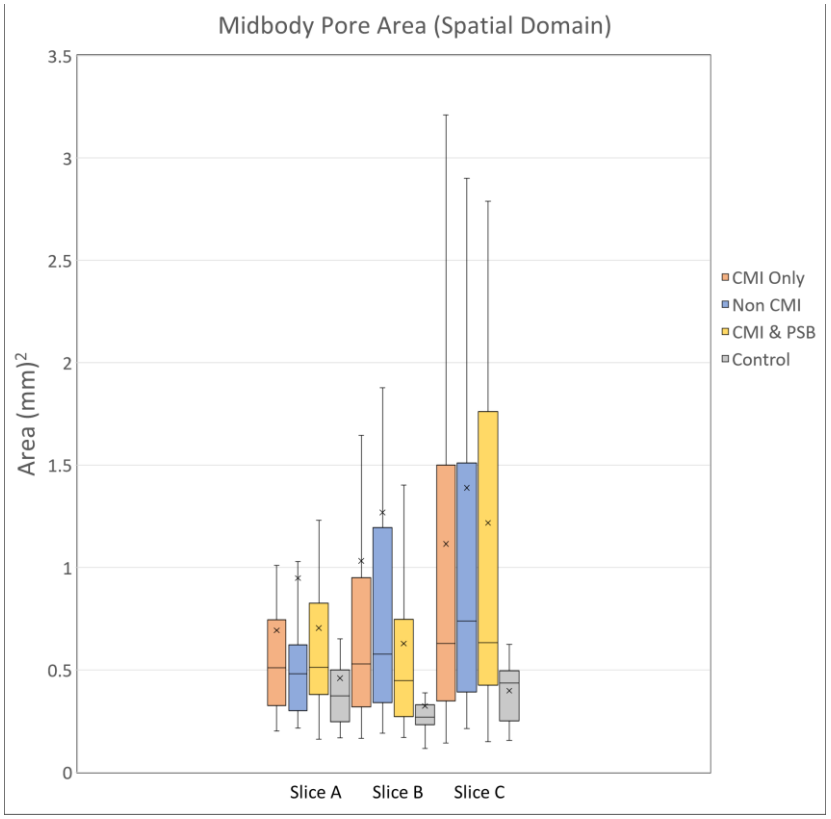
Midbody Pore Area (Spatial Domain)
Area (mm)²
3.5
3
2.5
2
1.5
1
0.5
0
Slice A
Slice B
Slice C
CMI Only
Non CMI
CMI & PSB
Control

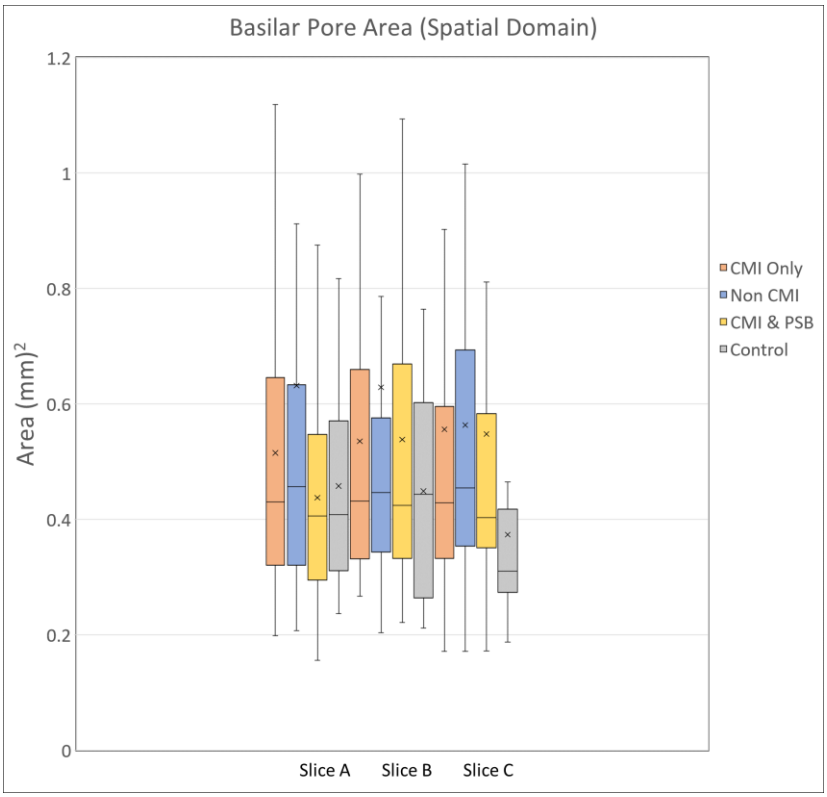
Basilar Pore Area (Spatial Domain)
Area (mm)²
1.2
1
0.8
0.6
0.4
0.2
0
Slice A
Slice B
Slice C
CMI Only
Non CMI
CMI & PSB
Control

APPENDIX B.

Supplementary graphs for the data looking at specific fracture modalities.

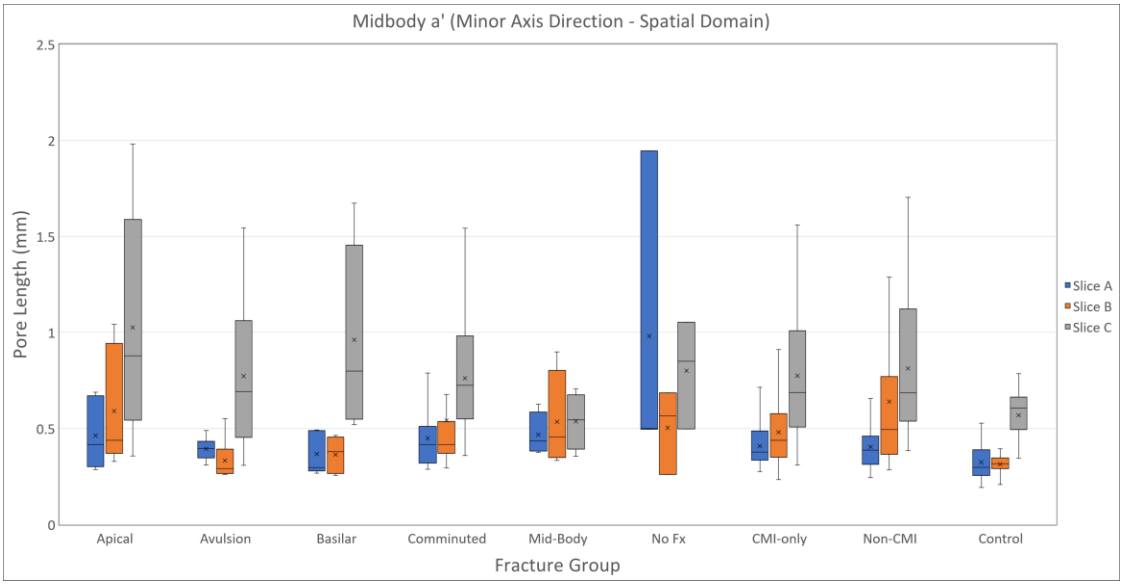

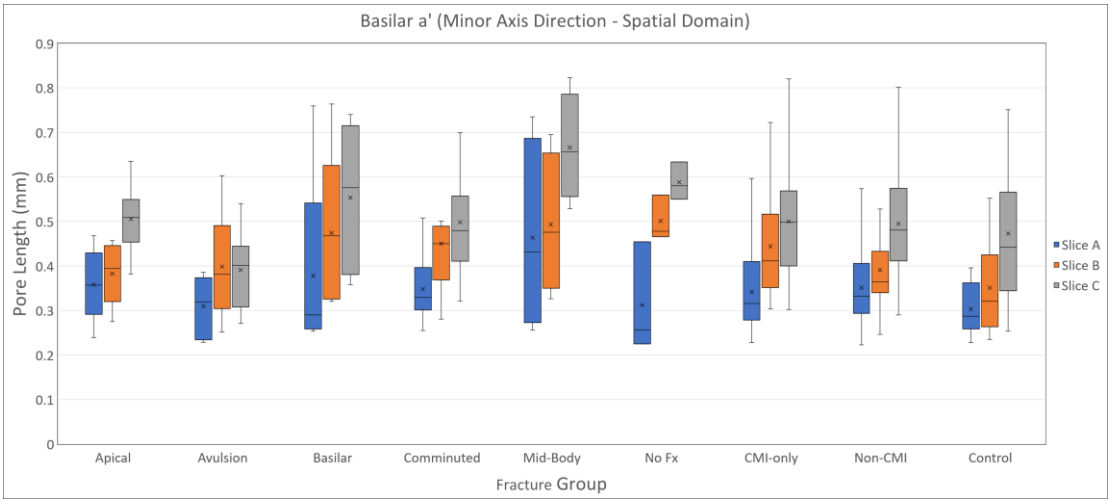

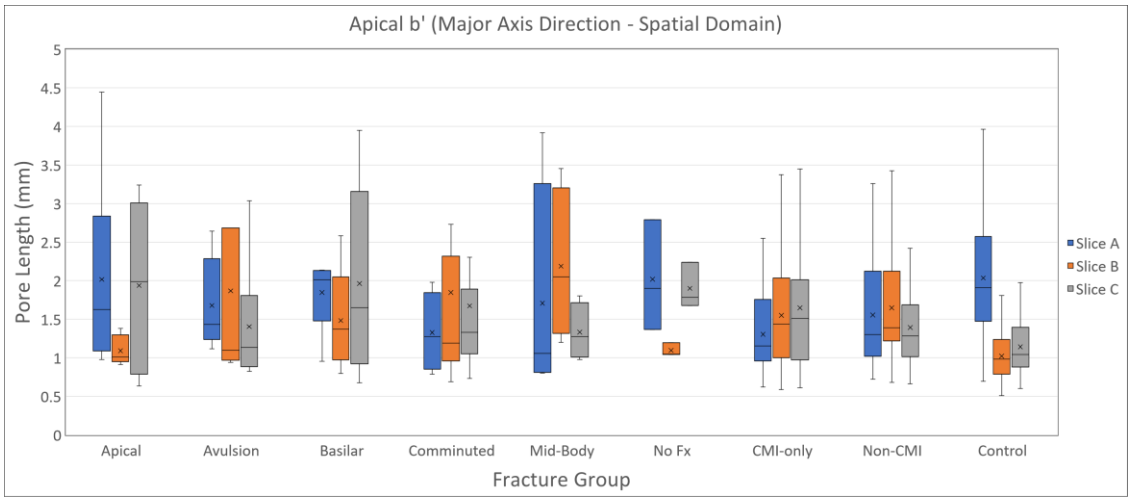
Apical b' (Major Axis Direction - Spatial Domain)
Pore Length (mm)
5
4.5
4
3.5
3
2.5
2
1.5
1
0.5
0
Apical
Avulsion
Basilar
Comminuted
Mid-Body
No Fx
CMI-only
Non-CMI
Control
Fracture Group
Slice A
Slice B
Slice C

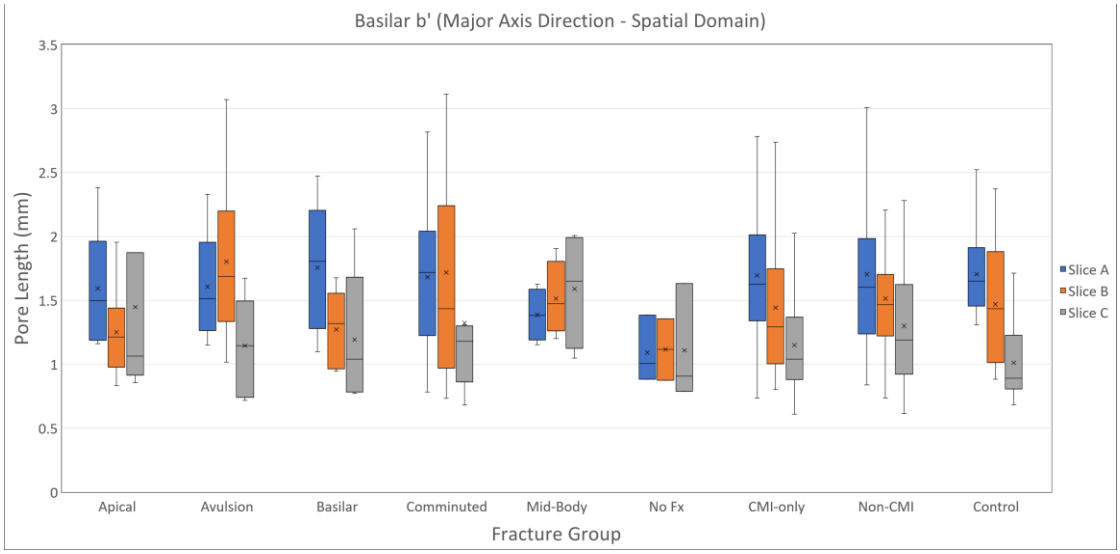
Basilar b' (Major Axis Direction - Spatial Domain)
Pore Length (mm)
3.5
3
2.5
2
1.5
1
0.5
0
Apical
Avulsion
Basilar
Comminuted
Mid-Body
No Fx
CMI-only
Non-CMI
Control
Fracture Group
Slice A
Slice B
Slice C

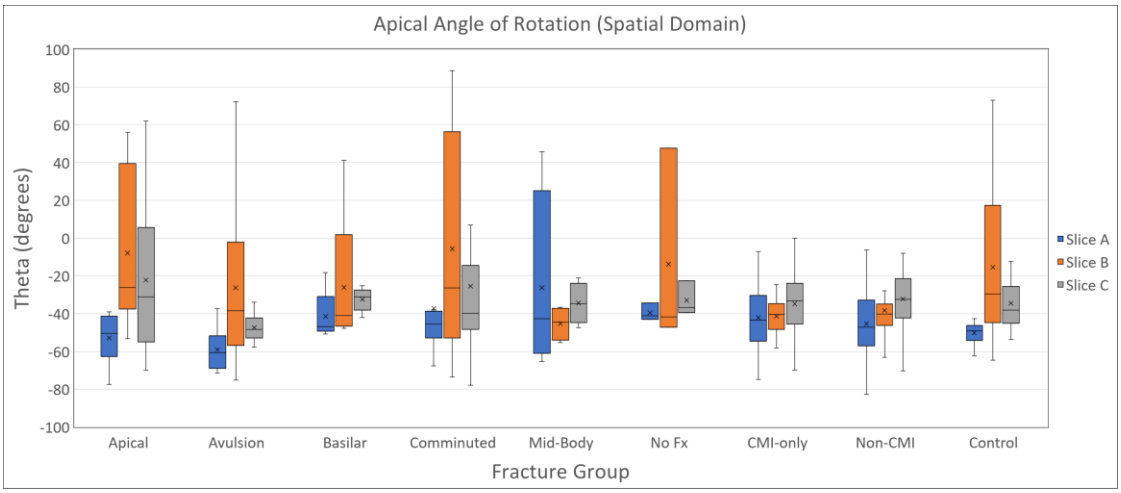
Apical Angle of Rotation (Spatial Domain)
Theta (degrees)
100
80
60
40
20
0
-20
-40
-60
-80
-100
Apical
Avulsion
Basilar
Comminuted
Mid-Body
No Fx
CMI-only
Non-CMI
Control
Fracture Group
Slice A
Slice B
Slice C

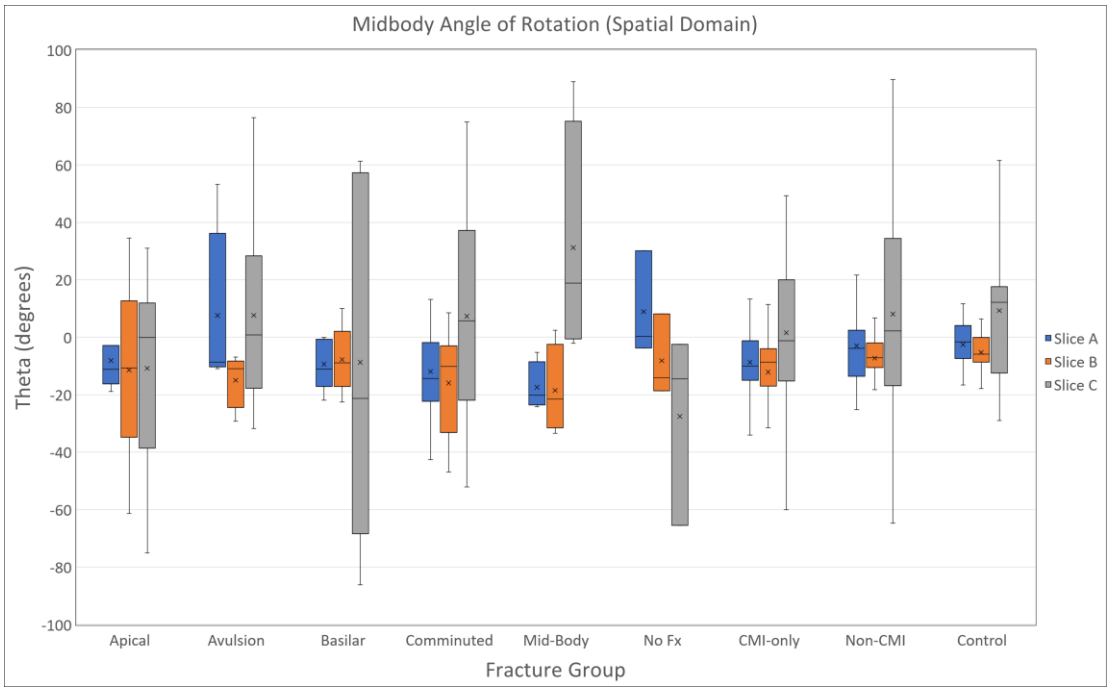
Midbody Angle of Rotation (Spatial Domain)
Theta (degrees)
100
80
60
40
20
0
-20
-40
-60
-80
-100
Apical
Avulsion
Basilar
Comminuted
Mid-Body
No Fx
CMI-only
Non-CMI
Control
Fracture Group
Slice A
Slice B
Slice C

APPENDIX C.

Updated Micro Ct Protocol

This is an updated version based on the Micro CT protocol, including 3D modelling and STL exporting (with pictures).

This panel is located at the bottom left corner and is referenced several times during the protocol.

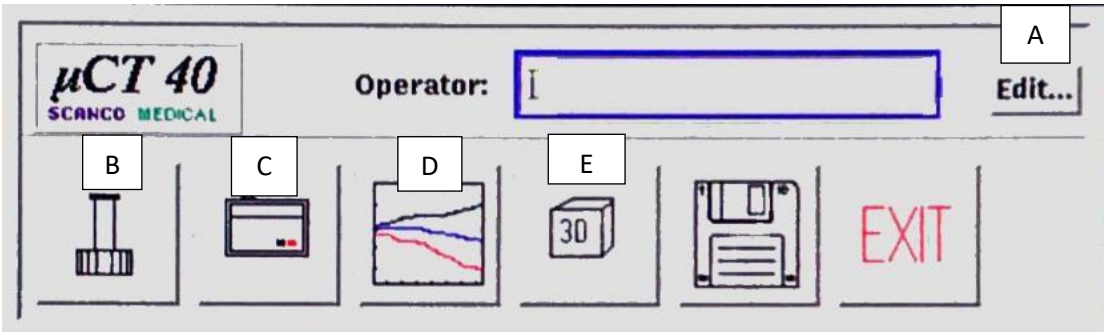

Figure 1 Control panel.

New user

- Click the edit button (A in Figure 1).
- Put user information (name…).
- Click on the save button and exit.
- Your name should appear in the operator window.

Loading sample and scanner.

Load your sample.

- Choose a tube to use taking note of the size of your sample (Use the smallest tube possible).
- Pack your sample with packing popcorn or floral foam to wrap the sample.
- Place the tube in holder inside the machine. Give the tube a small twist to ensure the notch on the end slips around the locking pin in the holder.

Figure 2 Sample

1)Naming sample:

- Click on B button in figure 1.

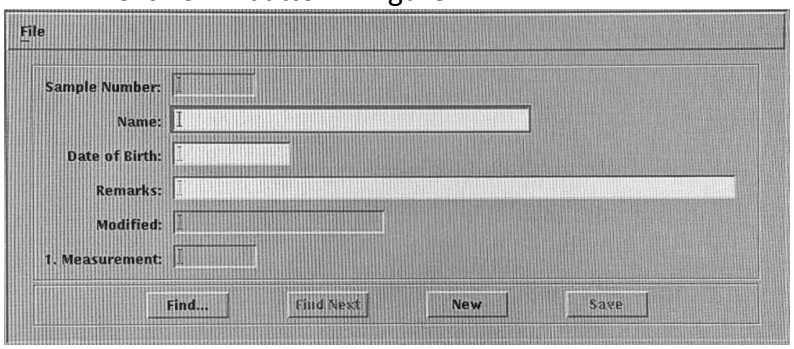

Figure 3 Naming the Sample

- Click on new

- This will be your measurement file name
- Give it an appropriate name and save

o Remember the number of the sample, you will need it later

- Exit after saving

2)Scanning

- Click on the C button in figure 1.

This window will show up

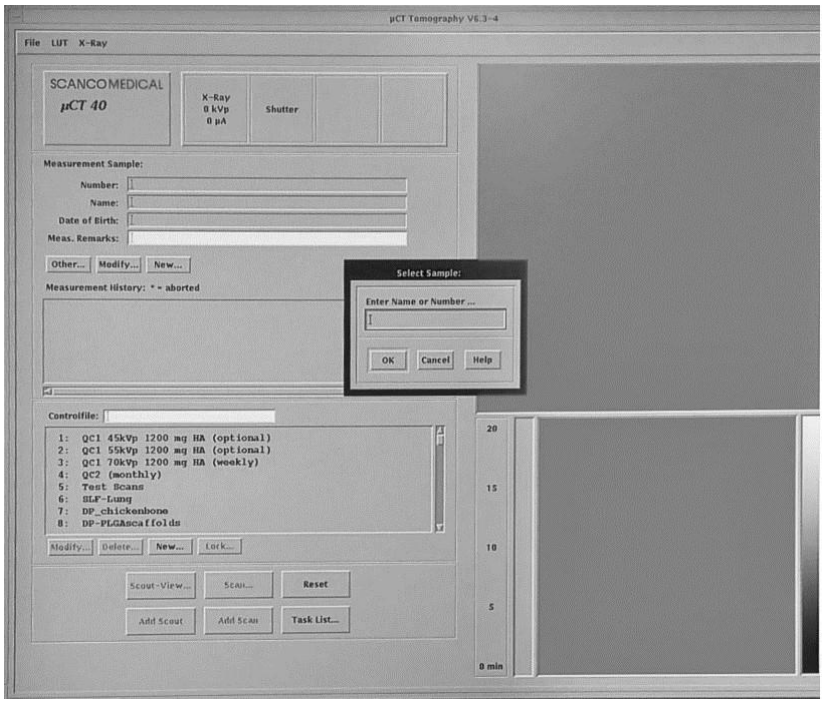

Figure 4 Tomography window

- Enter your sample number.
- Create a control file.
    - Click on new. A window will pop up with multiple parameters.

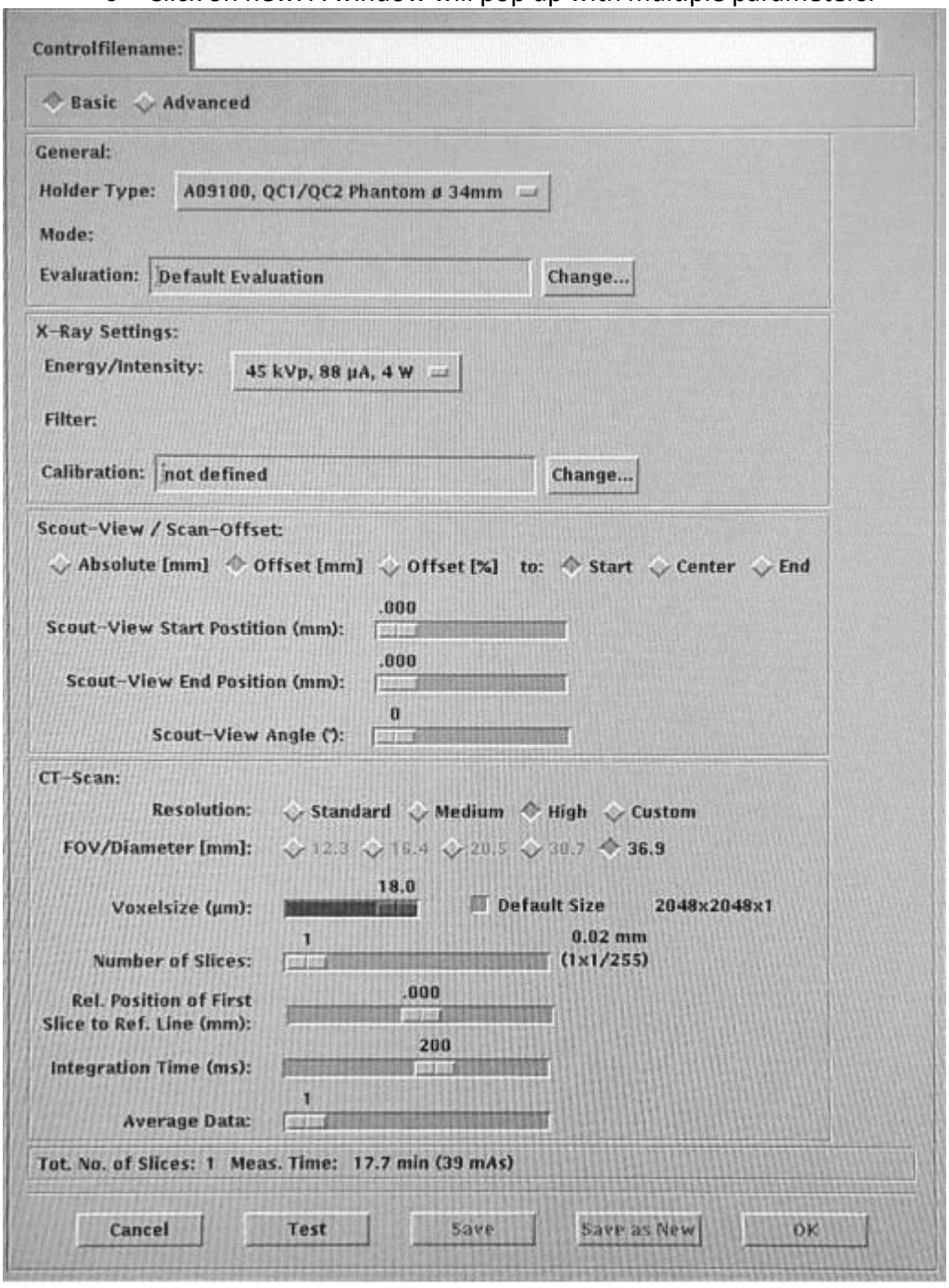

Figure 5 Control file settings

- Give the control file a name
- Holder type: Choose the diameter of the tube being used :12.3 mm is the smallest 36.9mm is the largest.

- Evaluation: For bone related studies. There are two (2) main ones
    - Bone Trab. Morphometry: It is the most detailed one. It includes Anisotropy, Mean density, 3D model, Triangular (plate model), bone volume, bone surface, trabecular measurements (thickness, number and spacing) and mean density.
    - BV/Density only Bone Eval: Will show you the bone volume, the 3D model, the complete volume (bone+ void) and the mean density

The first one takes a really time processing but its more detailed, so pick the evaluation that is more suited for your research.

- Energy intensity: You can pick the energy that is more suited for your sample, but errors could show up. The option "55kVp,72uA 4 W" works fine with most samples (Pick the highest option for dense materials)
- Resolution: Pick the one that is better suited for your investigation
- FOV/Diameter[mm]: Choose the diameter of your tube
- Click on Test, Save as New and OK.

- On the main tomography window (Figure 5) your control file should display at the bottom
- Next click Scout View and this window will pop up

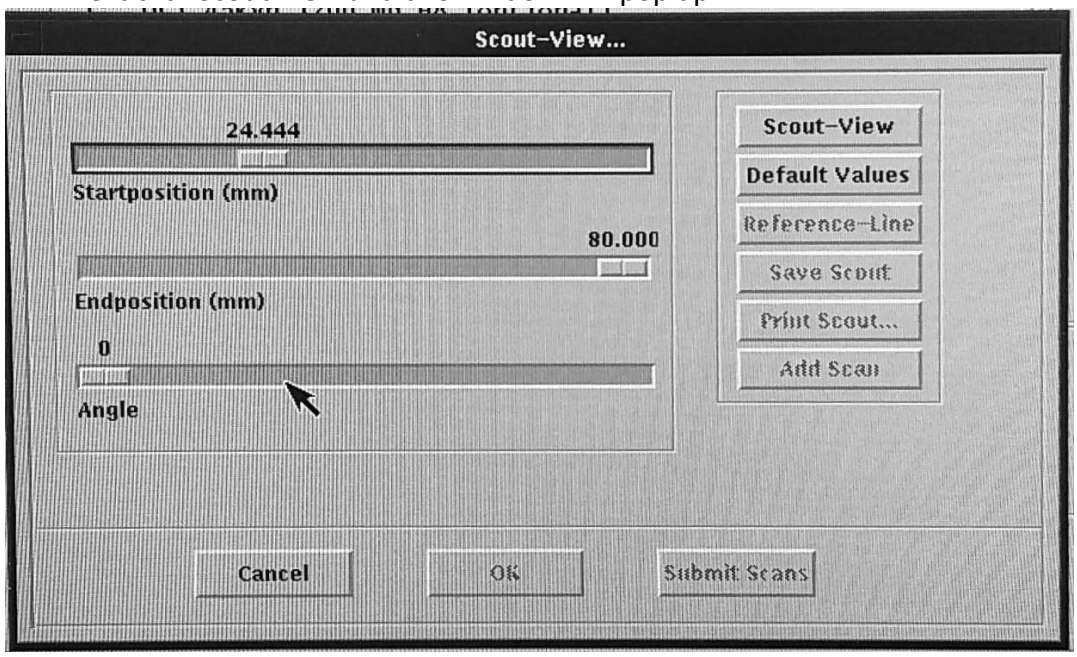

Figure 6 Scout-View window

- The Start position would the top of your tube, and the End Position the bottom.
    - If your sample is not that tall, you can adjust this accordingly and save time.

    - The Angle should be zero (0)
- Click on Scout-View
    - It will take a quick scan of the sample (it may take a couple of minutes)
- Once the scanning finishes an image of your sample will appear. Click on Reference Line

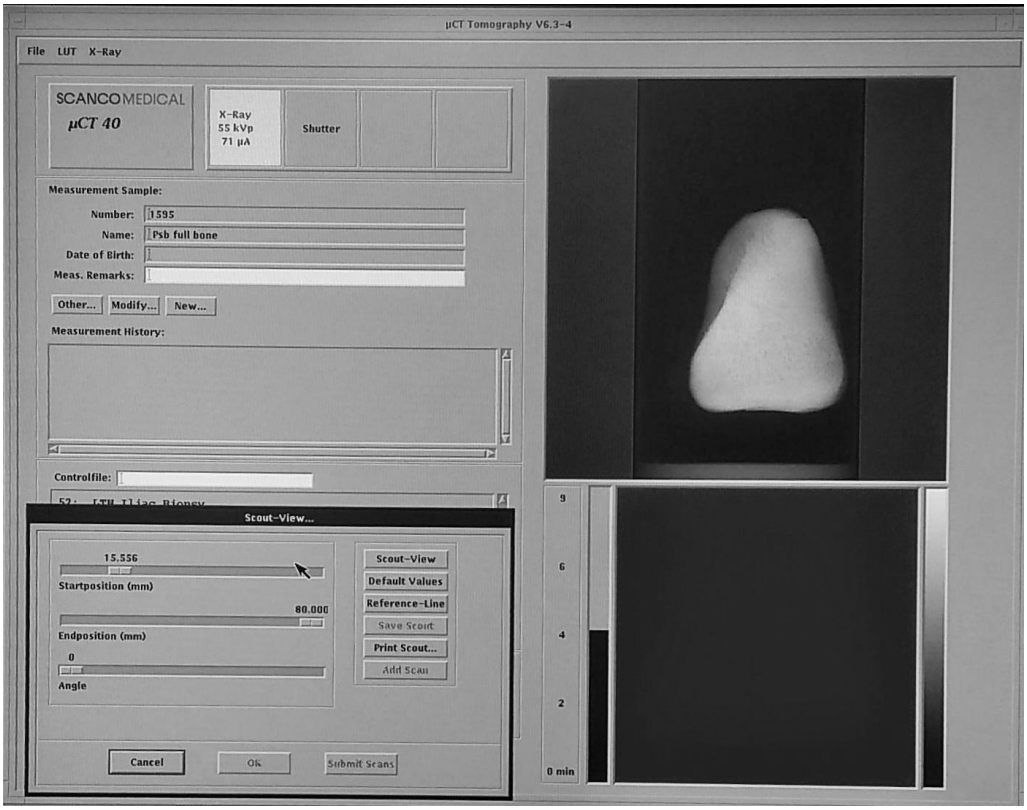

Figure 7 Scout-View Window after scanning

        - These lines represent the area that will be scanned, so the larger the box the long, the longer the scan will take.
    - Use mouse to move the green line up and down, and put it as close as possible to the top of your sample (without clicking)

- 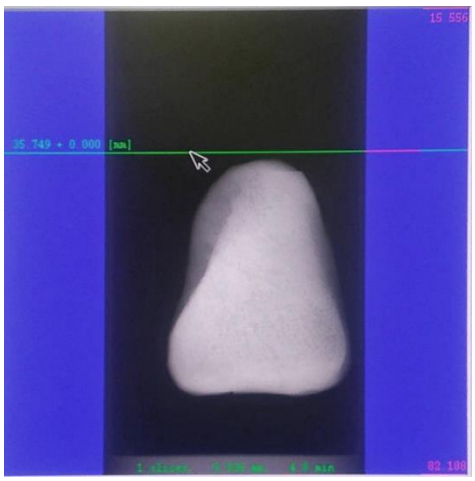

Figure 8 Scanned sample with top reference line

- Hold down the SHIFT key and move your mouse down to adjust the distance between the top and the bottom line.

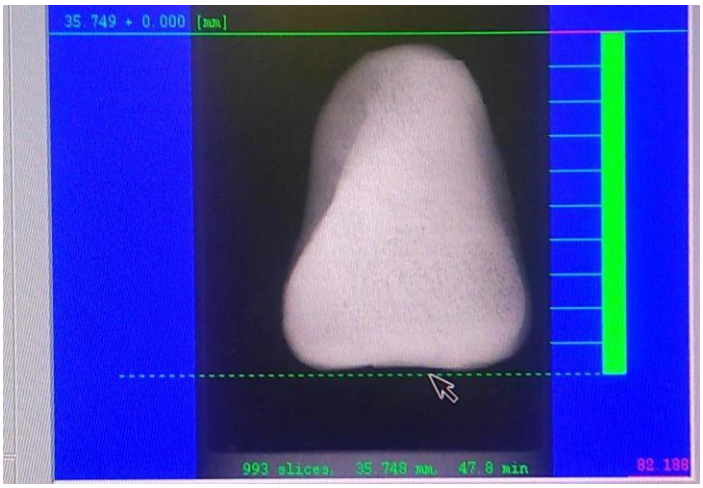

Figure 9 Scanned sample with both Reference lines

- You will be able to see the scanning time at the bottom of the window

- Release key to move both lines together and click to set them in place

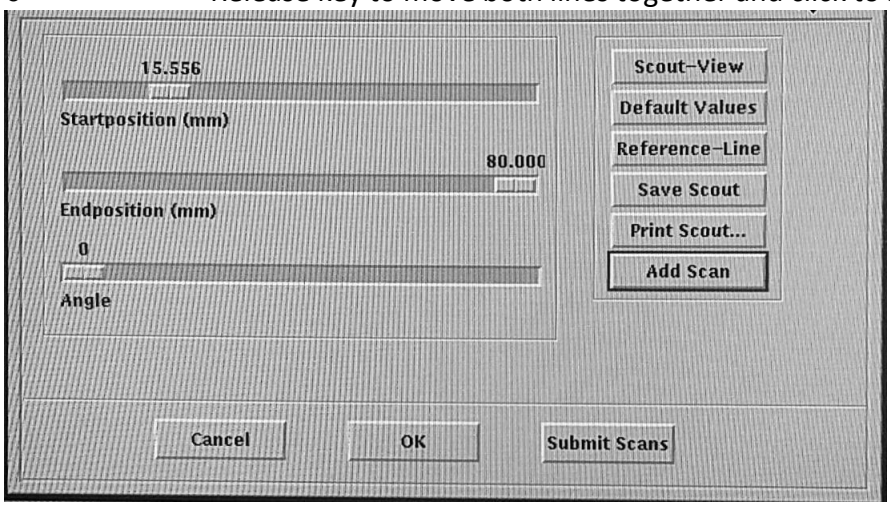

Figure 10 Scout-View window

- Click on Add scan and later on Submit Scans.
- This process will take a while.

A few moments later a light will turn on the Micro Ct scan and it will not turn off until the scanning process finishes

Figure 11 Micro Ct Scanning

3) Viewing Images

- Click on the D button (Figure 1)
- In the secondary pop up, select your file or sample number by either typing in the # you recorded or by scrolling for the name.
- Click Ok
- Images will load

- The next step is contouring every image; this needs to be really accurate since it will be used to create the 3D model.
- Main drawing tools.

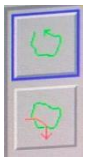

- Draw contour: This tool will contour your sample. Circle the image in the counterclockwise direction

- Correct: The contour to be corrected must be crossed at two places. The part lying in between these crossing points will be replaced by a new contour. (Counterclockwise direction).

- Delete object: Deletes one contour of the current image.
- Delete all objects: Deletes all the contours of the current image.
- Delete objects of all images: Deletes all contours of all images.

Contouring the images

- Choose the slice where you want to draw a contour by clicking on the appropriate picture
- Click on the draw contour tool, press the left mouse button, and drag it around your picture closely. Complete a circle for the contour to appear. (Counter clock-wise)

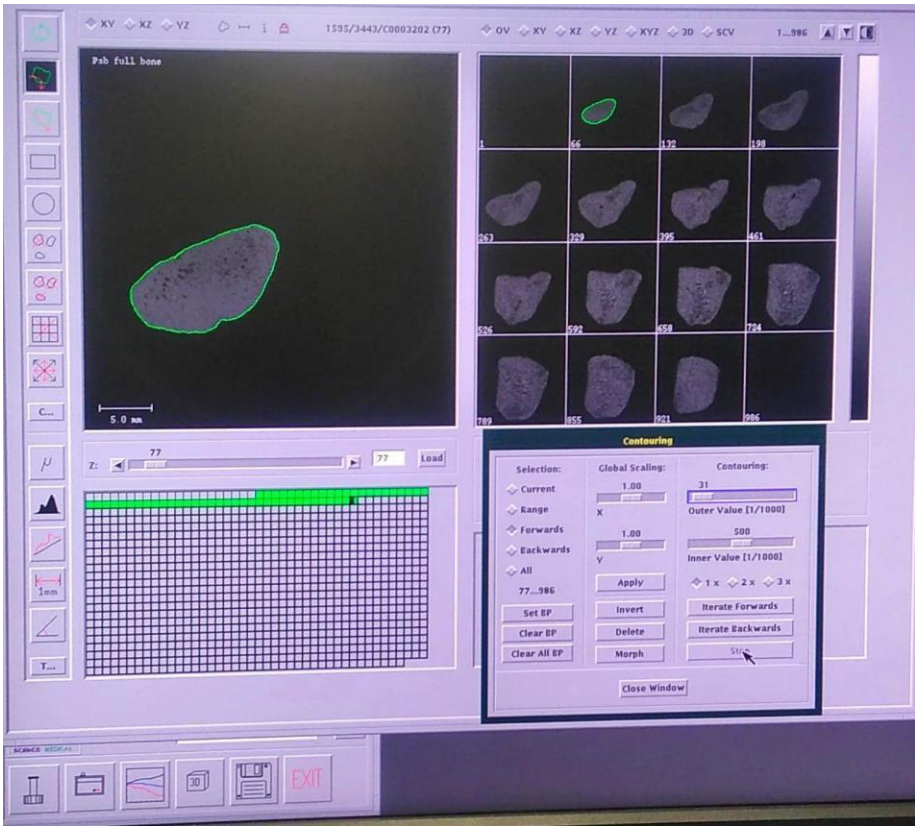

Figure 12 Images Window

- Double click the left mouse button and a secondary pop up will appear

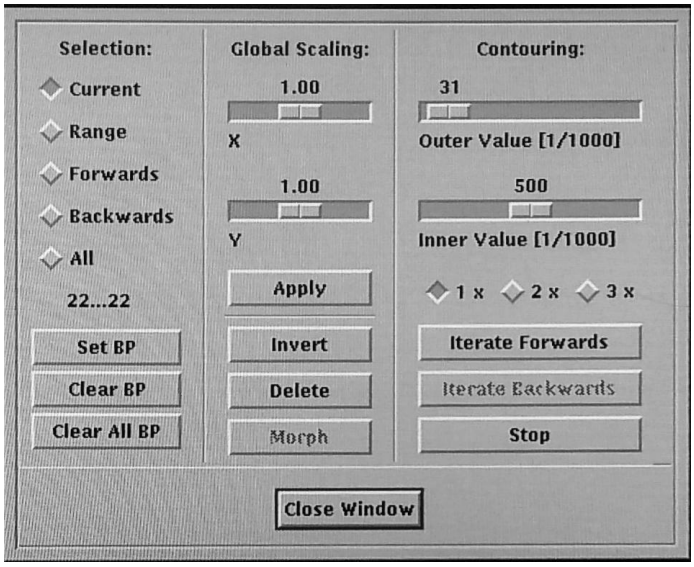

Figure 13 Contouring window

- This window will let you contour all the images faster.
- Double click the left mouse again and the circle you drew before will automatically adapt to your image.
- In figure 13, click on the forwards button and iterate forwards. This will let you contour images fast and the contour will automatically adapt to most of the pictures.
- You need to keep an eye of every picture to verify that the contour is accurate. If the contouring shifts in an odd shape, click stop. Use the Correct tool, double click on t h e left mouse button and it will adapt to the new shape.
- If they are several images with odd contour shapes, just go to the first odd picture and click on delete. It will remove all the contours from that slice forward.
- After you finish contouring all your images. Go to the tasks menu and click on 3D evaluation.

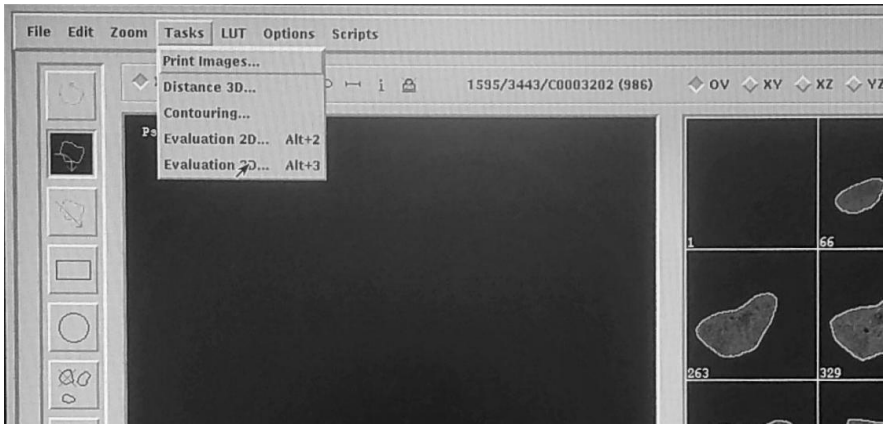

Figure 14 Tasks Menu

- This window will pop up

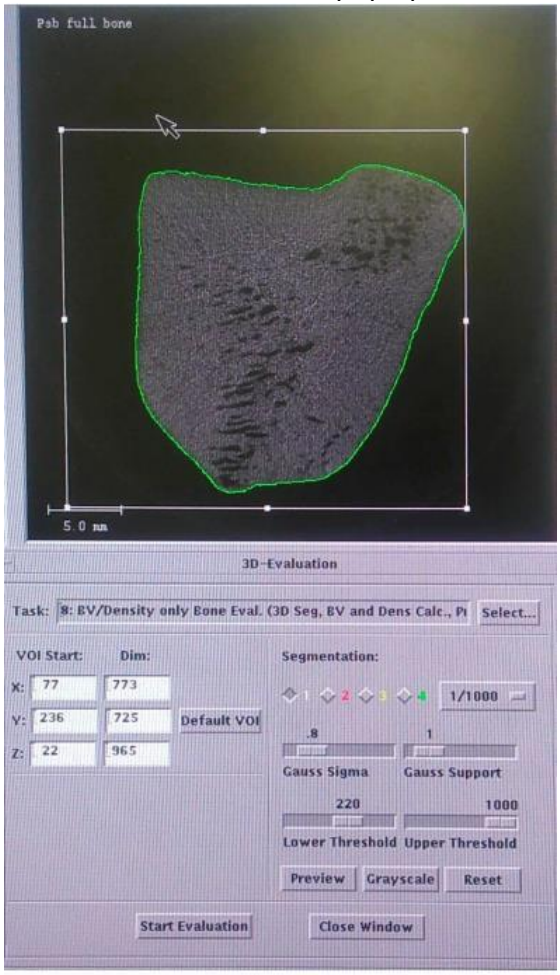

Figure 15 3D Evaluation window

- In the task section, Select your preferred evaluation.
- Choose a slice of the scanned images where you can clearly see the voids and internal structure of the sample.

- Zoom-in the sample and modify the lower threshold so that the black portion of the image would be void, and the white part is the material of the sample.

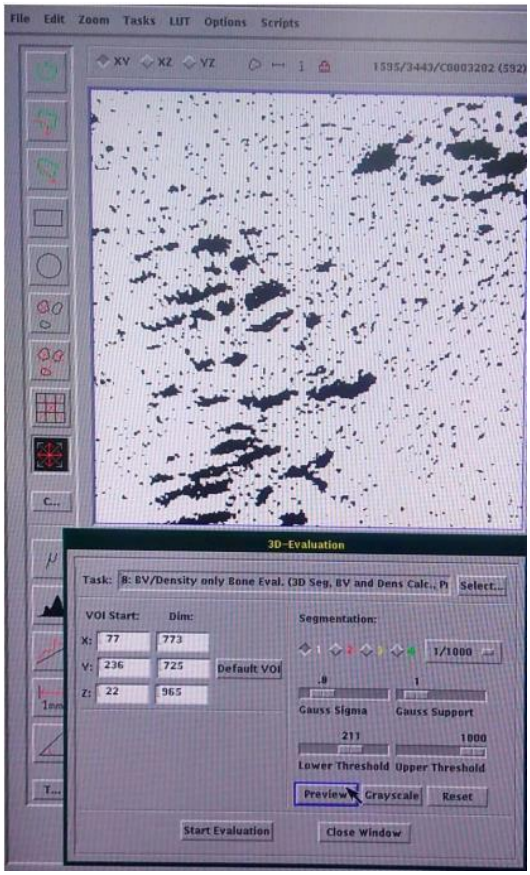

Figure 16 Threshold modification on the zoomed-in image

- Go back and forth between the grayscale and preview button, to ensure an accurate selection of void/material.
- Click Start evaluation and wait until the process is completed (this may take a few hours depending on the type of evaluation chosen).

3.1 Creating DICOM images

- Click on the 3D-Evaluation button under the task tab again. For the specific task, choose number 13

- Convert to DICOM
-For the minimum value for the VOI select one (1)
-For the maximum value for the VOI, select 1024 for X & Y and select the number of the last slice for Z
-Then click "start evaluation"

4) Finding your test Evaluation Results and pictures

- Follow the protocol for using the "MicroCT FTP" work instructions

Downloading the DICOM files from the microCT machine

1. Open the “microctFTP” app on the computer. This app should be pinned to the taskbar at the bottom of the screen or can be found by searching “microctFTP” in the windows search bar

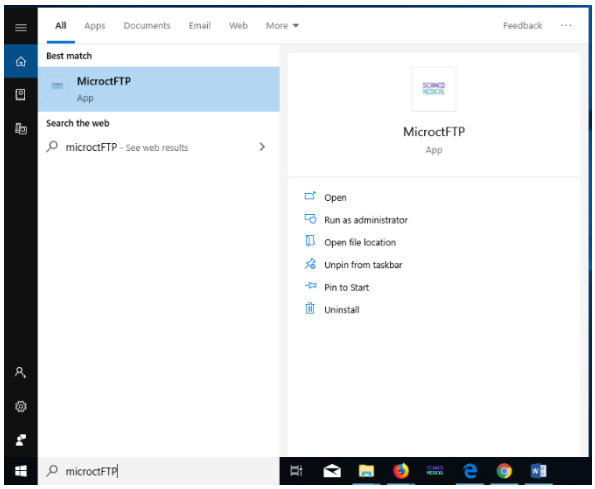

2. Once the app is open, click the “FTP connection” tab
   Fill out the information as follows:
   (contact lab PI for login credentials)

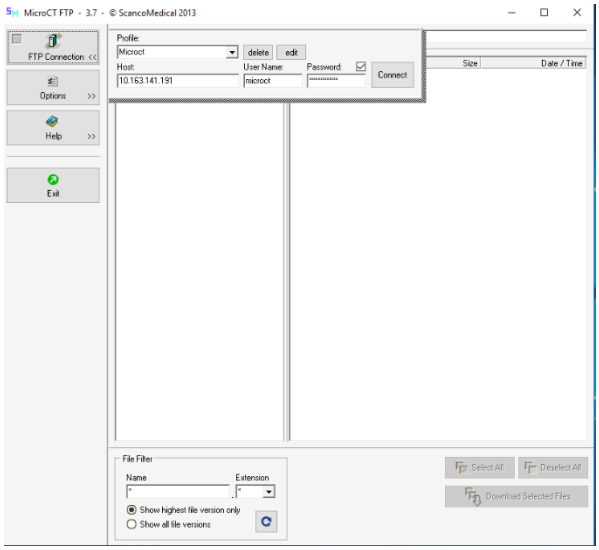

3. Click “Connect”

4. Your data should be located under the “MicroCT:Data” tab. Click this tab and then scroll all the way to the bottom and click on the last folder (right above the “MicroCT:Scratch” folder)

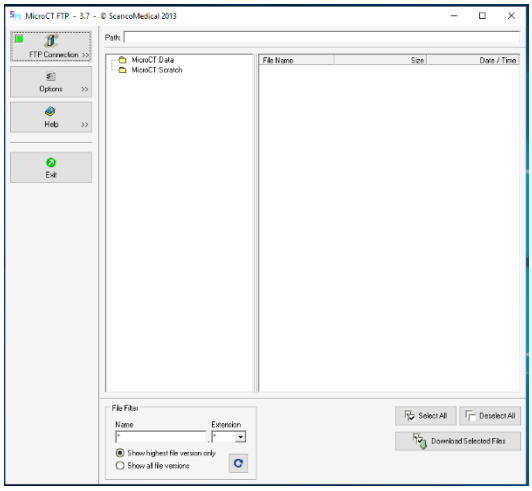

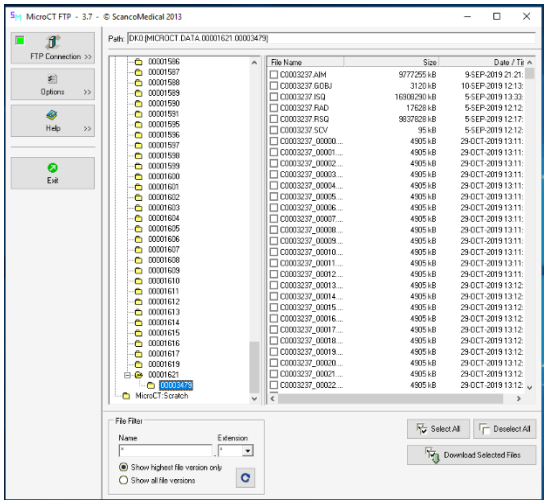

5. In the “Extension” drop down box, type in “DCM” and the click the refresh arrow (this will make sure only the DICOM files are being shown)

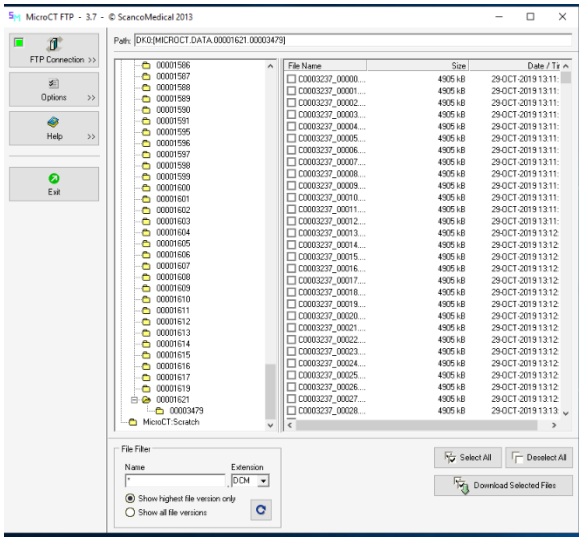

6. Click on the “Select All” button

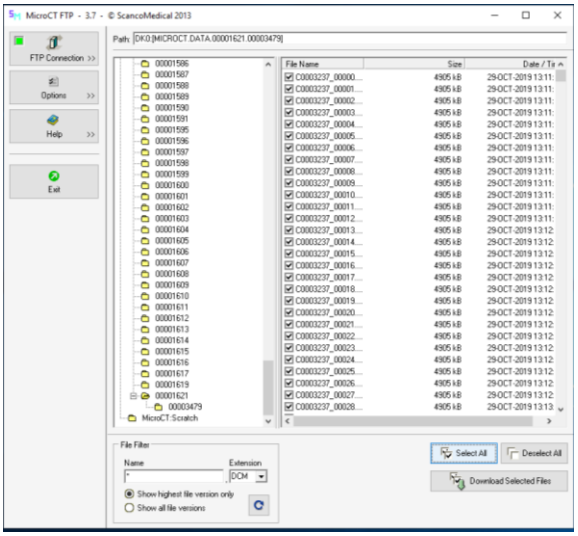

7. Click on the “Download Selected Files” button. A pop-up window will then appear. Select the folder in which you want the DICOM files to populate and be stored, and then click “OK”.

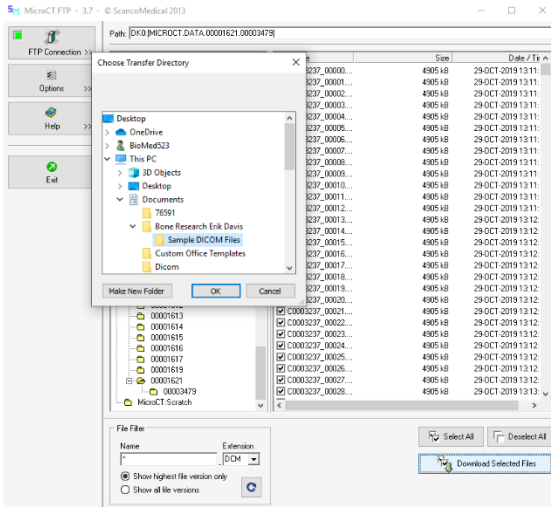
MicroCT FTP - 3.7 - © ScancoMedical 2013
FTP Connection
Options
Help
Exit
Path: [DK:0.[MICROCT.DATA.00001621.00003479]
Choose Transfer Directory
Desktop
OneDrive
BioMed523
This PC
3D Objects
Desktop
Documents
76591
Bone Research Erik Davis
Sample DICOM Files
Custom Office Templates
Dicom
Make New Folder
OK
Cancel
00001613
00001614
00001615
00001616
00001617
00001619
00001621
00003479
MicroCT Scratch
Size
Date / Ti
4905 kB
29-OCT-2019 13:11:
29-OCT-2019 13:12:
File Filter
Name
Extension
DCM
Show highest file version only
Show all file versions
Select All
Deselect All
Download Selected Files

Creating Sagittal Slices Using SimpleWare

1. Open the SimpleWare Application

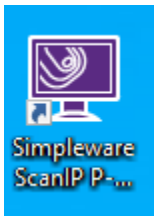

2. On the left-hand side of the screen under the “New Project From” tab, select DICOM images

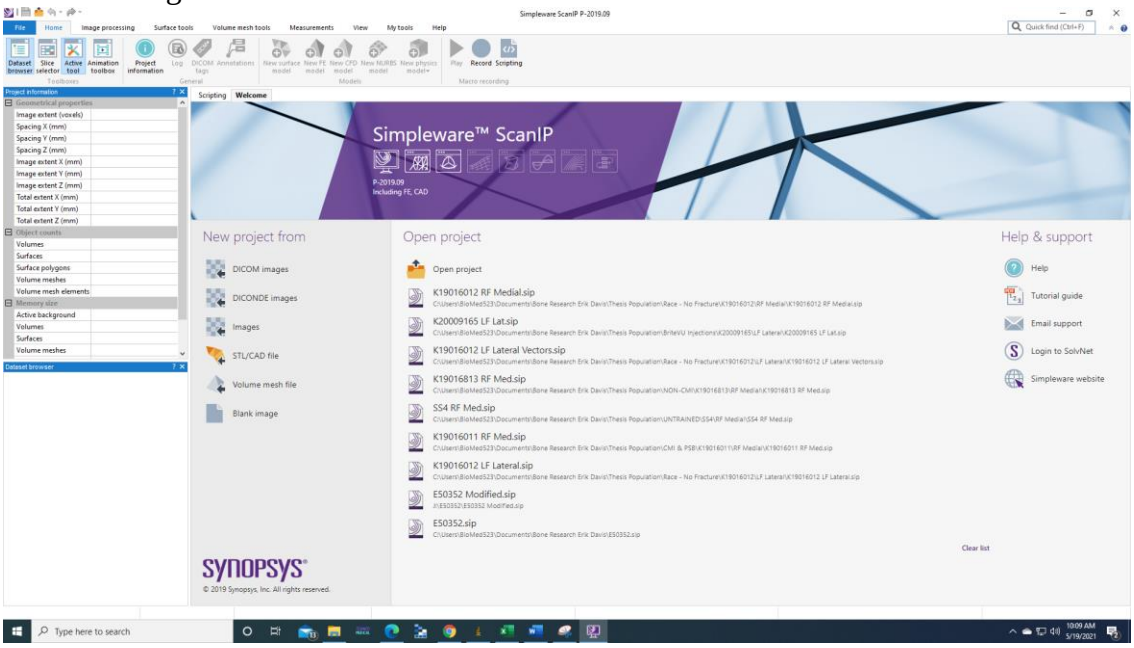

3. On the new pop-up window click “Scan Folder” in the upper-right hand corner

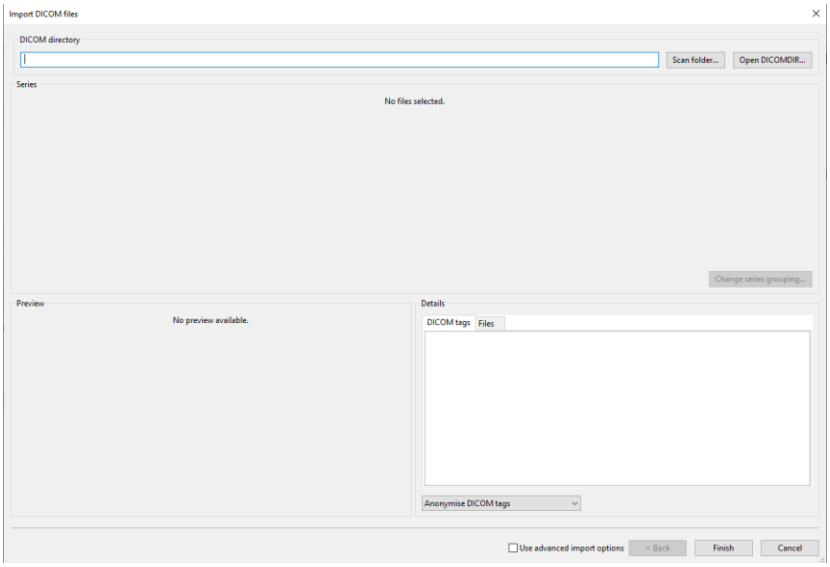

4. On the file explorer, find the **folder** you wish you upload and click “Select Folder”

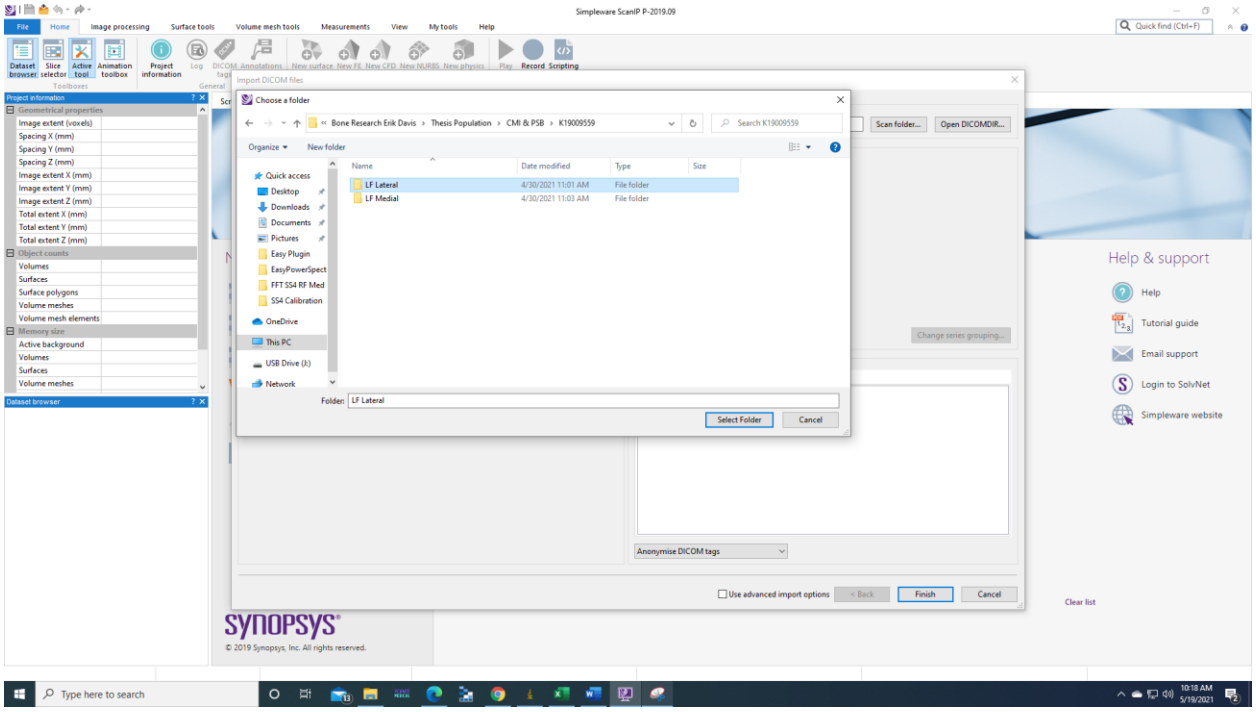

5. Then click “Finish”

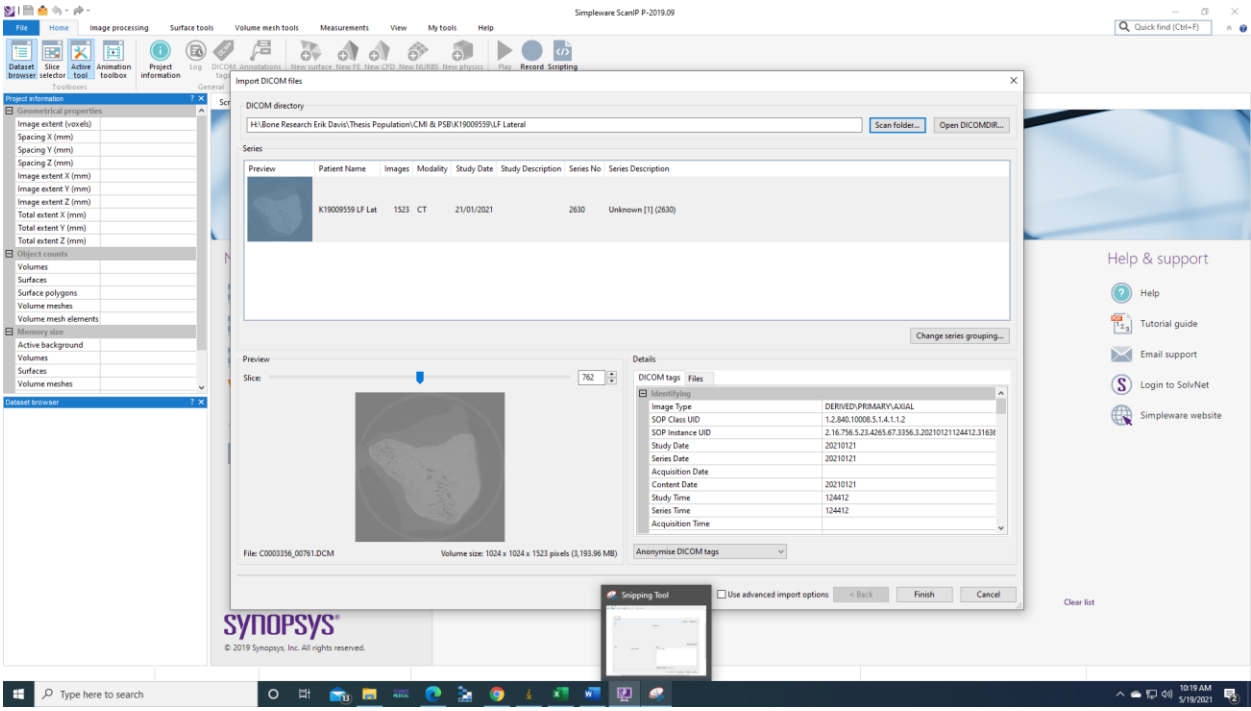

6. You will now see three (3) different panes with the three different orientations of the bone. The three sliders above the panes let you slide freely through the slices in that orientation

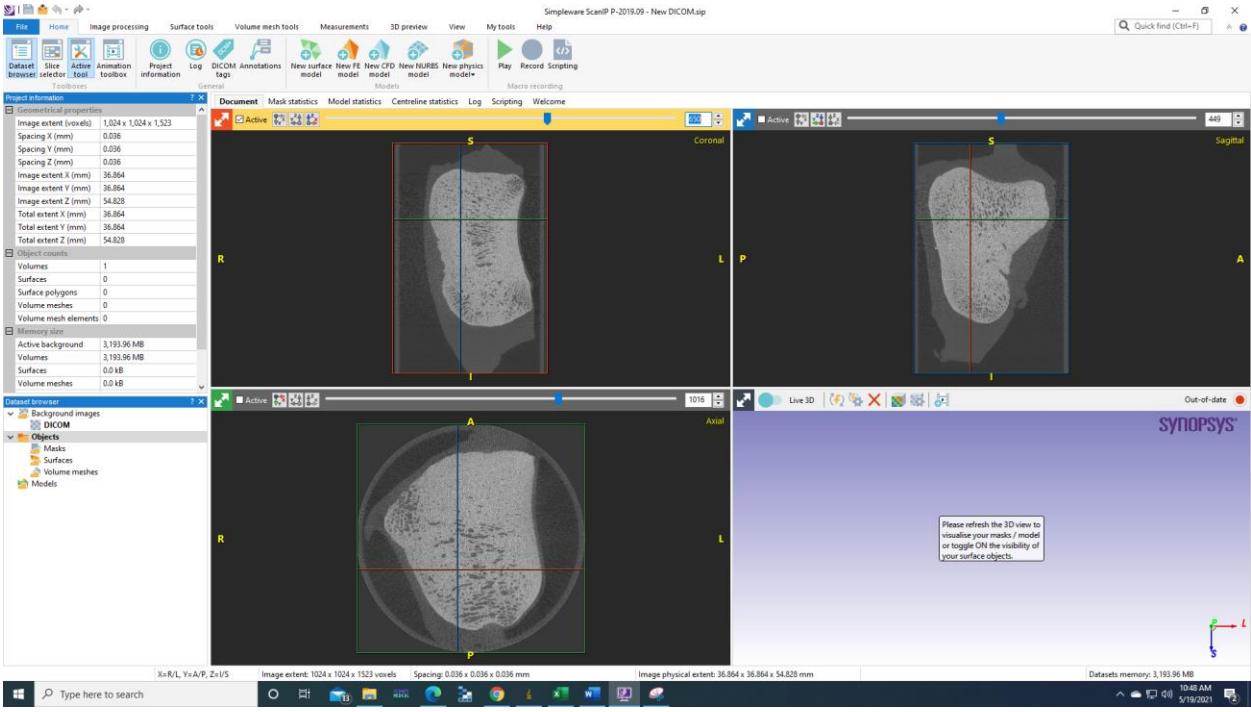

7. For standardization purposes, the bone needs to be oriented in the same position for exporting. This will ensure that the slices are from the same viewing angle and can be more accurately compared across the different populations of horses. The axial view will need to be rotated so that the frame looks like as shown below:

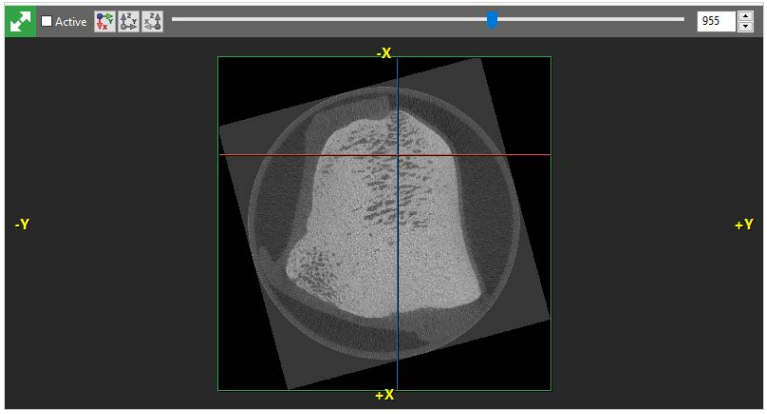

This rotation has the medial point of the bone pointing upwards on the screen in the -X direction.

The rotation can be done using the “Align” function under the “Image Processing” tab and changing the box in the far right to only rotate around the axial view.

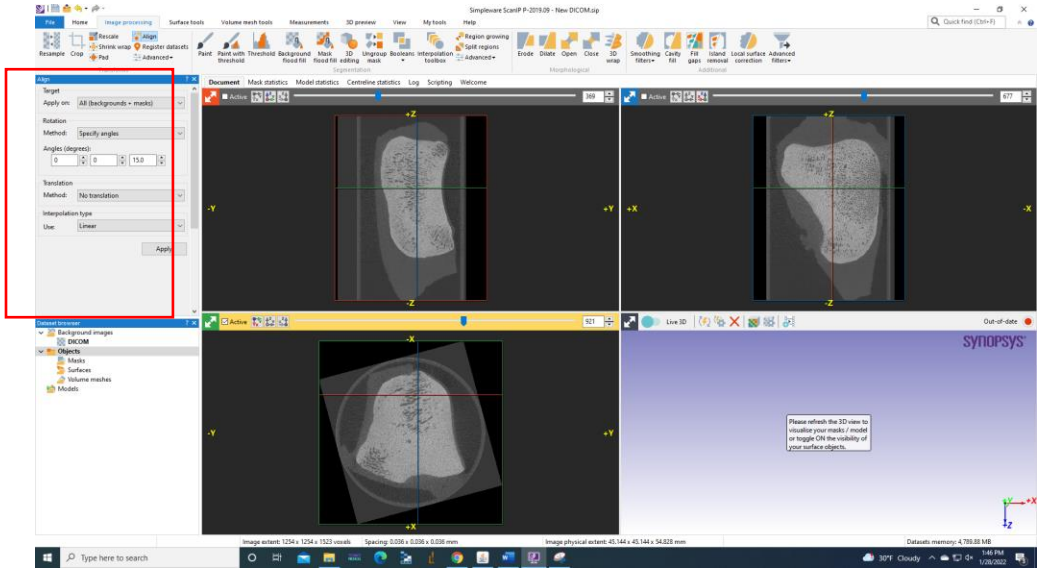

8. The top right pane is labeled “sagittal,” but depending on how the DICOM image is oriented in SimpleWare, it may not be oriented correctly.

(SimpleWare does not import the same way that the microCT machine exports, so sometimes there is a little bit of confusion in the orientation)

You will need to use the sliders to slide through the top panels to find slices that resemble:

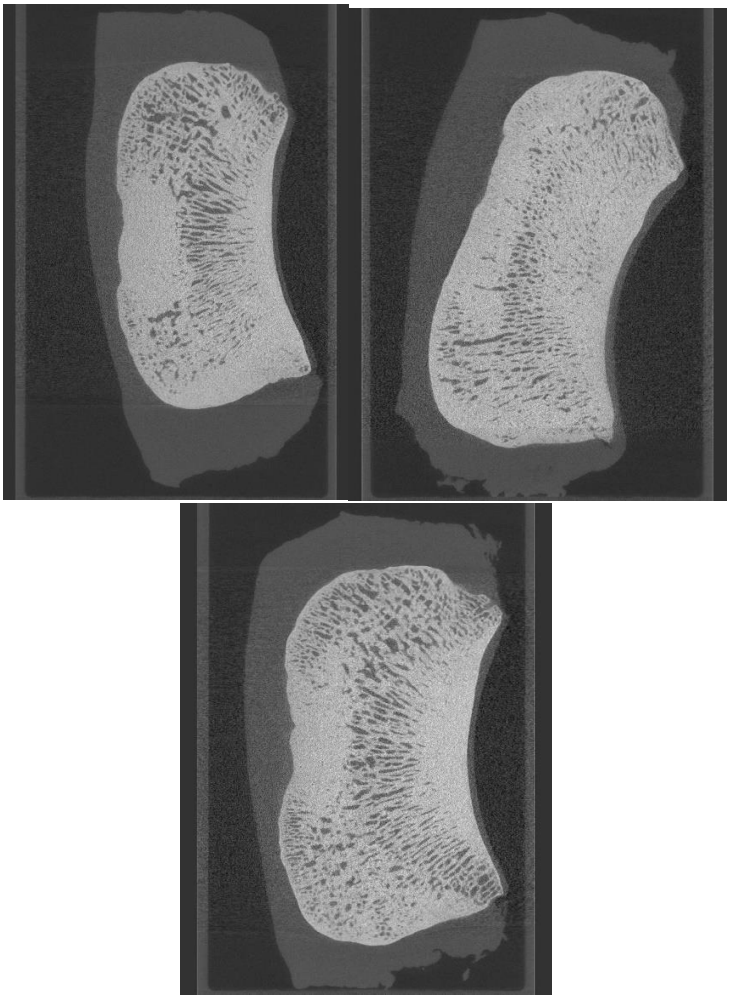

(These three pictures are all taken from different bones.)

9. Locate a slice you wish to export

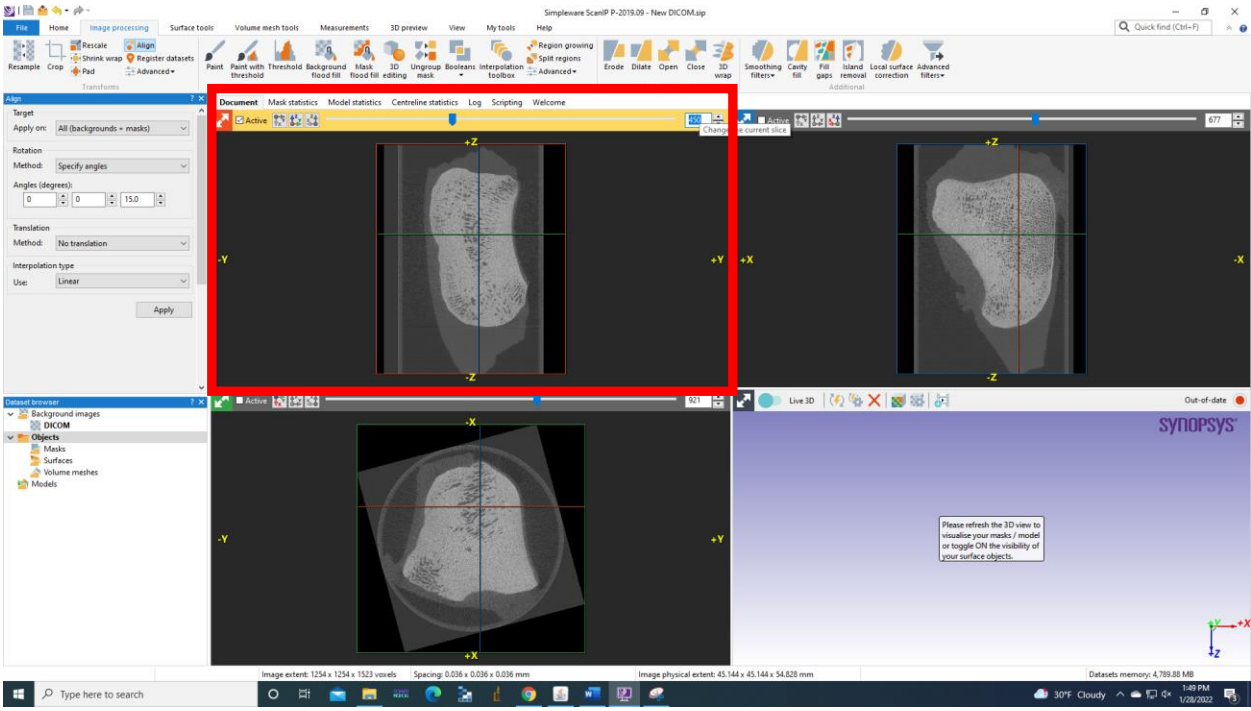

10. Mark the slice by going to the “Image Processing” tab and clicking the “Threshold” button. The thresholding levels are not that important because we are just using them to mark this slice and not using them to do any processing. If the levels are around the same as the one in the picture, then they will be fine. Make sure “Apply On” only has “Active Slice” listed, and make sure the “Active” box is checked for the slice that you want. Take note of the slice number as well (450 in this case).

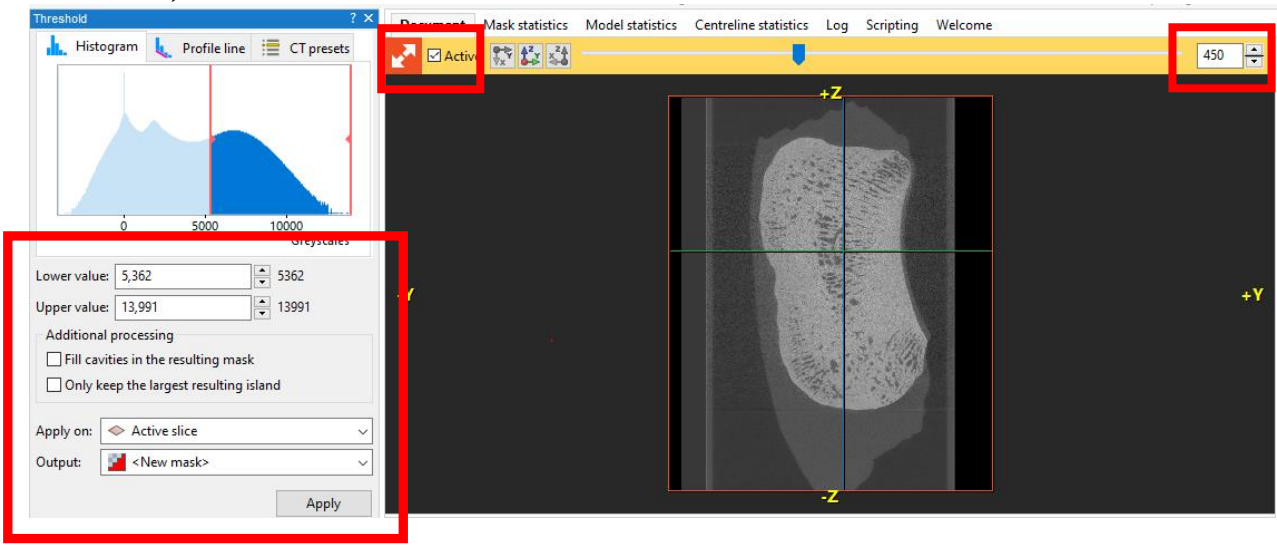

11. Click “Apply.”

The slice should now appear as red on the screen.

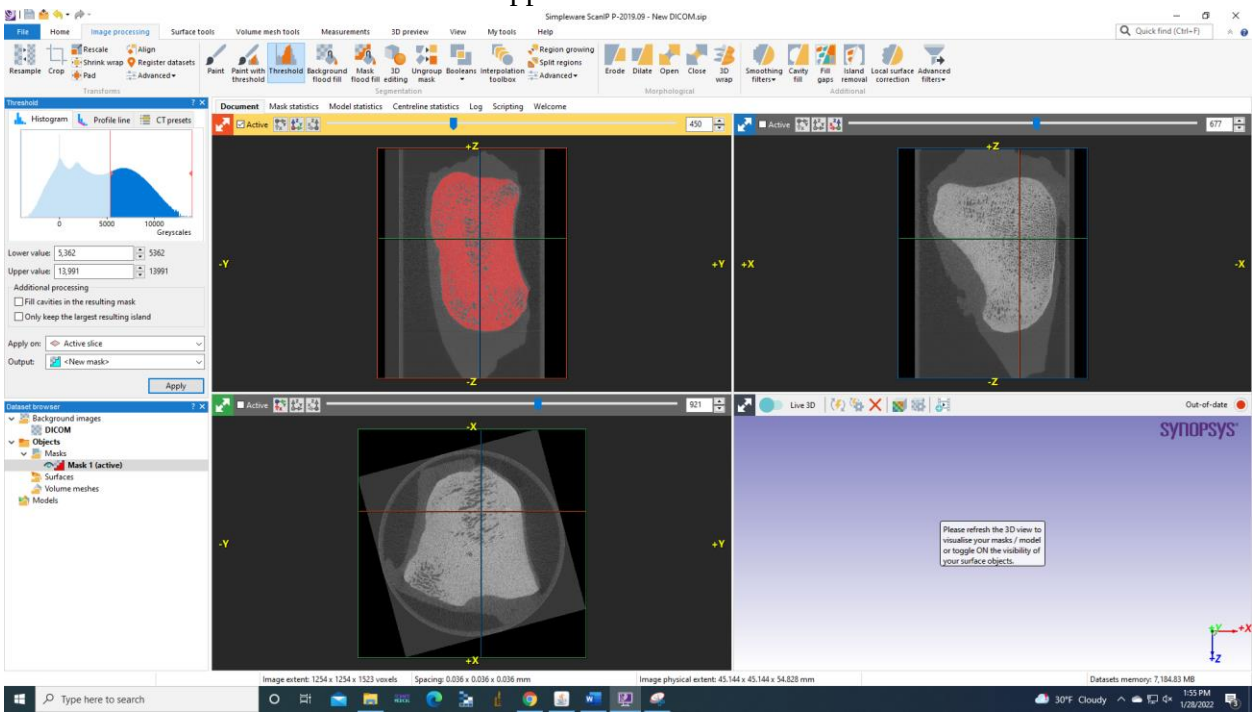

12. Now click the “Align” button under the “Image Processing” Tab.
    - If the slice you want is in the “Coronal” window (top left…. Like this example)

      Then enter “90” into the box in the middle and set the parameters to the ones shown in the box below.

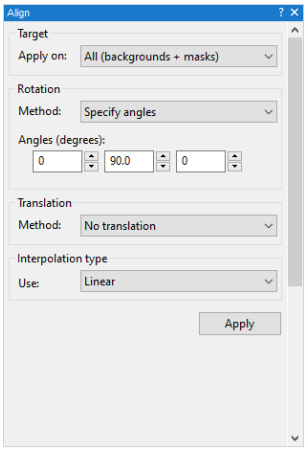

    - If slice you want is in the “Sagittal” window (top right) then enter “90” into the box on the far left under the degrees section

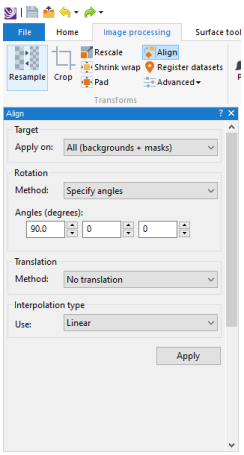

13. Click “Apply.” You should now see that the views have switched locations from earlier.

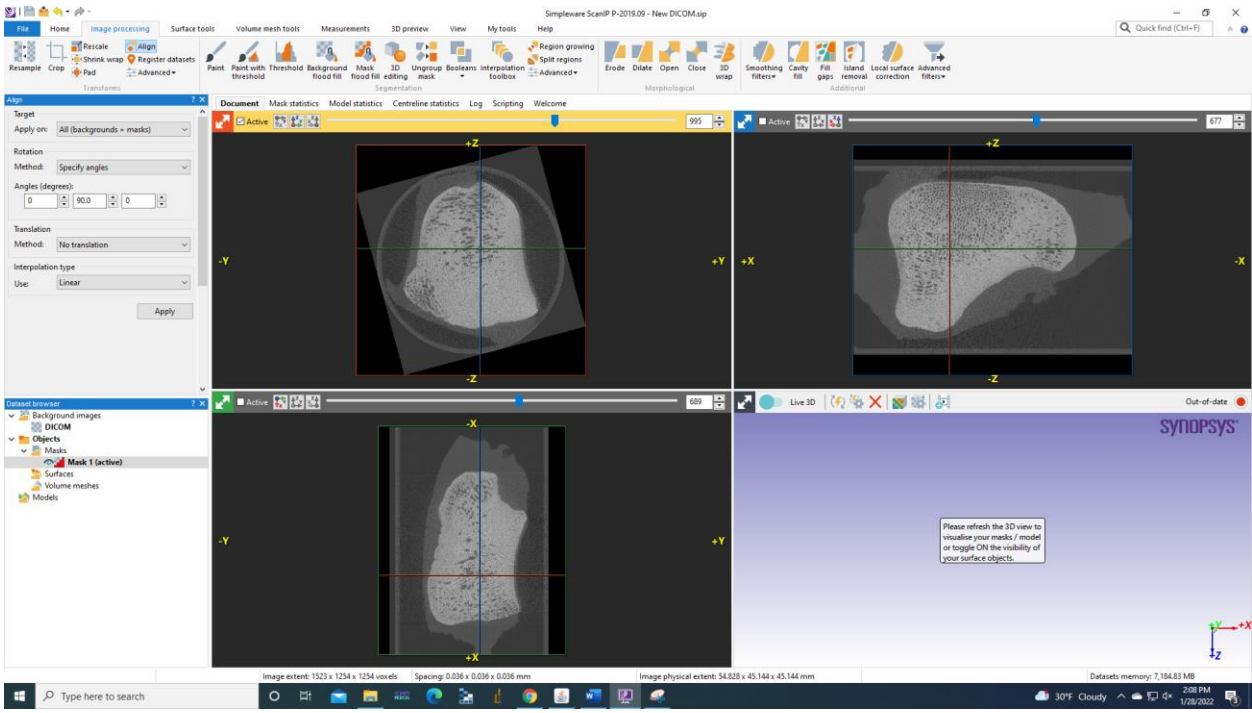

Now find the same slice number that you took note of earlier that you marked (in this case 450) and subtract it from the total number of slices in the set (in this case 1253) and find the resultant number in the bottom window (1253-450=803). If you see your red slice, then you correctly changed the orientation and are ready for export.

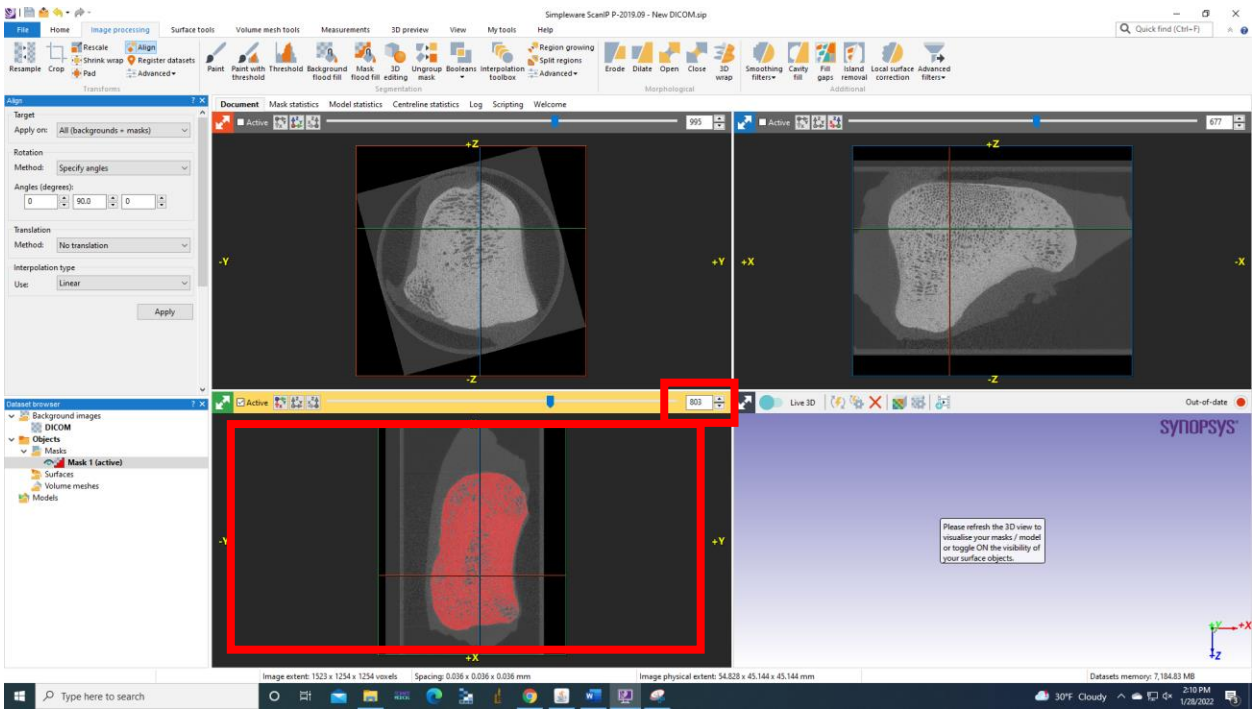

14. Click on the “File” tab and then “Export” -> “DICOM”

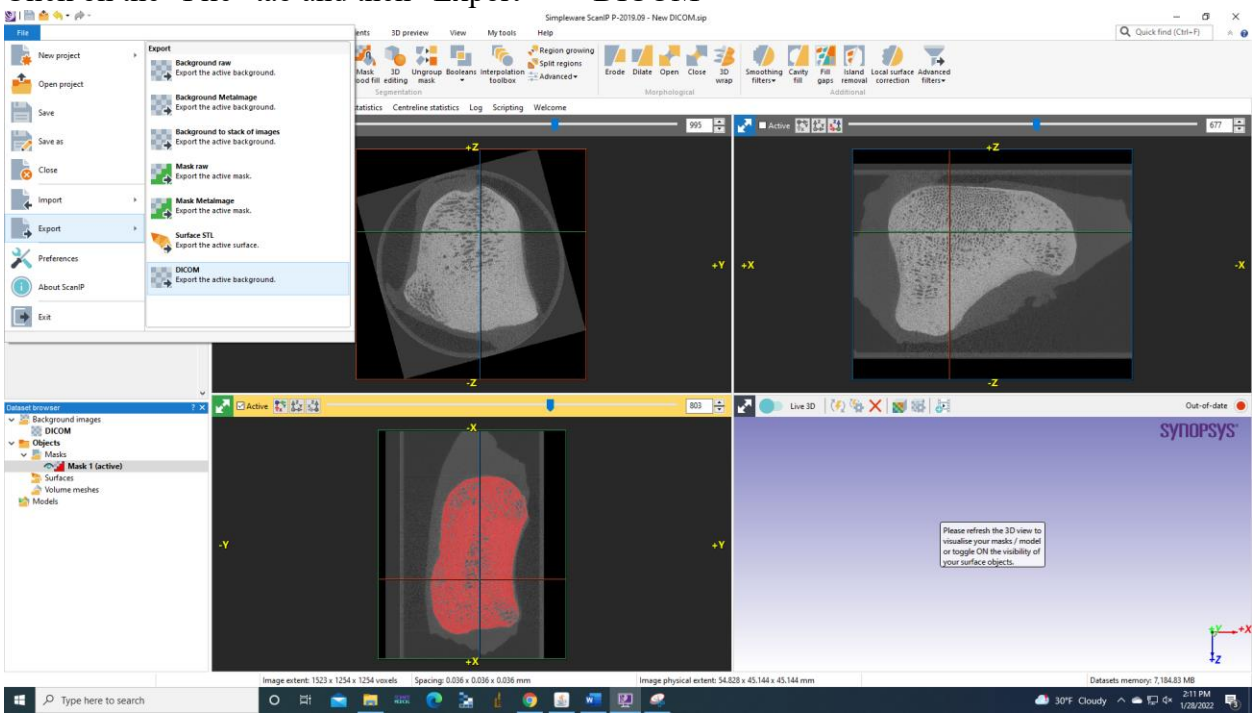

15. Under the “Z plane slices to export” section select “Range of Slices” and put the slice number (803) in both boxes on the right to only export the one slice.

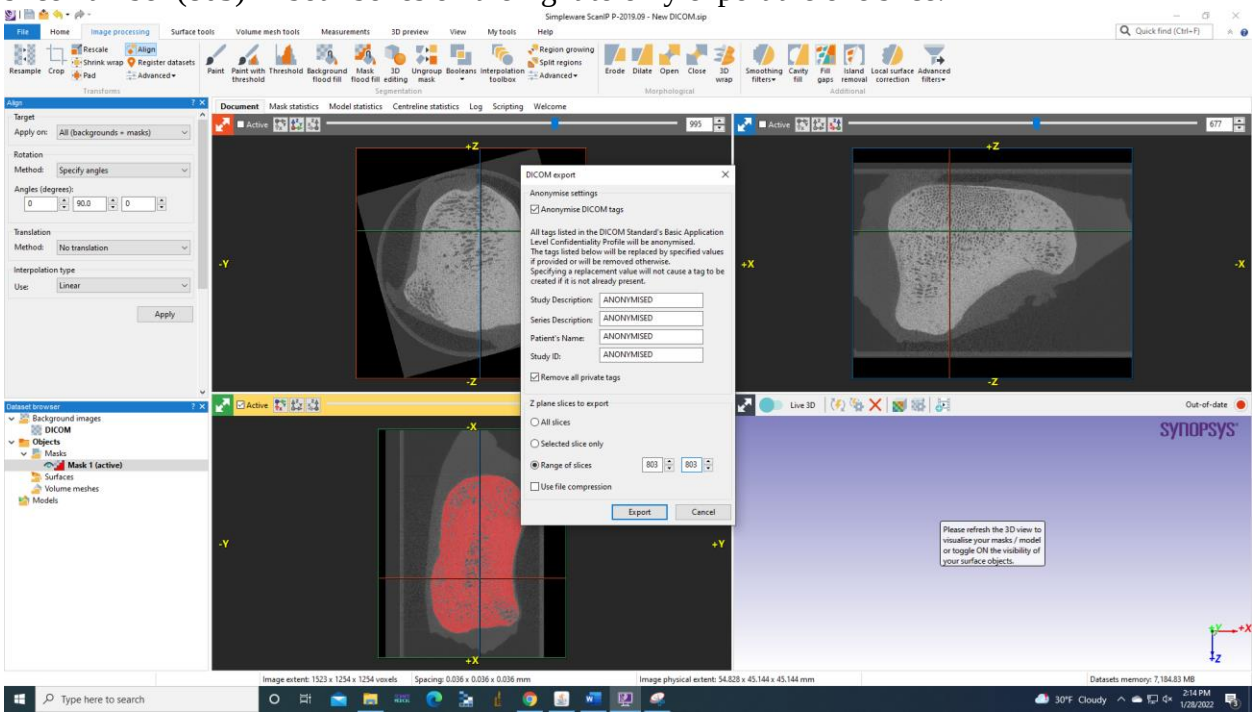

16. Finally, select where you want the exported DICOM slice to be stored.

Saving the Data Point for the Ellipses in ImageJ

1. Open the ImageJ software

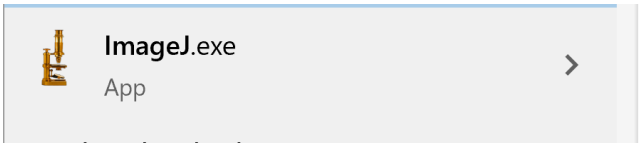

2. Click “File” and then “Open” and then select the image you wish to open

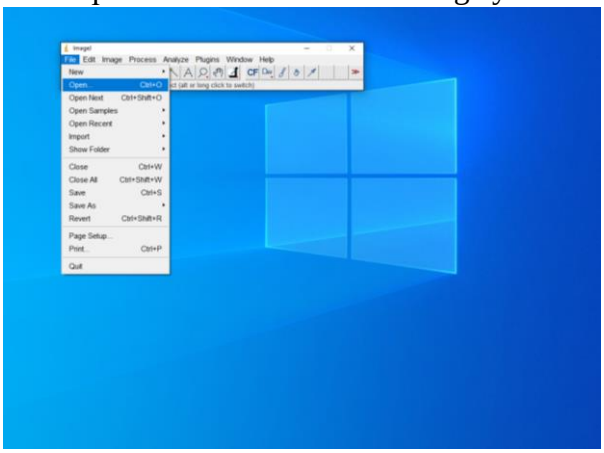

Use the “- “and “+” keys to either shrink on enlarge the Image

3. Once the image is loaded, create a rectangle selection using the tool on the far left of the top bar (it can be any size)

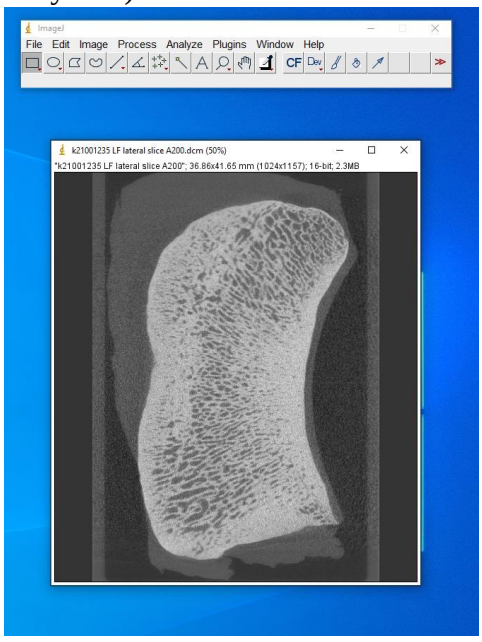

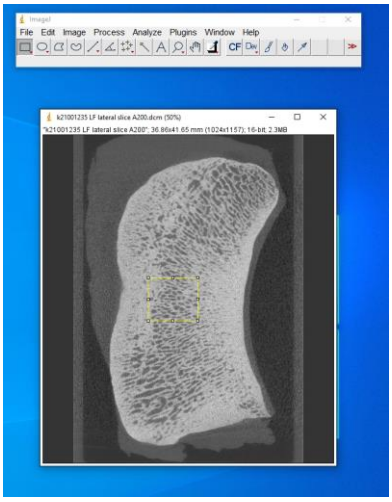

4. Next click on the “edit” tab and then move down to “selection” until it expands and then click “specify”

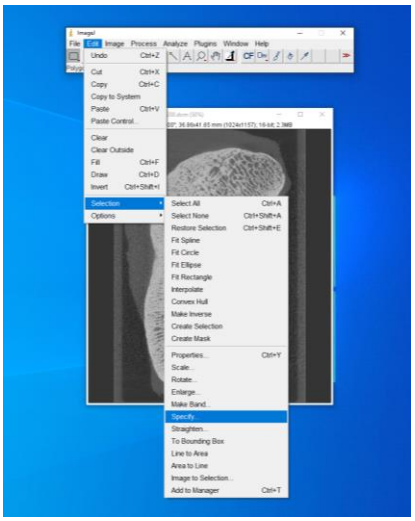

5. In the tab that appears make sure that the “scaled units (mm)” box is checked. Then type in the width and height of the selection window (**make sure the width and height are the same value)**.
   For this, make sure that the selection window only encompasses porous structures and try to exclude large areas of compact bone
6. Click “OK”

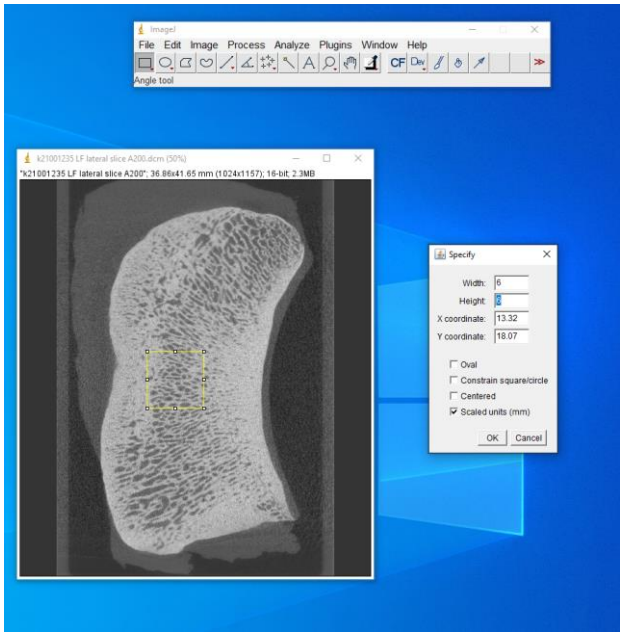

7. Click in the center of the selection window and drag to move it around. Move it to the area you want to take the FFT of

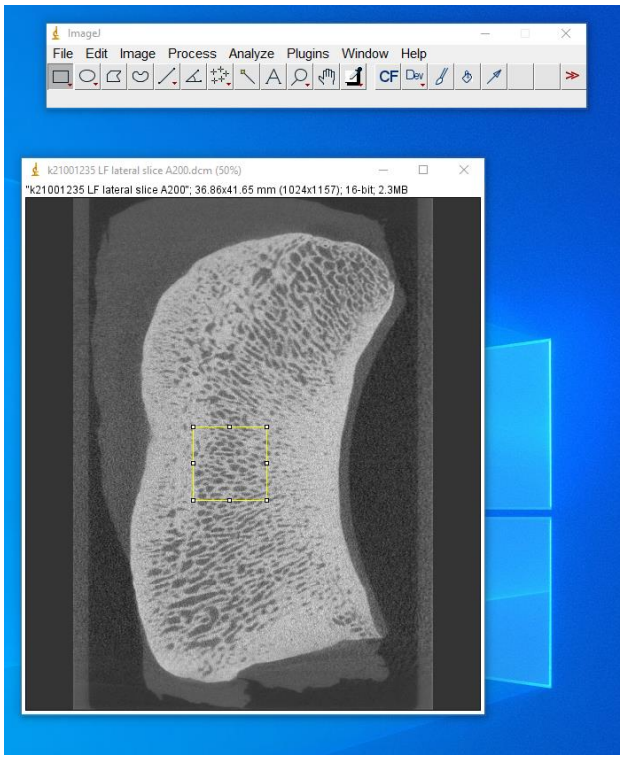

8. Make sure you go back to the “specify” window and record the coordinates and size of the selection window

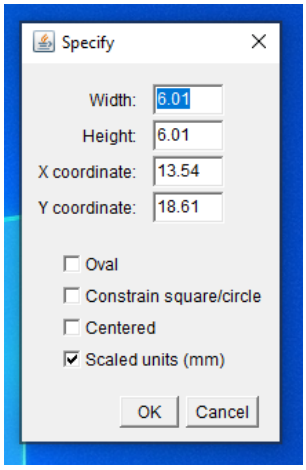

You will be taking three (3) selection windows for each slice.
-1 in the apical region
-1 in the midbody region
-1 in the basilar region
The selection windows should be situated internally with respect to the outside edges of the slice. The articulating surface of the bone will only have compact bone and a very small number of porous structures. This is not the region we are looking for. The palmar aspect of the bone could present differently in its porous network, and to establish a baseline guide on where to take these FFTs and to be able to link relate them within the same bone, we will be taking a consistent area for the windows

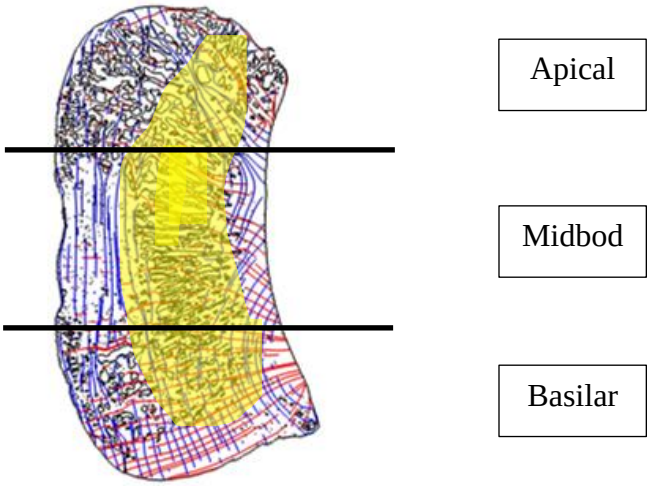

9. Next, go to the “Plugins” tab and click on “Easy PowerSpectrum”

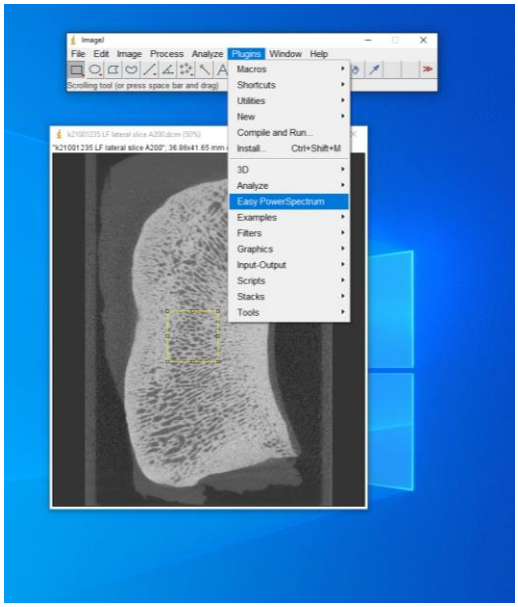

10. In the “Fourier Power Spectrum” select the “Easy Mode” box and select “Unscaled Power Spectrum” with “Report Dominant Peaks.” Then select “Transform”

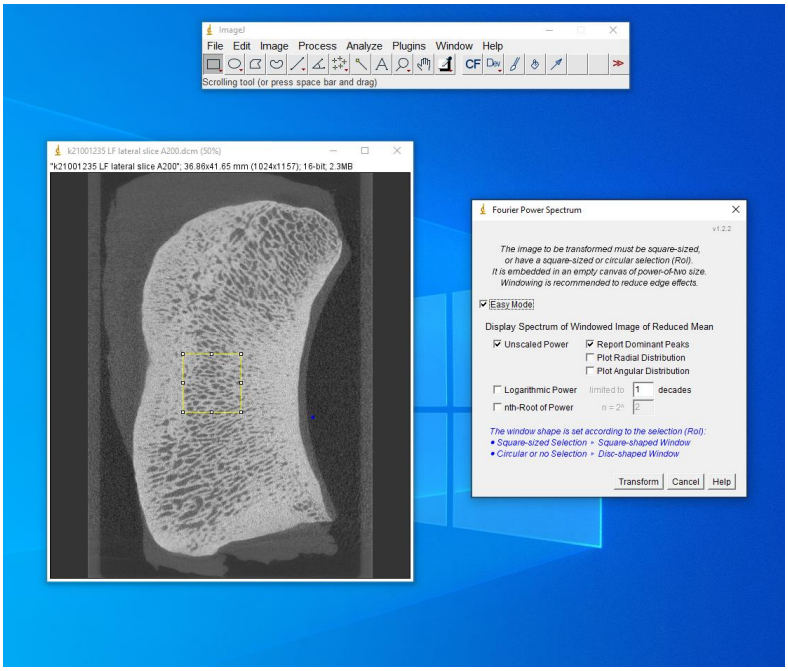

11. The resultant plot should look like this:

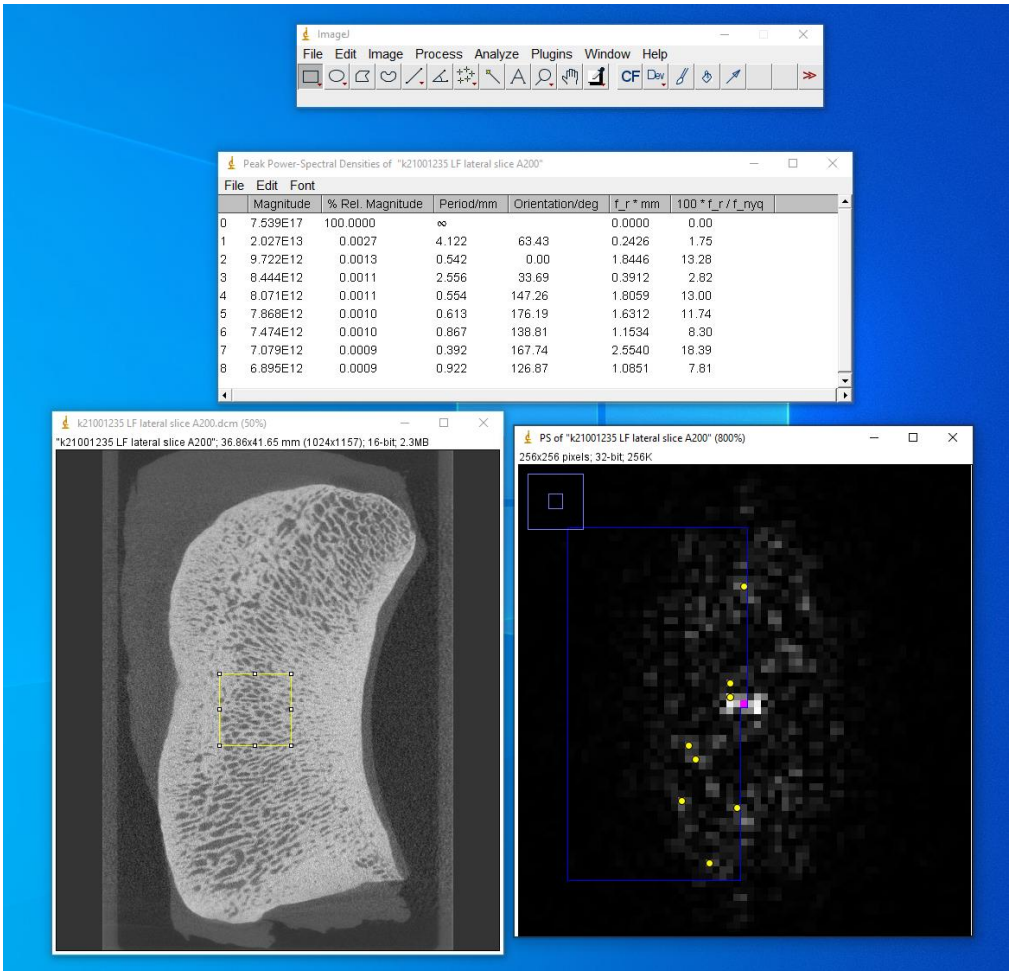

12. Select the “PS” window you just created. Go to the “Image” tab expand the “Lookup Tables” option and select “16 Colors”

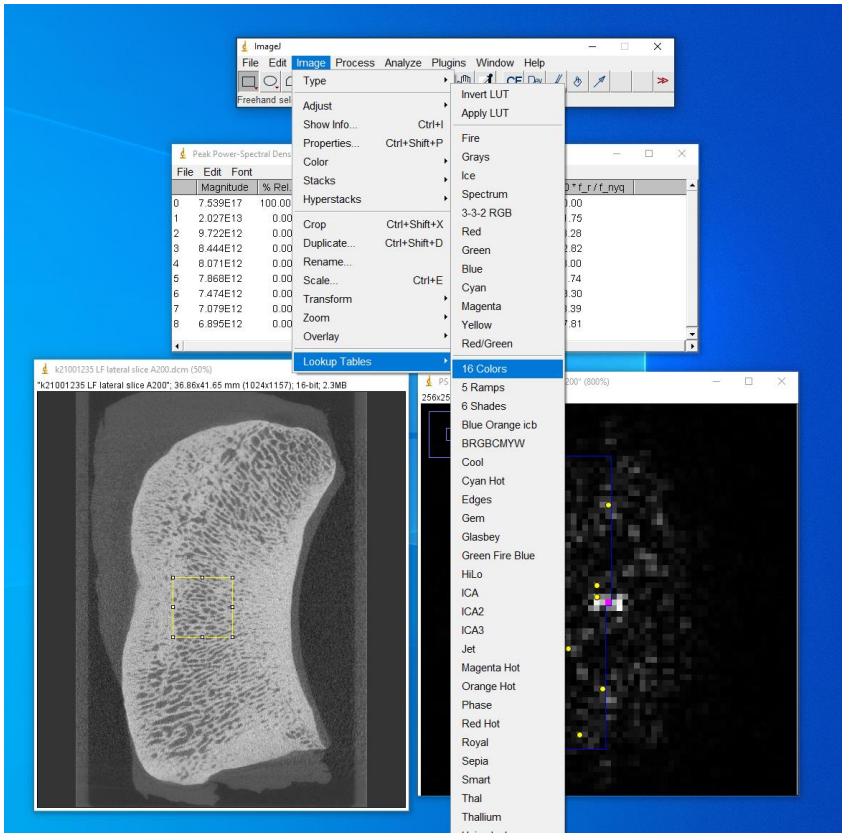

13. Now select the “Image” tab and expand the “Adjust” and click “Threshold.”

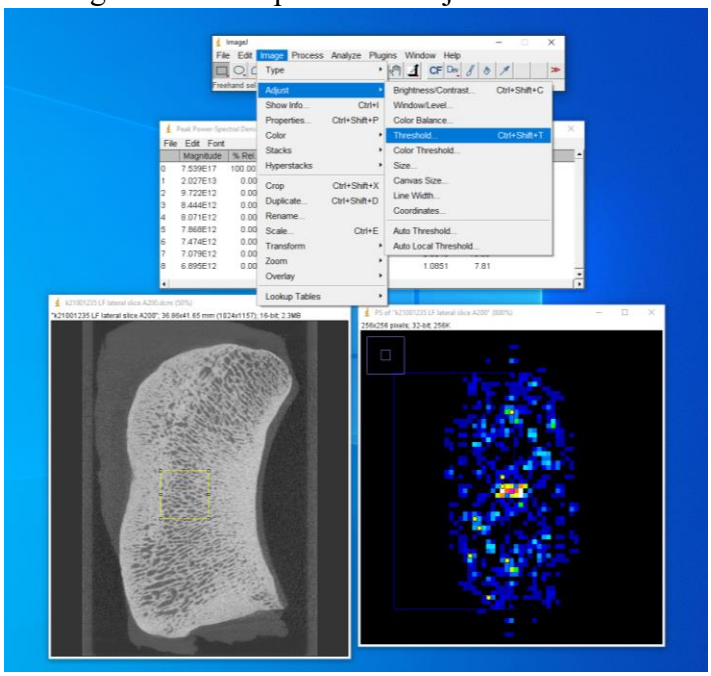

14. For the upper limit (the bottom slide bar), take the slide bar and slide it all the way to the right. For the upper limit (the top slide bar), adjust it so that the pixels marked with the yellow circle are shown in white. (There may be some

surrounding points that also show up because of the thresholding steps on ImageJ).

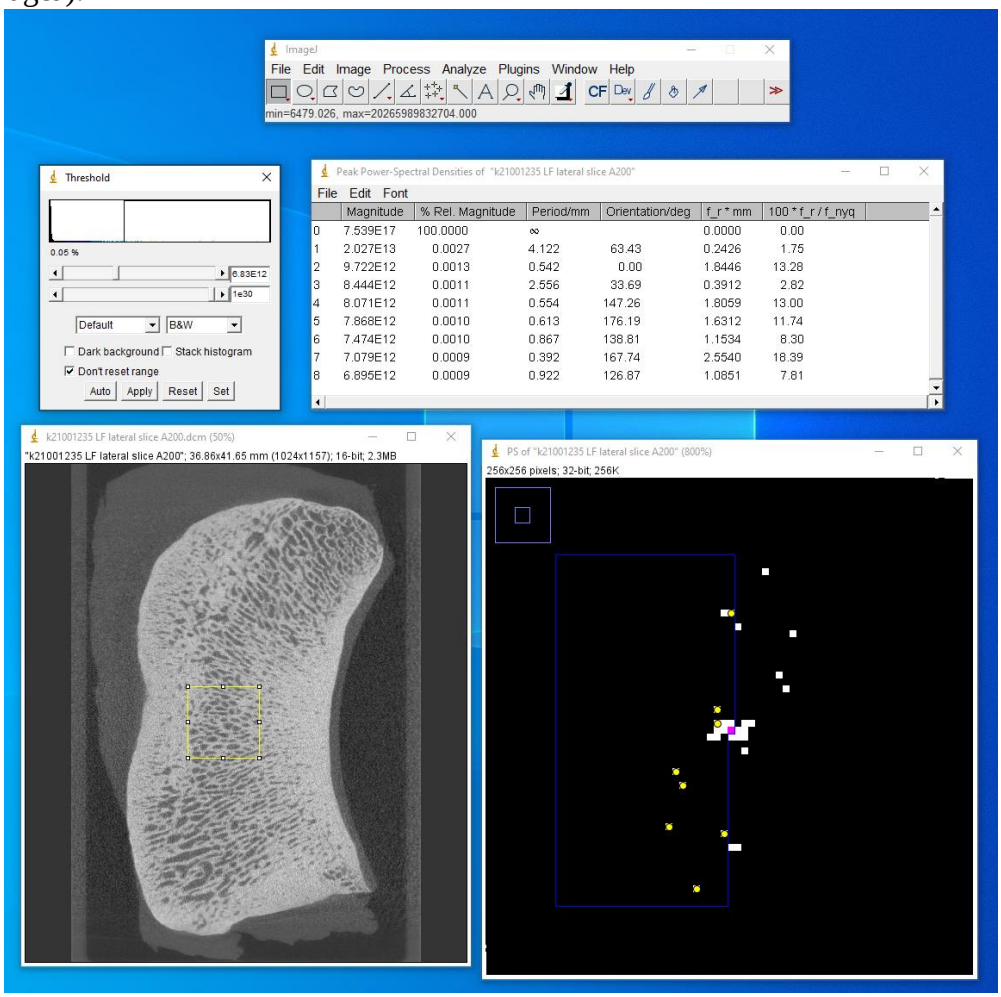

Click “apply” in the threshold window.

15. For the “Thresholder” pop up window, select “convert to mask.”

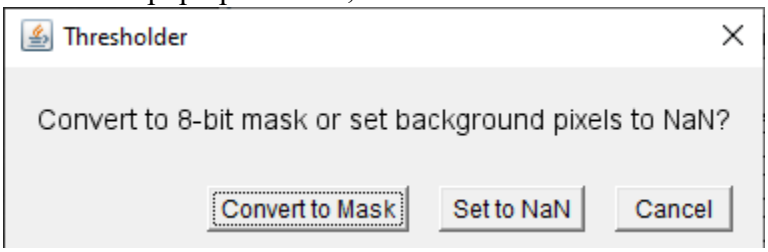

16. The colors on the PS should now be inverted

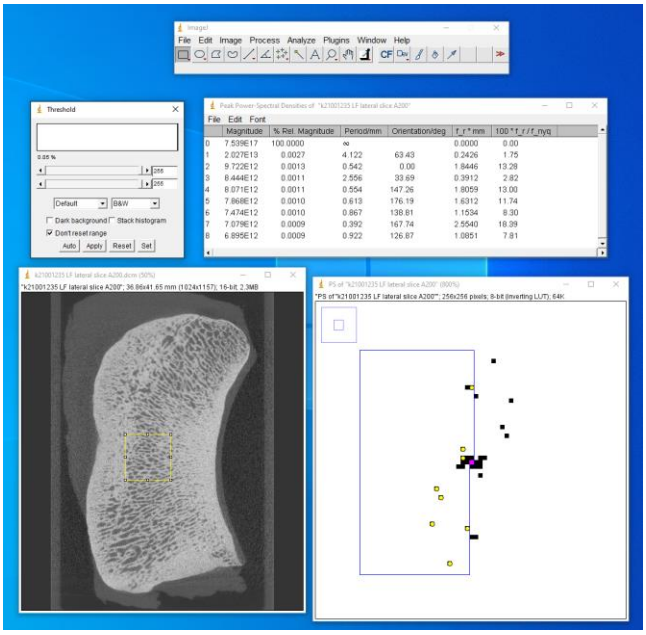

17. Next, change the thresholding limits on the threshold pop-up so that the lower limit is “1” and the upper limit is “255.”

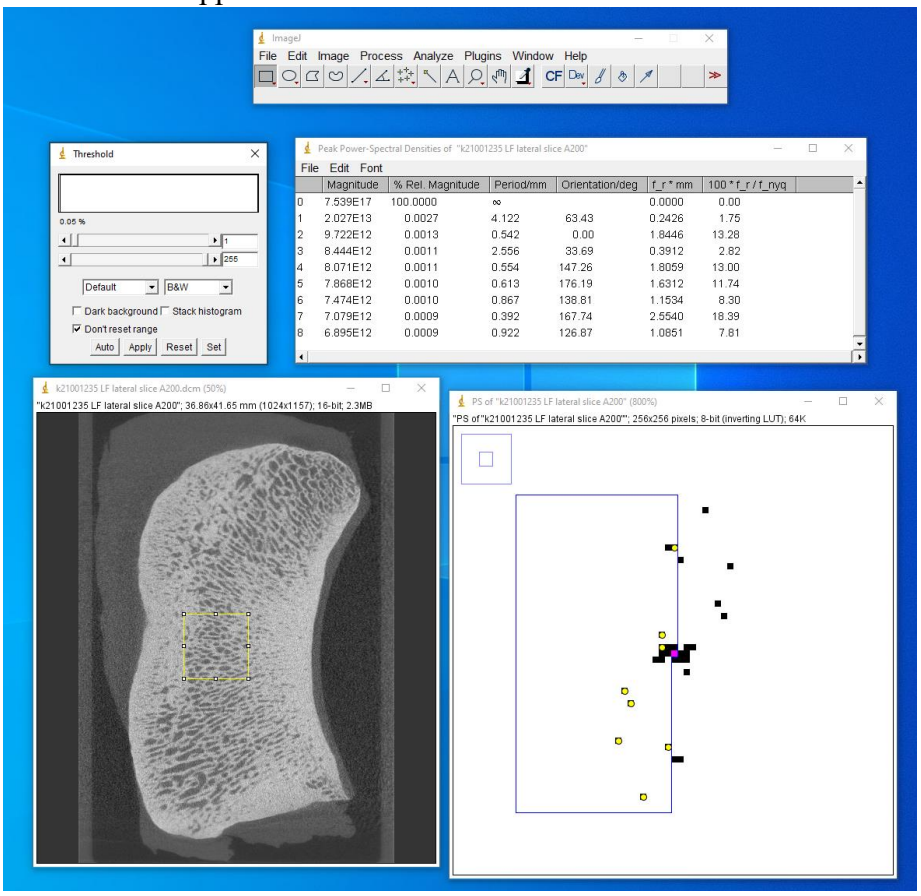

18. Select the PS window and click on the “Analyze” tab and expand the “Tools” options and click on “Save XY Coordinates”

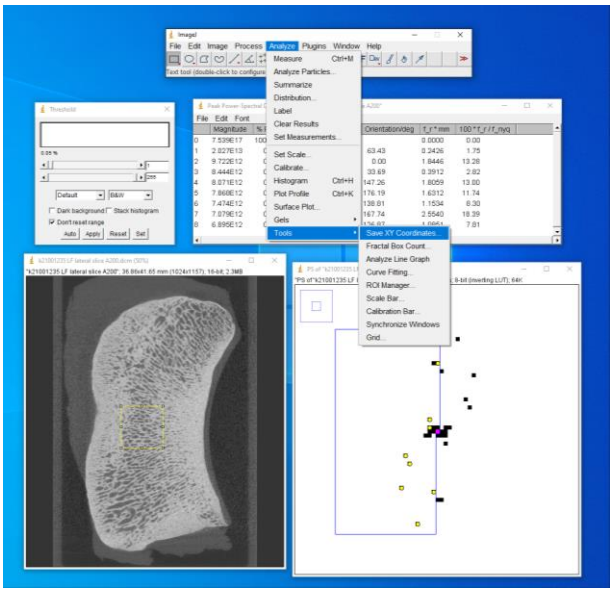

19. Set the “Background value” to “0” and click “OK”

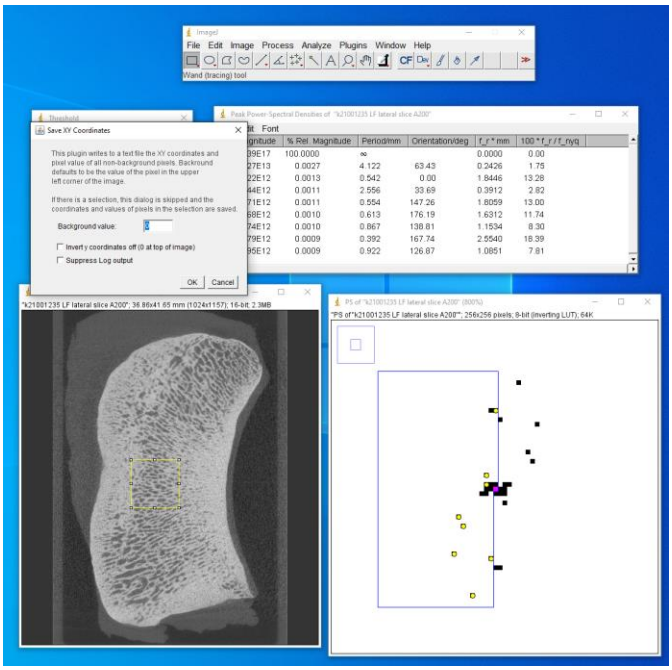

20. Proceed to select where you want to save your file and what you want to name it.

REFERENCES

Anthenill, L.A., Stover, S.M., Gardner, I.A., Hill, A.E., Lee, C.M., Anderson, M.L., Barr, B.C., Read, D.H., Johnson, B.J., Woods, L.W., Daft, B.M., Kinde, H., Moore, J.D., Farman, C.A., Odani, J.S., Pesavento, P.A., Uzal, F.A., Case, J.T. and Ardans, A.A. (2006) Association between findings on palmarodorsal radiographic images and detection of a fracture in the proximal sesamoid bones of forelimbs obtained from cadavers of racing thoroughbreds. Am. J. Vet. Res. 67, 858-868.

Boerckel, J. D., Dupont, K. M., Kolambkar, Y. M., Lin, A. S. P., and Guldberg, R. E. (July 2, 2009). "In Vivo Model for Evaluating the Effects of Mechanical Stimulation on Tissue-Engineered Bone Repair." ASME. *J Biomech Eng*. August 2009; 131(8): 084502. https://doi-org.ezproxy.uky.edu/10.1115/1.3148472

Boerckel, Joel & Uhrig, Brent & Willett, Nick & Huebsch, Nathaniel & Guldberg, Robert. (2011). Mechanical regulation of vascular growth and tissue regeneration in vivo. Proceedings of the National Academy of Sciences of the United States of America. 108. E674-80. 10.1073/pnas.1107019108.

Bonewald L. F. (2011). The amazing osteocyte. *Journal of bone and mineral research : the official journal of the American Society for Bone and Mineral Research*, *26*(2), 229–238. doi:10.1002/jbmr.320

Burr, D.B. The use of finite element analysis to estimate the changing strength of bone following treatment for osteoporosis. *Osteoporosis Int* **27,** 2651–2654 (2016). https://doi.org/10.1007/s00198-016-3707-3

Chang-Yong Ko, Young Jin Jung, Ji Hyung Park, Donghyun Seo, Paul Han, Kiho Bae, Jürgen Schreiber, Han Sung Kim, Trabecular bone response to mechanical loading in ovariectomized Sprague-Dawley rats depends on baseline bone quantity, Journal of Biomechanics, Volume 45, Issue 11, 2012, Pages 2046-2049, ISSN 0021-9290, https://doi.org/10.1016/j.jbiomech.2012.05.013.

Clarke B. (2008). Normal bone anatomy and physiology. *Clinical journal of the American Society of Nephrology : CJASN*, *3 Suppl 3*(Suppl 3), S131–S139. doi:10.2215/CJN.04151206

Cresswell, E.N., McDonough, S.P., Palmer, S.E., Hernandez, C.J. and Reesink, H.L. (2019), Can quantitative computed tomography detect bone morphological changes associated with catastrophic proximal sesamoid bone fracture in Thoroughbred racehorses?. Equine Vet J, 51: 123-130. doi:10.1111/evj.12965.

Diab, S. S., Stover, S. M., Carvallo, F., Nyaoke, A. C., Moore, J., Hill, A., Arthur, R., & Uzal, F. A. (2017). Diagnostic approach to catastrophic musculoskeletal injuries in racehorses. *Journal of veterinary diagnostic investigation : official publication of the American Association of Veterinary Laboratory Diagnosticians, Inc*, *29*(4), 405–413. https://doi.org/10.1177/1040638716685598

Dominguez, V. M., & Agnew, A. M. (2019). Microdamage as a Bone Quality Component: Practical Guidelines for the Two-Dimensional Analysis of Linear Microcracks in Human Cortical Bone. *JBMR plus*, *3*(6), e10203. doi:10.1002/jbm4.10203

Ducy, P., Desbois, C., Boyce, B. *et al.* Increased bone formation in osteocalcin-deficient mice. *Nature* **382,** 448–452 (1996) doi:10.1038/382448a0

Dunkerly, Suzann A. Carson, Hanson, R. Reid, Humburg, Jay, Case Report: Proximal Sesamoid Sequestrum in a Horse, *Equine Practice*, 19(5), 12-15.

Eberle, Sebastian, et al. "An Investigation to Determine If a Single Validated Density–Elasticity Relationship Can Be Used for Subject Specific Finite Element Analyses of Human Long Bones." *Medical Engineering & Physics*, vol. 35, no. 7, 2013, pp. 875–883., https://doi.org/10.1016/j.medengphy.2012.08.022.

Eriksen E. F. (2010). Cellular mechanisms of bone remodeling. *Reviews in endocrine & metabolic disorders*, *11*(4), 219–227. doi:10.1007/s11154-010-9153-1

Filipowska, J., Tomaszewski, K. A., Niedźwiedzki, Ł., Walocha, J. A., & Niedźwiedzki, T. (2017). The role of vasculature in bone development, regeneration and proper systemic functioning. *Angiogenesis*, *20*(3), 291–302. https://doi.org/10.1007/s10456-017-9541-1

Fung YC. (1993) Bone and Cartilage. In: Biomechanics. Springer, New York, NY. https://doi.org/10.1007/978-1-4757-2257-4_12

Galbraith, R. M., & Lavallee, M. E. (2009). Medial tibial stress syndrome: conservative treatment options. *Current reviews in musculoskeletal medicine*, *2*(3), 127–133. https://doi.org/10.1007/s12178-009-9055-6

Geissler, J. R., Bajaj, D., & Fritton, J. C. (2015). American Society of Biomechanics Journal of Biomechanics Award 2013: cortical bone tissue mechanical quality and biological mechanisms possibly underlying atypical fractures. *Journal of biomechanics*, *48*(6), 883–894. doi:10.1016/j.jbiomech.2015.01.032

Gough, Christina. (2019). Sports market size in North America. Retrieved from https://www.statista.com/statistics/214960/revenue-of-the-north-american-sports-market/

Guntur, A. R., & Rosen, C. J. (2012). Bone as an endocrine organ. *Endocrine practice : official journal of the American College of Endocrinology and the American Association of Clinical Endocrinologists*, *18*(5), 758–762. doi:10.4158/EP12141.RA

H.H. Bolotin, DXA in vivo BMD methodology: An erroneous and misleading research and clinical gauge of bone mineral status, bone fragility, and bone remodeling, Bone, Volume 41, Issue 1, 2007, Pages 138-154, ISSN 8756-3282, https://doi.org/10.1016/j.bone.2007.02.022.

H.H. Bolotin, DXA in vivo BMD methodology: An erroneous and misleading research and clinical gauge of bone mineral status, bone fragility, and bone remodelling, Bone, Volume 41, Issue 1, 2007, Pages 138-154, ISSN 8756-3282, https://doi.org/10.1016/j.bone.2007.02.022.

HADJIDAKIS, D.J. and ANDROULAKIS, I.I. (2006), Bone Remodeling. Annals of the New York Academy of Sciences, 1092: 385-396. doi:10.1196/annals.1365.035

Hart, N. H., Nimphius, S., Rantalainen, T., Ireland, A., Siafarikas, A., & Newton, R. U. (2017). Mechanical basis of bone strength: influence of bone material, bone structure and muscle action. *Journal of musculoskeletal & neuronal interactions*, *17*(3), 114–139.

Hess R. A. (2003). Estrogen in the adult male reproductive tract: a review. *Reproductive biology and endocrinology : RB&E*, *1*, 52. doi:10.1186/1477-7827-1-52

Hughes, J. M., Charkoudian, N., Barnes, J. N., & Morgan, B. J. (2016). Revisiting the Debate: Does Exercise Build Strong Bones in the Mature and Senescent Skeleton?. *Frontiers in physiology*, *7*, 369. doi:10.3389/fphys.2016.00369

Hughes, J. M., Charkoudian, N., Barnes, J. N., & Morgan, B. J. (2016). Revisiting the Debate: Does Exercise Build Strong Bones in the Mature and Senescent Skeleton?. *Frontiers in physiology*, *7*, 369. doi:10.3389/fphys.2016.00369

Ji, M. X., & Yu, Q. (2015). Primary osteoporosis in postmenopausal women. *Chronic diseases and translational medicine*, *1*(1), 9–13. doi:10.1016/j.cdtm.2015.02.006

Kim KJ, Li B, Winer J, et al. Inhibition of vascular endothelial growth factor-induced angiogenesis suppresses tumour growth in vivo. Nature. 1993;362:841-4

Kreider, J. M., & Goldstein, S. A. (2009). Trabecular bone mechanical properties in patients with fragility fractures. *Clinical orthopaedics and related research*, *467*(8), 1955–1963. doi:10.1007/s11999-009-0751-8

Langdahl, B., Ferrari, S., & Dempster, D. W. (2016). Bone modeling and remodeling: potential as therapeutic targets for the treatment of osteoporosis. *Therapeutic advances in musculoskeletal disease*, *8*(6), 225–235. doi:10.1177/1759720X16670154

Liqin Xie, Jeffrey M. Jacobson, Edna S. Choi, Bhavin Busa, Leah Rae Donahue, Lisa M. Miller, Clinton T. Rubin, Stefan Judex, Low-level mechanical vibrations can influence bone resorption and bone formation in the growing skeleton, Bone,

Volume 39, Issue 5, 2006, Pages 1059-1066, ISSN 8756-3282, https://doi.org/10.1016/j.bone.2006.05.012.

Maffioli P., Derosa G. (2017) Overview of Biochemical Markers of Bone Metabolism. In: Patel V., Preedy V. (eds) Biomarkers in Bone Disease. Biomarkers in Disease: Methods, Discoveries and Applications. Springer, Dordrecht. https://doi-org.ezproxy.uky.edu/10.1007/978-94-007-7693-7_24

Marenzana, M., & Arnett, T. R. (2013). The Key Role of the Blood Supply to Bone. *Bone research*, *1*(3), 203–215. doi:10.4248/BR201303001

Martig, S., Chen, W., Lee, P. V., & Whitton, R. C. (2014). Bone fatigue and its implications for injuries in racehorses. *Equine veterinary journal*, *46*(4), 408–415. https://doi.org/10.1111/evj.12241

Mohamed A. M. (2008). An overview of bone cells and their regulating factors of differentiation. *The Malaysian journal of medical sciences : MJMS*, *15*(1), 4–12.

Mohsin, S., O'Brien, F. J., & Lee, T. C. (2006). Microcracks in compact bone: a three-dimensional view. *Journal of anatomy*, *209*(1), 119–124. doi:10.1111/j.1469-7580.2006.00554.x

N.Thompson, K., & Cheung, T.K. (1994). A Finite Element Model of the Proximal Sesamoid Bones of the Horse Under Different Loading Conditions. *VCOT Archive, 7*, 40-44.

Oliver M., Waxman E.S. (2019) The Role of Anti-Angiogenic Agents (VEGF). In: Davies M., Eaby-Sandy B. (eds) Targeted Therapies in Lung Cancer: Management Strategies for Nurses and Practitioners. Springer, Cham

Panagiotopoulou, O. (2009). Finite element analysis (FEA): Applying an engineering method to functional morphology in anthropology and human biology. Annals of Human Biology, 36(5), 609–623.

Peter Augat, Sandra Schorlemmer, The role of cortical bone and its microstructure in bone strength, *Age and Ageing*, Volume 35, Issue suppl_2, September 2006, Pages ii27–ii31, https://doi.org/10.1093/ageing/afl081

Peter Muir, Susannah J. Sample, Jennifer G. Barrett, Jenna McCarthy, Ray Vanderby, Mark D. Markel, Laura J. Prokuski, Vicki L. Kalscheur, Effect of fatigue loading and associated matrix microdamage on bone blood flow and interstitial fluid flow, Bone, Volume 40, Issue 4, 2007, Pages 948-956, ISSN 8756-3282, https://doi.org/10.1016/j.bone.2006.11.012.

Price, Brianna M., Davis, Joseph E., et al. (2021, March 5). Vasculature of the Equine Proximal Sesamoid Bone [Poster Presentation]. LMU-CVM Research Day, Virtual.

Raggatt, L. J., & Partridge, N. C. (2010). Cellular and molecular mechanisms of bone remodeling. *The Journal of biological chemistry*, *285*(33), 25103–25108. doi:10.1074/jbc.R109.041087

Ramasamy, R., Armstrong, J. M., & Lipshultz, L. I. (2015). Preserving fertility in the hypogonadal patient: an update. *Asian journal of andrology*, *17*(2), 197–200. doi:10.4103/1008-682X.142772

Rho, Jae-Young, et al. "Mechanical Properties and the Hierarchical Structure of Bone." *Medical Engineering & Physics*, vol. 20, no. 2, 1998, pp. 92–102., https://doi.org/10.1016/s1350-4533(98)00007-1.

Riddle, R. C., Khatri, R., Schipani, E., & Clemens, T. L. (2009). Role of hypoxia-inducible factor-1alpha in angiogenic-osteogenic coupling. *Journal of molecular medicine (Berlin, Germany)*, *87*(6), 583–590. doi:10.1007/s00109-009-0477-9

Robert P Heaney, Is the paradigm shifting?, Bone, Volume 33, Issue 4, 2003, Pages 457-465, ISSN 8756-3282, https://doi.org/10.1016/S8756-3282(03)00236-9.

Rubin, C., Recker, R., Cullen, D., Ryaby, J., McCabe, J., & McLeod, K. (2004). Prevention of Postmenopausal Bone Loss by a Low-Magnitude, High-Frequency Mechanical Stimuli: A Clinical Trial Assessing Compliance, Efficacy, and Safety. *Journal of Bone and Mineral Research*, *19*(3), 343–351. https://doi.org/10.1359/JBMR.0301251

Schnabel, L.V. and Redding, W.R. (2018), Diagnosis and management of proximal sesamoid bone fractures in the horse. Equine Vet Educ, 30: 450-455. https://doi.org/10.1111/eve.12615

Shetty, S., Kapoor, N., Bondu, J. D., Thomas, N., & Paul, T. V. (2016). Bone turnover markers: Emerging tool in the management of osteoporosis. *Indian journal of endocrinology and metabolism*, *20*(6), 846–852. https://doi.org/10.4103/2230-8210.192914

Shibuya M. (2011). Vascular Endothelial Growth Factor (VEGF) and Its Receptor (VEGFR) Signaling in Angiogenesis: A Crucial Target for Anti- and Pro-Angiogenic Therapies. *Genes & cancer*, *2*(12), 1097–1105. https://doi.org/10.1177/1947601911423031

Su, N., Yang, J., Xie, Y., Du, X., Chen, H., Zhou, H., & Chen, L. (2019). Bone function, dysfunction and its role in diseases including critical illness. *International journal of biological sciences*, *15*(4), 776–787. doi:10.7150/ijbs.27063

Su, N., Yang, J., Xie, Y., Du, X., Chen, H., Zhou, H., & Chen, L. (2019). Bone function, dysfunction and its role in diseases including critical illness. *International journal of biological sciences*, *15*(4), 776–787. https://doi.org/10.7150/ijbs.27063

Tanaka, K., Yamaguchi, Y. & Hakeda, Y. Isolated chick osteocytes stimulate formation and bone-resorbing activity of osteoclast-like cells. *J Bone Miner Metab* **13,** 61–70 (1995) doi:10.1007/BF01771319

Teichtahl, A. J., Wluka, A. E., Wijethilake, P., Wang, Y., Ghasem-Zadeh, A., & Cicuttini, F. M. (2015). Wolff's law in action: a mechanism for early knee

osteoarthritis. *Arthritis research & therapy*, *17*(1), 207. doi:10.1186/s13075-015-0738-7

Trumble, Troy N., Arnoczky, Steven P., Stick, John A., Stickle, Russ L., Clinical Relevance of the Microvasculature of the Equine Sesamoid Bone, *American Journal of Veterinary Research, 56 (6),* 720-724.

Tzaphlidou M. (2008). Bone architecture: collagen structure and calcium/phosphorus maps. *Journal of biological physics*, *34*(1-2), 39–49. doi:10.1007/s10867-008-9115-y

Unnanuntana, A., Gladnick, B. P., Donnelly, E., & Lane, J. M. (2010). The assessment of fracture risk. *The Journal of bone and joint surgery. American volume*, *92*(3), 743–753. doi:10.2106/JBJS.I.00919

Walsh, Jennifer S. "Normal Bone Physiology, Remodelling and Its Hormonal Regulation." *Surgery.* 33.1 (2015): 1-6. Web.

Ward, K., Alsop, C., Caulton, J., Rubin, C., Adams, J., & Mughal, Z. (2004). Low Magnitude Mechanical Loading Is Osteogenic in Children With Disabling Conditions. *Journal of Bone and Mineral Research*, *19*(3), 360–369. https://doi.org/10.1359/JBMR.040129

Wren, T. A., Lee, D. C., Hara, R., Rethlefsen, S. A., Kay, R. M., Dorey, F. J., & Gilsanz, V. (2010). Effect of high-frequency, low-magnitude vibration on bone and muscle in children with cerebral palsy. *Journal of pediatric orthopedics*, *30*(7), 732–738. https://doi.org/10.1097/BPO.0b013e3181efbabc

Xie, Y., Zhang, L., Xiong, Q. *et al.* Bench-to-bedside strategies for osteoporotic fracture: From osteoimmunology to mechanosensation. *Bone Res* **7,** 25 (2019). https://doi.org/10.1038/s41413-019-0066-7

Yao, Z., Lafage-Proust, M.-H., Plouët, J., Bloomfield, S., Alexandre, C. and Vico, L. (2004), Increase of Both Angiogenesis and Bone Mass in Response to Exercise

Depends on VEGF. J Bone Miner Res, 19: 1471-1480. doi:10.1359/JBMR.040517

Zaiontz, Charles (2010). Xrealstats (Version 1.2.2) [Microsoft Excel]. Real Statistics Using Excel.

Zysset, P. K., Dall'ara, E., Varga, P., & Pahr, D. H. (2013). Finite element analysis for prediction of bone strength. *BoneKEy reports*, *2*, 386. doi:10.1038/bonekey.2013.120

VITA

Education:

- Bachelor of Science Degree

  Major: Biosystems Engineering

  Minor: Biomedical Engineering

  Minor: Mathematics

  Status: Lewis Honors College

Experience:

- Graduate Research Assistant, Department of Biomedical Engineering, University of Kentucky, August 2019-May 2022
- Treasurer, Society for Biomaterials Student Chapter, University of Kentucky, September 2019- May 2021
- Manufacturing Engineering Intern, Big Ass Fans, June 2019-August 2019
- Quality Engineering Intern, Schneider Electric, June 2018-April 2019
- Controls Engineering Intern, Schneider Electric, July 2017-November 2017

Abstracts and Presentations:

- Erik Davis, David Patino, Yu Zhao Ph.D., Jennifer Janes, DVM, Ph.D., James MacLeod, VMD, Ph.D., Guigen Zhang Ph.D., "Probing the Connections between Micro-Vasculature of Bone and Its Mechanical Integrity and Pathology," Poster and Abstract accepted, Cardiovascular Research Day 2019, Lexington, KY
- Erik Davis, David Patino, Yu Zhao Ph.D., Jennifer Janes, DVM, Ph.D., James MacLeod, VMD, Ph.D., Guigen Zhang Ph.D., "Probing the Connections between Micro-Vasculature of Bone and Its Mechanical Integrity and Pathology," Poster and Abstract accepted, BMES Annual Meeting 2020, Virtual
- Brianna M. Price, Joseph E. Davis, Guigen Zhang, Katherine S. Garrett, Laura A. Kennedy, and Jennifer G. Janes, "Vasculature of the Equine Proximal Sesamoid Bone," Poster for LMU-CVM Research Day, Virtual
- Erik Davis, Jennifer Janes, DVM, Ph.D., James MacLeod, VMD, Ph.D., Guigen Zhang Ph.D. "Revelation of Vasculature Tree Structure Inside Sesamoid Bone and Its Impact on Bone Mechanical Integrity", Accepted for oral presentation, 2021 Annual meeting of the Society for Biomaterials, Virtual
- Erik Davis, Yu Zhao Ph.D.**,** Brianna Price, Jennifer Janes, DVM, Ph.D., Dipl. ACVP, Laura Kennedy DVM, Dipl. ACVP, James MacLeod, VMD, Ph.D., Guigen Zhang Ph.D. "Probing the Microstructural Differences in Equine Proximal

Sesamoid Bones Using Imaging FFT," Poster and Abstract accepted, Annual CCTS Spring Conference 2021, Virtual.

Joseph Erik Davis